UNIVERSITY OF CALIFORNIA, SAN DIEGO

Marine Gravity Variations and the Strength of the Oceanic Lithosphere with Bending

A dissertation submitted in partial satisfaction of the
requirements for the degree
Doctor of Philosophy

in

Earth Sciences

by

Emmanuel Soliman Mortel Garcia

Committee in charge:

Professor David T. Sandwell, Chair
Professor Yuri Fialko
Professor Jeffrey Gee
Professor Stefan G. Llewellyn Smith
Professor Tara C. Hutchinson
Professor Pål Wessel

2016

The dissertation of Emmanuel Soliman Mortel Garcia is approved, and it is acceptable in quality and form for publication on microfilm and electronically:

_____

_____

_____

_____

_____

_____

Chair

University of California, San Diego

2016

DEDICATION

EPIGRAPH

Whence does one come
when he speaks, his eyes lighting up?
Before speech, all words are dead,
their legends blind.
No one comes from language,
the truth is what words dream.
One speaks, and language comes,
the light in one's blood.

– Gemino H. Abad
The Light in One's Blood

TABLE OF CONTENTS

LIST OF FIGURES

LIST OF TABLES

ACKNOWLEDGEMENTS

Chapter 2, in full, is a reprint of the material as it appears in the Geophysical Journal International: Garcia, E.S., D.T. Sandwell, and W.H.F. Smith, "Retracking CryoSat-2, Envisat and Jason-1 radar altimetry waveforms for improved gravity field recovery", *Geophysical Journal International*, *196*(3): 1402–1422, doi: 10.1093/gji/ggt469, 2014. The dissertation author was the primary investigator and author of the paper.

Chapter 3, in full, is a reprint of the material as it appears in the Geophysical Journal International: Garcia, E.S., D.T. Sandwell, and K.M. Luttrell, "An iterative spectral solution method for thin elastic plate flexure with variable rigidity", *Geophysical Journal International*, 200(2): 1010–1026, doi: 10.1093/gji/ggu449, 2015. The dissertation author was the primary investigator and author of the paper.

Chapter 4, in full, is a preprint of material being prepared for submission to Geophysics Geochemistry Geosystems: Garcia, E. S., D. T. Sandwell, and D.G. Bassett, Outer Trench Slope Flexure and Faulting at Pacific Basin Subduction Zones. The dissertation author was the primary investigator and author of the paper.

VITA

2007	B. S. in Physics, University of the Philippines Diliman
2009	M. S. in Physics, University of the Philippines Diliman
2010	Postgraduate Diploma in Earth System Physics, Abdus Salam International Centre for Theoretical Physics
2016	Ph. D. in Earth Sciences, University of California, San Diego

PUBLICATIONS

Garcia, Emmanuel S., David T. Sandwell, and Karen M. Luttrell. An iterative spectral solution method for thin elastic plate flexure with variable rigidity. *Geophys. J. Int.*, *200*(2): 1010–1026, doi: 10.1093/gji/ggu449, 2015.

Sandwell, David T., R. Dietmar Müller., Walter H.F. Smith, **Emmanuel S. Garcia**, and Richard Francis. New global marine gravity model from CryoSat-2 and Jason-1 reveals buried tectonic structure. *Science*, *346*(6205), 65-67, doi:10.1126/science.1258213, 2014.

Garcia, Emmanuel S., David T. Sandwell, and Walter H.F. Smith. Retracking CryoSat-2, Envisat and Jason-1 radar altimetry waveforms for improved gravity field recovery. *Geophys. J. Int.*, *196*(3), 1402–1422, doi: 10.1093/gji/ggt469, 2014.

Sandwell, David T., **Emmanuel S. Garcia**, Khalid Soofi, Pål Wessel, Michael Chandler, and Walter H.F. Smith. Toward 1-mGal accuracy in global marine gravity from CryoSat-2, Envisat, and Jason-1. *The Leading Edge*, *32*(8), 892-899, doi:10.1190/tle32080892.1, 2013.

ABSTRACT OF THE DISSERTATION

Marine Gravity Variations and the Strength of the Oceanic Lithosphere with Bending

by

Emmanuel Soliman Mortel Garcia

Doctor of Philosophy in Earth Sciences

University of California, San Diego, 2016

Professor David T. Sandwell, Chair

The variations of the Earth's gravity field at spatial scales ranging from tens to hundreds of kilometers over the deep ocean basins can be measured with satellite remote sensing of sea surface slopes. As the composition of the crust and upper mantle comprising the oceanic lithosphere is highly uniform, these gravity variations are closely linked to geological structures formed by tectonic processes. One such process is the subduction of oceanic lithosphere into the planetary interior at deep-sea trenches. The combination of a bending moment from the slab sinking and a downward load from the overriding plate causes flexure of the lithosphere. This flexure produces the prominence of the trench outer rise and the slope of the outer trench wall. Extension of the plate at the outer rise is often accompanied by

the formation of faults, which can reduce the plate strength and hence the amount of stress that the plate can support.

Data from recent radar altimetry missions of the CryoSat-2, Envisat and Jason-1 satellites was reprocessed to improve the accuracy of a global marine gravity field model. This reprocessing technique ("retracking") refines the precision of radar range measurements by a factor of 1.5. An approximate mathematical model was formulated to enable retracking of radar waveforms collected by a novel instrument onboard CryoSat-2 in the synthetic aperture radar (SAR) mode.

A computational algorithm was developed for solving the thin plate flexure equation for spatially varying rigidity in two horizontal distributions subject to applied loads. The accuracy of the method was tested against analytic solutions. This modeling technique was applied to the oceanic lithosphere for the trench flexure case. Solving a parameter estimation problem generated flexural deformation surfaces that fit marine gravity and bathymetry observations at trench locations around the Pacific basin. Our results show that a flexure model in which the initial strength of the plate depends on age but is allowed to decreased through inelastic yielding is consistent with observations of the incoming lithosphere at Pacific subduction zones.

Chapter 1

Introduction

1.1 Outline of the Dissertation

This dissertation combines three studies concerning the oceanic lithosphere but with each one emphasizing a different methodology: data collection and improvement, mathematical and numerical forward modeling, and inverse modeling through parameter estimation. The first chapter describes the processing and analysis of satellite radar altimeter observations for mapping marine gravity anomalies across the global ocean. The second chapter explains in detail a mathematical formulation for thin elastic plate flexure with variable rigidity along with a computational technique that finds accurate solutions rapidly. The third and last chapter builds upon the contributions of the first two by leveraging an improved data set and numerical models to solve a parameter estimation problem for the bending of oceanic lithosphere at subduction zones.

1.2 Recovering the Marine Gravity Signal using Satellite Altimetry

My co-authors and I developed in-house software tools for processing new satellite data from the recent CryoSat-2 and Jason-1 radar altimetry missions to recover the marine gravity signal. CryoSat-2 was originally designed for observing

ice in the polar regions with a novel instrument mode, but it also collects altimeter return waveforms over the oceans. Meanwhile, Jason-1 was originally tasked for physical oceanography applications but was placed in a non-repeat orbit for the final phase of its mission, which is more ideal for geodetic mapping. We derived a simple mathematical approximation to fit the CryoSat-2 waveforms and estimate sea surface slopes. These slope measurements are then used to construct a global marine gravity model. Such maps of marine gravity anomalies serve as a fundamental data set for interpreting geological features especially where no high-resolution ship surveys are available, which is around 80 percent of the entire seafloor. The gravity map also allows for the interpretation of tectonic structures buried beneath sediment. The following chapters of this dissertation concentrates on the incoming plate at oceanic subduction zones. At these locations, the negative anomaly at the deep-sea trench is typically lower than -100 mGal, and the positive anomaly associated with the outer rise is typically on the order of 50 mGal.

1.3 Solving Thin Elastic Plate Flexure Equations with Analytic and Numerical Methods

In this chapter, we adapted an iterative solution method aided by Fast Fourier Transform routines to solve the governing equations for static thin plate flexure with the elastic thickness varying across two horizontal dimensions. This mechanical model is applicable to geological settings where the bent plate has non-uniform rigidity over the area that is deforming. We performed benchmark tests of our software against textbook formulas as well as novel analytic solutions.

1.4 Modeling of Lithosphere Bending at Subduction Zones

The lithosphere is the outermost solid layer of the Earth, and it is comprised of rigid units called plates which move with respect to each other. Depending

on the direction of this relative motion, plate boundaries can be one of three types: divergent, transform, or convergent. When one of the plates at a convergent boundary consists of oceanic lithosphere and has sufficient negative buoyancy to sink into the mantle, then the plate is said to be subducting under the overriding plate. Deep ocean trenches are the surface expression of subduction zones, and across the entire Earth surface these have a combined length of approximately 40,000 kilometers.

At a trench, the lithosphere is bent well beyond its elastic limit. A simplified description of the oceanic lithosphere strength is specified by a layered rheology that is brittle near the surface, elastic in the middle, and ductile at greater depths. We implemented a self-consistent numerical approach which computed an effective elastic thickness based on the local curvature of the deflected plate surface and the amount of yielding predicted by the brittle-elastic-plastic rheology.

Using this nonlinear flexure algorithm along with the improved gravity observations resulting from the work of Chapter 2 and an updated compilation of high-resolution bathymetry, we modeled the topographic relief of the outer rise at trenches and examined the impact of bending on extensional faulting at the trench outer slope (see Fig. 1.4 for an illustration). The flexural deformation surface is generated by solving a parameter estimation problem. We infer the applied load distribution close to the trench axis required to compute forward models of plate deflection by fitting marine gravity anomalies and shipboard bathymetry data. Since the model allows for lateral variations in plate rigidity, it incorporates both weakening effects from brittle deformation and strengthening due to cooling with age. We generated numerous outer rise flexure models for regions outboard of subduction zones around the Pacific basin, with seafloor ages ranging from 20 to 150 million years old. Our preferred models display decreasing elastic thickness toward the trench, and the final values do not have a conclusive dependence on the lithosphere age.

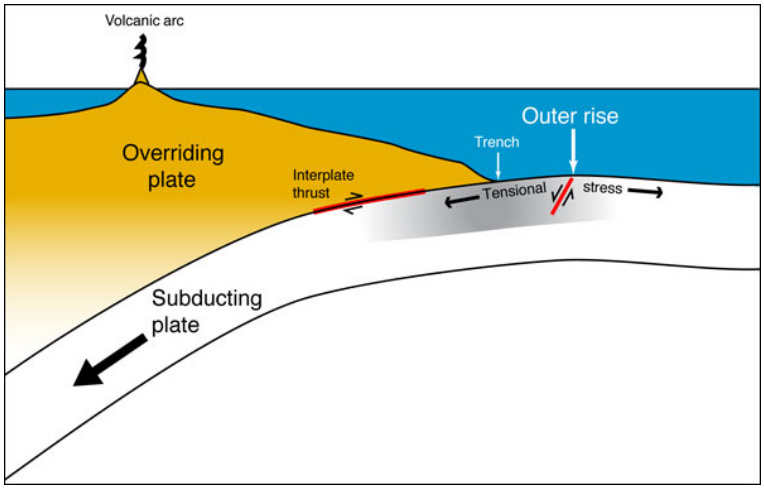

Figure 1.4: An illustration of a subduction zone showing the trench and the outer rise. (Eric Geist, United States Geological Survey)

Chapter 2

Retracking CryoSat-2, Envisat and Jason-1 radar altimetry waveforms for improved gravity field recovery

Abstract

Improving the accuracy of the marine gravity field requires both improved altimeter range precision and dense track coverage. After a hiatus of more than 15 yr, a wealth of suitable data is now available from the CryoSat-2, Envisat and Jason-1 satellites. The range precision of these data is significantly improved with respect to the conventional techniques used in operational oceanography by retracking the altimeter waveforms using an algorithm that is optimized for the recovery of the short-wavelength geodetic signal. We caution that this new approach, which provides optimal range precision, may introduce large-scale errors that would be unacceptable for other applications. In addition, CryoSat-2 has a new synthetic aperture radar (SAR) mode that should result in higher range precision. For this new mode we derived a simple, but approximate, analytic model for the shape of the SAR waveform that could be used in an iterative least-squares

algorithm for estimating range. For the conventional waveforms, we demonstrate that a two-step retracking algorithm that was originally designed for data from prior missions (ERS-1 and Geosat) also improves precision on all three of the new satellites by about a factor of 1.5. The improved range precision and dense coverage from CryoSat-2, Envisat and Jason-1 should lead to a significant increase in the accuracy of the marine gravity field.

2.1 Introduction

The remote ocean basins remain largely unexplored by ships (Wessel & Chandler, 2011) and are opaque to direct electromagnetic sounding, and so satellite radar altimeters are the tool of choice for global reconnaissance of the bathymetry and tectonics of the ocean basins (Smith, 1998). Seafloor topography and crustal geology are isostatically compensated (Watts 2001) and so generate gravity anomalies primarily at wavelengths of 160 km and shorter (Smith & Sandwell, 1994) . Anomalies of horizontal wavelength λ are reduced in amplitude by an amount $\exp(-2\pi z/\lambda)$ when observed at a height z above the field's source (Parker, 1973), so the gravity signal of seafloor structure is insensible by gravity satellite missions such as GOCE (z 250 km) or GRACE (z 450 km). Radar altimeters sense the gravity field at the ocean surface so for a typical ocean depth of 4 km, the smallest spatial scale recoverable is 6 km. The scientific rationale for improved gravity is fairly mature and a set of papers related to this topic was published in a special issue of *Oceanography* (Smith, 2004), entitled *Bathymetry from Space*. These studies show that achieving an accuracy of 1 mGal at a horizontal resolution of 6 km would enable major advances for a large number of basic science and practical applications.

Radar altimeters measure the height of the ocean surface, which to a first approximation is a measure of gravitational potential. Gravity anomalies are the vertical derivative of the potential and they can be recovered from the two horizontal derivatives of the potential (i.e. sea surface gradient) through Laplace's equation; 1 mGal of gravity anomaly roughly corresponds to 1 μrad (microradian)

of ocean surface slope. Therefore, achieving this 1 mGal threshold requires a radar altimeter range having a precision of 6 mm over 6-km horizontal distance. This precision could be derived from a single profile or a stack of repeated profiles. The gravity signal is most accurately recovered by working with along-track sea surface slopes rather than heights (Sandwell, 1984; Olgiati et al., 1995). Many factors that affect the absolute height accuracy of altimetric sea level (Chelton D.B. & P.S, 2001) have correlation scales long enough that they yield negligible error in along-track slope ((Sandwell & Smith, 2009), table 3). The error budget for gravity recovery from altimetry is dominated by the range precision of the radar measurement. This precision can be improved by a process known as 'retracking' (Sandwell & Smith, 2005, 2009).

In addition to high-range precision, the accuracy of the global marine gravity field depends on dense track spacing, which needs to be less than the desired resolution of 6 km. Current gravity fields having accuracies of 35 mGal (e.g. S&S V18 (Sandwell & Smith, 2009) and DNSC08 (Andersen et al., 2010)) are based primarily on dense track coverage from 18 months of Geodetic Satellite (Geosat) geodetic mission (GM) data collected in (Sandwell & McAdoo, 1990) and 12 months of European Remote-Sensing Satellite-1 (ERS-1/GM) data collected in 19951996. Between 1995 and 2010 seven radar altimeter missions flew, yet none of them contributed significantly to marine gravity field mapping except in the Arctic areas where the tracks converge (Laxon & McAdoo, 1994; Childers et al., 2001). All were confined to 'exact repeat' orbits which revisited the same ground points every 1035 days, resulting in track spacings of 80 km and longer at the Equator, too wide to usefully sample the $\lambda < 160$ km field.

New altimeter data have become available in the last 2 yr that will have a significant impact on marine mapping (Louis et al., 2010). CryoSat-2 was launched into a 369-day orbit with an Equator spacing of 7.5 km in May 2010. The Environmental Satellite (Envisat) mission was moved out of its 35-d exact repeat track to fly a new drifting track in 2010 October, where it remained until its demise in 2012 April. The new track had a 30-day cycle, and combining the data from this phase of the mission with ten years' worth of data from the repeat phase leads to

dense coverage at high latitudes. In 2012 May, Jason-1 began a geodetic mission in a 406-day, 7.7 km spacing at Equator orbit. Each of these missions collects ocean data at a $\sim$ 2 kHz pulse repetition frequency (PRF), thought to maximize the number of statistically independent measurements per second (Walsh, 1974, 1982) , and about double the $\sim$ 1 kHz PRF of Geosat and ERS-1.

The Synthetic Aperture Radar/Interferometric Radar Altimeter (SIRAL) instrument on CryoSat-2 has three measurement modes (Wingham et al., 2006) and switches among these autonomously as the spacecraft flies through a geographical 'mode mask' (European Space Agency, 2013). The standard Low Resolution Mode (LRM) is the conventional pulse-limited radar altimeter mode that has been used by all previous radar altimeters (black lines in Fig. 1). This mode requires a relatively low-data bandwidth and is ussed continuously over all ice-free ocean areas. The new Synthetic Aperture Radar (SAR) mode is used over ocean areas where sea ice is prevalent as well as a few small test areas (green lines in Fig. 1). In this mode the radar sends a burst of pulses every 11.8 ms. Within each burst, the interval between pulses is 55 μs long (ESRIN & University College London, 2013; Galin et al., 2013). The returning echoes are processed coherently in the along-track direction forming a 26-m long synthetic aperture. This results in a footprint that is beam-limited and narrow (0.29 km) in the along-track direction and pulse-limited and broad (1.53 km) in the cross-track direction (Ford & Pettengill, 1992; Raney, 1998). In addition, the echoes are sorted by Doppler frequency, allowing for the formation of distinct radar-illuminated beams along the satellite ground track. The locations of these beams can be described by a 'look' angle measured with respect to nadir. The return signals from multiple beams can be combined after performing range migration (Wingham et al., 2004), in a process termed 'multilooking', or 'multilook averaging'. There is a third mode of operation to measure elevation and cross-track slope over land ice surfaces where there is significant topographic slope (red lines in Fig. 1). This SAR/Interferometric Radar Altimeter (SARIN) mode utilizes the two antennas on CryoSat-2 to form a cross-track interferometer. The echoes received by each antenna undergo Doppler beam processing as in SAR mode, but the number of waveforms averaged is lower

due to the longer interval between bursts of 47.17 ms for SARIN mode. Both the SAR and SARIN modes require a very high bandwidth data link to the ground stations. CryoSat-2's SAR and SARIN modes were designed for measurements of sea ice and grounded ice, respectively (Wingham et al., 2006), but some data in these modes have been collected over ocean areas (Giles et al., 2012; Galin et al., 2013) for experiments which range from the observation of mesoscale sea surface variability (Dibarboure et al., 2012) to the recovery of the short-wavelength gravity signal (Stenseng & Andersen, 2012), with the latter being the main focus of the present paper. If all else were equal, SAR-mode altimetry should be about two times more precise than conventional altimetry (Jensen & Raney, 1998). However, CryoSat-2's implementation, in which the echoes from one burst are received before the next burst is transmitted, means that the instrument makes measurements only 30 percent of the available time, which is suboptimal (Raney, 2012) (Raney 2011). Thus, the performance gain, if any, of CryoSat-2's SAR and SARIN over its LRM, needs to be studied.

This paper addresses the following questions: (1) could the range measurements of these new altimeters be improved by the two-step retracking method Sandwell & Smith (2005) developed for ERS-1? (2) Could this method, which was developed for conventional 'pulse-limited' altimetry, be adapted to the CryoSat-2 SAR and SARIN cases where the radar waveform is both pulse-limited and also Doppler beam-limited? (3) When the method is applied to conventional waveforms acquired by averaging 2-kHz PRF echoes, how do the results compare with previous results obtained from the 1-kHz PRF instruments Geosat and ERS-1? (4) How do the CryoSat-2 SAR and SARIN results compare with those of the CryoSat-2 LRM and other conventional altimeters? (5) How does two-step retracking affect the spectral properties of the range measurements for the newer altimeters? This analysis would determine how well our techniques recover the various spatial scales that are present in the range signal.

As described above, we are only concerned with recovering the along-track ocean surface slope by estimating the range from consecutive radar altimeter waveforms. Therefore, our waveform model is less complex than is required for applica-

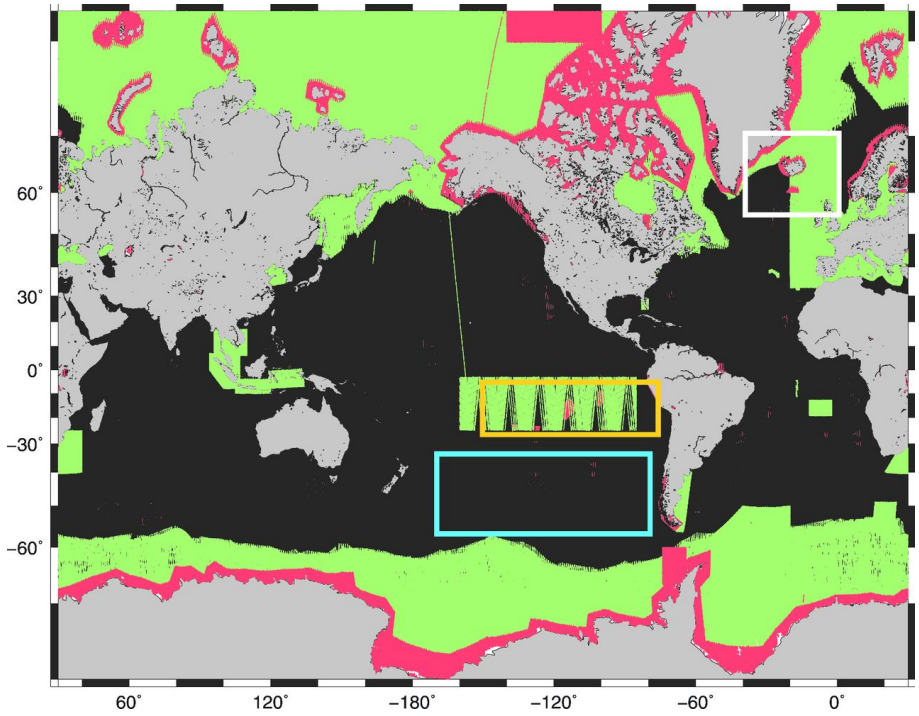

Figure 2.1: Ground tracks of 26 months of CryoSat-2 altimeter data (2010 July to 2012 August) in its three modes of operation LRM (black), SAR (green) and SARIN (red). Tracks from different modes that overlap in certain areas are due to changes in the geographical mode mask over the period of the mission. The area where altimeter noise was estimated for each instrument (see Fig. 2.5) is outlined by the white box, while the areas where the power spectra for sea level anomaly were computed for low and high significant wave height (SWH) conditions are outlined by the yellow and blue boxes, respectively. (see Fig. 2.7).

tions where absolute ocean surface height is needed. For example, we can neglect the effects of earth curvature, slow changes in antenna mispointing, and can use a Gaussian approximation for the point target response. We make these approximations for developing a simplified version of the analytical 'Brown' model for a conventional altimeter (Brown, 1977; Rodríguez, 1988; Amarouche et al., 2004). Then, using the same approximations, we develop an analytic formula for the shape of the SAR waveforms under the ideal condition of small radar mispointing angle. Analyticity is a virtue because it allows one to obtain the partial derivatives of least-squares model misfit with respect to model parameters, facilitating the search for a best-fit model by GaussNewton iterative steps. We evaluate the deficiencies of the analytical model through a comparison with a more fully developed waveform model (SAMOSA Project, Salvatore Dinardo 2012, personal communication) that also includes the effects of multilooking and radar mispointing (Wingham et al., 2004; Cotton et al., 2010). In addition, we show good agreement between our SAR retracking sea surface slope results and the slope derived from an independent analysis of the same data (Labroue et al., 2012).

Next, we show the results from least squares analysis of our waveform models applied to data from the different CryoSat-2 modes. Then, in order to assess the range precision of CryoSat-2, Envisat, and Jason-1 compared to ERS-1 and Geosat, we gathered all the data available for regions containing acquisitions from each of the CryoSat-2 modes. We quantified range precision by computing statistics on the range values produced by our retracking algorithms. In addition, we computed power spectral densities of the derived quantities such as sea level anomaly and significant wave height. Throughout these analyses, we compare the results obtained for data with and without two-step retracking. This allows us to discuss the benefits of applying this method in reducing the noise levels in range. Finally, we put our findings in context by examining the issue of correlated model errors during waveform retracking. The insights we have gained in this study have implications for understanding the contributions of each altimeter data set to the modelling of the global gravity field, which will be the focus of future work.

2.2 Waveform Models

A satellite altimeter senses the range to the sea surface by emitting a series of frequency-modulated chirp signals designed to act like brief radar pulses. These then interact with the ocean surface, and the received power of the reflected signal is recorded by the satellite altimeter over a short observation window, spanning 400 ns of travel time, equivalent to 60 m of range. Averages of the power received from many echoes are referred to as altimeter waveforms, and their shape may be described mathematically using a multiparameter model that is a function of the time elapsed since the signal transmission. The expected round-trip time varies by order 100 μs as the satellite moves around its orbit, and so the instrument employs a target tracking scheme to keep the sea surface echoes aligned within the observation window. Fitting a parametric model to the waveform is crucial to improving the estimate of range beyond what was estimated by the on-board tracker, and this parametric modelling is called 'retracking'.

The shape of the return radar waveforms collected by the altimeter can be described as a function of the delay time τ, which is the sampling time t referenced to the arrival time of the waveform t_0, such that $\tau = t - t_0$. The power versus delay time for the model radar return pulse $M(\tau)$ is given by the triple convolution of the point target response $P(\tau)$, the effective area of the ocean illuminated versus time $S(\tau)$, and the ocean surface roughness function $G(\tau)$ (Brown, 1977; Hayne, 1980; Chelton et al., 1989; Rodriguez & Martin, 1994; Chelton D.B. & P.S, 2001; Amarouche et al., 2004).

$$M(\tau) = P(\tau) * S(\tau) * G(\tau) \tag{2.1}$$

The source time function has the form $p_0 \left[\sin(\pi\tau/\tau_p)/(\pi\tau/\tau_p)\right]^2$ because the pulse is formed by deconvolution of a frequency modulated chirp, and p_0 is the peak power of the pulse. The bandwidth of the chirp is 320 MHz. This results in an effective pulse length, τ_p, of 3.125 ns, for an effective range resolution of the radar of 0.467 m. To simplify the convolution integrals, it is customary to approximate the source time function with a Gaussian function of the form

$$P(\tau) = p_0 exp\left(-\frac{\tau^2}{2\sigma_p^2}\right) \tag{2.2}$$

where σ_p is the standard deviation of the Gaussian function that models the point target response, and is related to the effective pulse length by $\sigma_p = 0.513\tau_p$ (Amarouche et al., 2004). This approximation leads to a range bias of about 1 cm and could be corrected using a lookup table (Thibaut et al., 2010). We do not apply this correction because the slope of this correction will be much less than 1 μrad. The roughness of the ocean surface due to ocean waves is also well approximated by a Gaussian function (Stewart, 1985).

$$G(\tau) = \frac{2}{\sigma_h c\sqrt{2\pi}} \exp\left(-\frac{\tau^2}{2\sigma_h^2}\right) \tag{2.3}$$

where σ_h is related to the significant wave height h_{SWH} by

$$\sigma_h = \frac{h_{\mathrm{SWH}}}{2c} \tag{2.4}$$

where c is the speed of light. The order of the triple convolution given in eq. (2.1) is unimportant so we begin by convolving the Gaussian approximation to the source function with the Gaussian wave height distribution resulting in

$$P(\tau) * G(\tau) = PG(\tau) = \frac{2p_0}{\sigma c\sqrt{2\pi}} \exp\left(-\frac{\tau^2}{2\sigma^2}\right) \tag{2.5}$$

where $\sigma^2 = \sigma_h^2 + \sigma_p^2$.

We note that for the purpose of recovering gravity from sea surface slopes the absolute scaling of eq. (2.5) is arbitrary, as we do not seek to recover calibrated values of the radar backscatter. The final convolution of the Gaussian pulse with the effective area of the ocean illuminated by the radar determines the shape of the model waveform.

The treatment that we present below to obtain the flat surface response $S(\tau)$ is meant to illustrate that the difference between the pulse-limited and SAR mode waveform models originates from the contrast in the geometries of the areas effectively illuminated by the radar pulse on the sea surface. To facilitate this, we will make the assumption that the diameter of the pulse-limited footprint is

much less than the diameter of the antenna beam pattern so the variation in antenna power within the pulse-limited area is small and can be approximated as a constant. This approximation will break down when the off-nadir pointing angle reaches a large fraction of the antenna beam angle. However, multiplying an ad hoc exponential decay function to the effective illuminated area results in the same functional form as a derivation of the flat surface response that takes into account the finite width of the radar antenna gain pattern, up to within a multiplicative factor (Appendix 2.A). Since we are most interested in measuring the arrival time of the return pulse, our analysis is not concerned with the amplitude of the pulse and thus our methods are sufficient for the sole purpose of measuring sea surface slopes.

2.3 Simplified Brown Model

Over the ocean the CryoSat-2 altimeter is operated in two modes (Fig. 2.2). The SIRAL antenna is slightly elliptical, but for LRM we consider the pulses as having approximately spherical wave fronts. The wave front reflects from an annulus on the ocean surface having an area $A(r) = 2\pi r dr$, where r is the radius of the annulus and dr is the width of the annulus. The approximate radius of the annulus versus time is given by (Walsh et al., 1978; Hayne, 1980; Stewart, 1985)

$$r(\tau) \approxeq \left(\frac{hc\tau}{\kappa}\right)^{1/2} \tag{2.6}$$

in which h is the altitude of the radar antenna above the surface, and c is the propagation speed of the radar pulse. The factor $\kappa = 1 + h/R$ accounts for the curvature of the earth, R Rodríguez (1988). While the radius of the annulus increases as the square root of time, the thickness of the annulus per unit time decreases as the square root of time. This can be seen by approximating the thickness of the annulus dr and by the rate of growth of the radius of the encircling ring

$$\frac{dr}{d\tau} \approxeq \frac{1}{2}\left(\frac{hc}{\kappa\tau}\right)^{1/2} \tag{2.7}$$

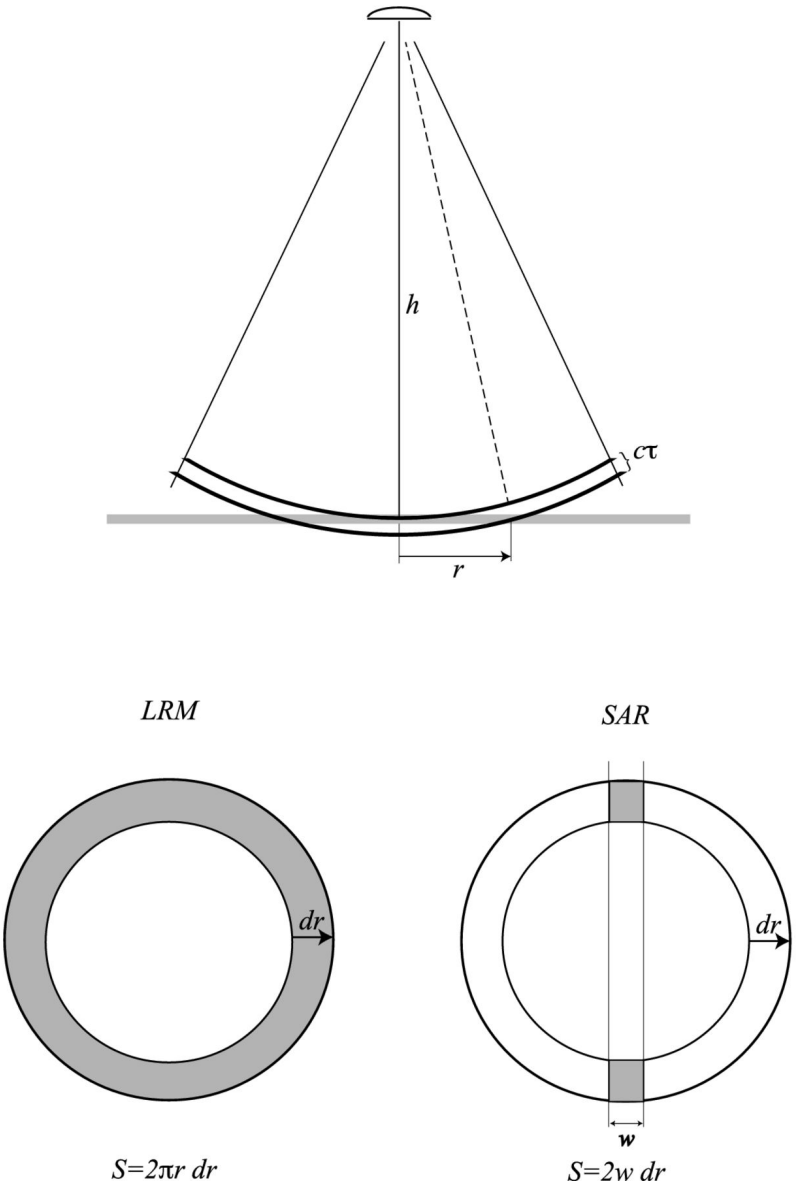

Figure 2.2: Interaction of a radar pulse with a flat surface. Area illuminated in standard LRM mode after the arrival of the pulse (left-hand side). Area illuminated by the synthetic aperture radar (SAR) method where w is the effective width of the focused beam in the along-track direction (right-hand side).

and so therefore the area of the annulus as a function of τ is uniform after the arrival of the pulse:

$$S(\tau) = \frac{\pi hc}{\kappa} H(\tau) \tag{2.8}$$

The final step in generating the model waveform is to convolve the effective area versus time with the Gaussian pulse function

$$M(\tau) = P(\tau) * G(\tau) * S(\tau) = \frac{hc}{\sigma\kappa}\sqrt{2\pi} p_0 \int_{-\infty}^{\infty} \exp\left[-\frac{\tau - \tau'}{2\sigma^2}\right] H(\tau') d\tau' \tag{2.9}$$

Integrating (2.9) using formula 7.4.2 in Abramowitz & Stegun (1964) results in the familiar 'Brown model' (Brown, 1977) waveform model

$$M(\tau) = \frac{hc\pi p_0 \sqrt{2}}{\kappa} \left[1 + \mathrm{erf}(\eta)\right] \exp(-\alpha\tau) = \frac{A}{2}\left[1 + \mathrm{erf}\left(\frac{\tau}{\sqrt{2}\sigma}\right)\right] \exp\left(-\alpha\tau\right) \tag{2.10}$$

where A is a scaling factor similar to a peak amplitude and $\eta = \tau/\sqrt{2}\sigma$. The exponential decay accounts for the antenna's gain pattern under the assumption that the line of maximum antenna gain makes an angle with nadir (the 'mispointing' angle) which is small compared to the antenna's beam width (Rodríguez, 1988; Amarouche et al., 2004). Also assumed in (2.10) is that the antenna gain pattern is circular. This is correct for all altimeter satellites except CryoSat-2, which has a slightly elliptical antenna pattern; however, CryoSat-2 conventional mode waveforms can be adequately approximated by assuming a circular pattern having a beam width squared equal to the harmonic mean of CryoSat-2's actual major and minor beam widths squared (Wingham & Wallis, 2010; Smith & Scharroo, 2011; Smith et al., 2011).

The partial derivatives of the model with respect to t_0, σ, and A are approximately

$$\frac{\partial M}{\partial t_0} = -\frac{A}{\sigma\sqrt{2\pi}} \exp(-\eta^2) \tag{2.11}$$

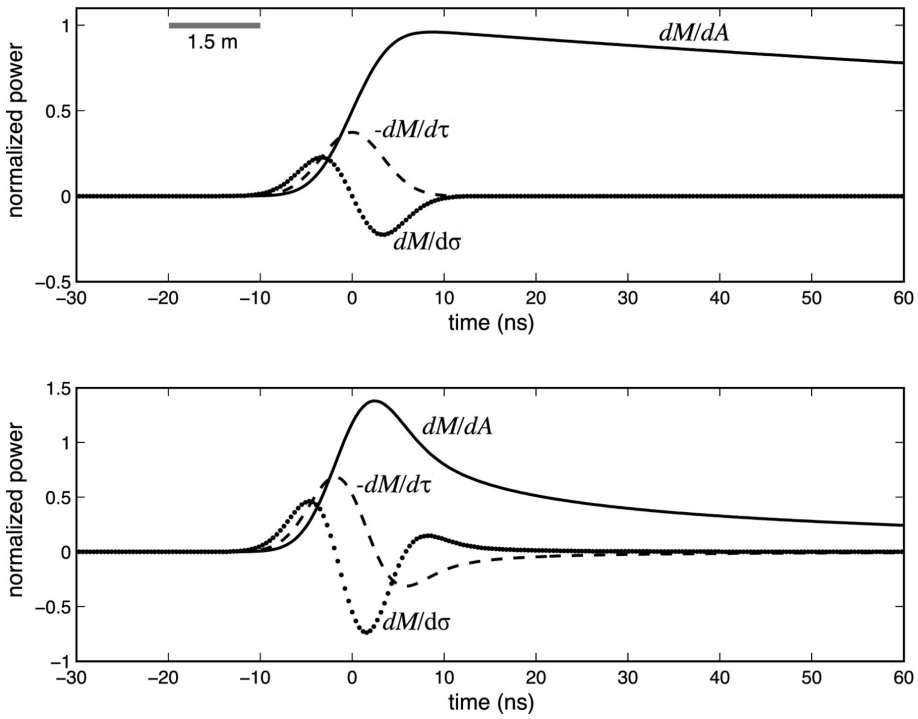

Figure 2.3: Brown model waveform including the exponential approximation to the trailing edge decay for a 2 m SWH (upper). Model derivatives with respect to arrival time (dashed) and rise time (dotted) are also shown. SAR model waveform for a 2 m SWH and including the exponential decay of the trailing edge approximating the antenna gain effect. Model derivatives are also shown (lower).

$$\frac{\partial M}{\partial \sigma} = -\frac{A}{\sigma\sqrt{\pi}}\eta \exp(-\eta^2) \tag{2.12}$$

$$\frac{\partial M}{\partial A} = \frac{M}{A} \tag{2.13}$$

respectively. Note that to simplify these expressions and the least squares analysis we have assumed that the slope of the exponential decay with respect to time is smaller than the more important leading terms. Plots of this simplified Brown model and its partial derivatives are provided in Fig. 2.3 (upper).

2.4 Approximate SAR Model

A similar approach is used to develop the waveform shape for the SAR model as well as its derivatives with respect to the model parameters. When CryoSat-2 operates in its SAR mode, the PRF is high enough to allow Doppler beam sharpening. Processing a group of 64 echoes yields 64 Doppler beams, fanned out in the direction of flight (Raney, 1998). One of these beams looks at nadir while the others look fore and aft; each subtends a width w along the ground. By selecting data from a particular beam, one may select slices through the annulus sampled by the radar pulse (Fig. 2.2b). Here, we will develop a simple expression approximating the mean power expected from only the nadir-looking beam having an effective width w in the along-track direction (Raney, 1998; Wingham et al., 2004). An assessment of the effects of using a nadir-only beam model to fit a multilooked waveform with small off-nadir pointing angle is provided in Appendices 2.B and 2.C. In this case the area of the illuminated ocean surface is approximately given by

$$S(\tau) \approxeq 2w\frac{dr}{d\tau}H(\tau) \tag{2.14}$$

when $w \ll r$ 2.2. So by again invoking eq. (2.7), the area versus delay time function is given by

$$S(\tau) = w\left(\frac{hc}{\kappa\tau}\right)^{1/2} H(\tau) \tag{2.15}$$

The model return waveform is the convolution of the Gaussian pulse with this area versus time function

$$M(\tau) = P(\tau) * S(\tau) * G(\tau) \quad = \frac{wp_0}{\sigma}\left(\frac{2hc}{\kappa\pi}\right)^{1/2} \int_{-\infty}^{+infty} \exp\left[-\frac{(\tau-\tau')^2}{2\sigma^2}\right] \tau'^{-\frac{1}{2}} \tag{2.16}$$

This integration, including an approximation to the CryoSat-2 antenna beam pattern, is provided in Appendix 2.A. The final result is

$$M(\tau) = A\sigma^{-\frac{1}{2}} \exp\left(-\frac{\tau}{4\sigma^2}\right) D_{-1/2}\left(-\frac{\tau}{\sigma}\right) \exp\left(-\alpha\tau\right) \tag{2.17}$$

where $D_n u(z)$ is the parabolic cylinder function of order ν and argument z.

As in the case of the Brown model, we would like to compute the partial derivatives of the model with respect to t_0, σ, and A. The details are provided in Appendix 2.A, but we summarize the results here:

$$M = A\sigma^{-\frac{1}{2}} \exp\left(-\frac{1}{4}z^2\right) D_{-1/2}(z) \exp\left(-\alpha\tau\right) \tag{2.18}$$

$$\frac{\partial M}{\partial t_0} = -A\sigma^{-\frac{3}{2}} \exp\left(-\frac{1}{4}z^2\right) D_{1/2}(z) \tag{2.19}$$

$$\frac{\partial M}{\partial \sigma} = -A\sigma^{-frac32} \exp\left(-\frac{1}{4}z^2\right) \left[\frac{1}{2}D_{-1/2}(z) - zD_{1/2}(z)\right] \tag{2.20}$$

$$\frac{\partial M}{\partial A} = \frac{M}{A} \tag{2.21}$$

where $z = -\tau/\sigma$. As in the case of the Brown model we simplify these expressions by assuming that the slope of the exponential decay with respect to time is smaller than the more important leading terms. Plots of this SAR model and its derivatives are provided in Fig. 2.3 (lower).

2.5 Least Squares Analysis

The standard approach in operational oceanography is to retrack the waveforms of conventional altimeters by fitting a mathematical model as in eq. 2.10. One such technique has been referred to as MLE (Amarouche et al., 2004; Thibaut et al., 2010). If the retracker fits four unknown parameters A - amplitude, t_0 - arrival time, σ -rise time and α - trailing edge decay, it is commonly called 'MLE4', while if the trailing edge decay parameter α is held fixed, then it is called 'MLE3'. In prior work (Sandwell & Smith, 2005) and in this study, we use a least-squares approach, which we call 3-parameter retracking. For our algorithm, the criteria for convergence depends on the following misfit function

$$\chi_2 = \sum_{i=1}^{N} \left(\frac{P_i - M(t_i; t_0, \sigma, A)}{W_i} \right)^2 \tag{2.22}$$

where the summation is over N waveform power samples. The waveform model M is evaluated for every t_i, and a starting model is calculated from some initial estimates A^0, σ^0 and t_0^0 for the fitting parameters. The best fitting model is found through successive iteration, and at each iteration the differences between the new parameter values A^{j+1}, $^{j+1}$ and t_0^{j+1} and the current values A^j, σ^j amd t_0^j are found by solving the following linear system:

$$\begin{bmatrix} P_1 - M_1^j \\ P_2 - M_2^j \\ \vdots \\ \vdots \\ P_N - M_M^j \end{bmatrix} =$$

$$\begin{bmatrix} \frac{\partial}{\partial t_0} M(t_1; t_0^j, \sigma^j, A^j) & \frac{\partial}{\partial \sigma} M(t_1; t_0^j, \sigma^j, A^j) & \frac{\partial}{\partial A} M(t_1; t_0^j, \sigma^j, A^j) \\ \vdots & \vdots & \vdots \\ \vdots & \vdots & \vdots \\ \frac{\partial}{\partial t_0} M(t_N; t_0^j, \sigma^j, A^j) & \frac{\partial}{\partial \sigma} M(t_N; t_0^j, \sigma^j, A^j) & \frac{\partial}{\partial A} M(t_N; t_0^j, \sigma^j, A^j) \end{bmatrix} \begin{bmatrix} t_0^{j+1} - t_0^j \\ \sigma^{j+1} - \sigma^j \\ A^{j+1} - A^j \end{bmatrix} \tag{2.23}$$

In the case of non-uniform weights, (2.23) should be modified by dividing both sides of the i-th equation by the weights W_i. The expressions for the partial derivatives of the model with respect to the parameters are given by eqs (2.11)-(2.13)) for the conventional pulse-limited waveform, and eqs (2.19)-(2.21) for the SAR mode waveform. The partial derivatives are then evaluated for the set of parameter values at each step j and at every gate i. The weights W_i in eq. (2.22) represent the uncertainty in the recorded waveform power, and for the conventional pulse-limited waveforms we use the functional form

$$W_i = \frac{(P_i + P_0)}{K^{\frac{1}{2}}} \tag{2.24}$$

where K is the number of statistically independent return echoes averaged to produce a 20 Hz waveform and P_0 is a power offset value. It is necessary to account for the offset P_0 as waveform values should contain a background noise level caused by temperature-dependent thermal noise in the receiver; the overall level is set by the engineering characteristics of each altimeter and varies with the automatic gain control setting. We arrive at the functional form of eq. (2.24) because theoretical considerations (Brown, 1977) show that since the radar amplitude follows a Rayleigh distribution, then the standard deviation in the signal component of the waveform value should be proportional to the mean of this component.

Two previous studies (Maus et al., 1998; Sandwell & Smith, 2005) showed that for weighted 3-parameter retracking, there is a strong covariance between the estimation errors in the arrival time and rise time parameters resulting in a relatively noisy estimate of arrival time. Moreover, if the rise time parameter is held to a fixed value (derived from about 40 km of along-track waveforms), then the results of Monte Carlo simulations show that the noise in arrival time is reduced by 36 percent, or a factor of 1.57 (Sandwell & Smith, 2005) (Fig. 2c). We refer to this approach as 2-parameter retracking. As shown below, while there are significant benefits in terms of range precision by reducing the number of parameters for the CryoSat-2 LRM and other conventional altimeter data, there seems to be no benefit in applying this approach to the SAR-mode data.

In this study we sought an optimal algorithm for retracking CryoSat-2 LRM and other conventional waveforms by fitting (eq.2.10) and CryoSat-2 SAR waveforms by fitting (eq. 2.18). Our optimization of the method is based on trial and error using tens of long ocean tracks and selecting the best method based on minimizing the median absolute difference between the along-track ocean slope, filtered at 18 km wavelength, and the slope of the ocean surface extracted from the EGM2008 global gravity model (Pavlis et al., 2012). The parameters we tuned are the trailing edge decay rate α, the power offset P_0 in eq. (2.24), and the number of waveforms to assemble into a single least-squares analysis.

The α value should depend on the antenna beam width, the altitude of the orbit, and the square of the off-nadir pointing angle. Height variations around the

orbit have negligible effect on α and the only important source of variation in α is variation in the spacecraft mispointing. Geosat had large mispointing excursions (order 0.7 °, a large fraction of its beamwidth) because it was only passively stabilized, but the other altimeter spacecraft actively maintain nadir pointing to a high enough accuracy that we chose to use a constant value for for these other satellites, for two reasons. First, allowing the parameter to vary rapidly along a satellite track will increase the noise in the range precision, particularly in areas of large wave height (Smith & Scharroo, 2011). Secondly, we found that the rate of change of mispointing angle is usually very small, so that any range bias we might introduce by assuming a constant α will introduce negligible error in the along-track sea surface slope required for gravity. Thus, for our purpose a constant α is a good assumption, although it might not be if absolute accuracy in ocean height were a requirement (Thibaut et al., 2010). The α values we found, expressed in units of (waveform range gate sample)-1, are: 0.022-ERS-1; 0.090-Envisat; 0.0058-Jason-1; 0.0130-CryoSat-2/LRM; 0.0149-CryoSat-2/SAR (0.00744-for the baseline B product). For Geosat, a mean value of 0.006 was used to initialize a best-fit search for α.

The second type of tuning was related to the weight function used in the least-squares analysis. The parameters in eq. (2.24) were tuned to achieve the best fits between along-track slope and EGM2008 slope for numerous profiles. It is interesting that all the Brown-type waveforms (Geosat, ERS-1, Envisat, Jason-1 and CryoSat-2/LRM) required a significant downweighting of the higher power data (as expected from the Rayleigh distribution theory) while the CryoSat-2 SAR waveforms had best fits when a uniform weight was used, meaning that instead of eq. (2.24) we simply set $W_i = P_0/K^{1/2}$ for all values P_i in the waveform window considered.

The third type of tuning is the number of 20 Hz waveforms to be used in each least-squares adjustment. In a previous study involving ERS-1 (Sandwell & Smith, 2005) we found optimal along-track slope fits when three waveforms were used and the two outer waveforms were given $\frac{1}{2}$ the weight of the central waveform. This approach proved optimal also for CryoSat-2/LRM and SAR and

we simply adopted the same weighting scheme for Envisat and Jason-1. Note that Geosat waveforms are provided at 10 Hz and we found that fits to single waveforms provided optimal results. Later when the 20-Hz noise levels of each altimeter are presented, the Geosat values will be multiplied by a factor of 1.41 to account for the reduced number of independent waveforms in the least-squares adjustment.

Examples of fits to the three modes of CryoSat-2 data are provided in Fig. 2.5. The left plot shows fits to the LRM data using the 2-parameter Brown model. As described in the Sandwell & Smith (2005) study, a two-step retracking approach was used. The data are assembled into continuous tracks of 20-Hz waveforms. A three-parameter retracking is performed during the first step; then the rise time parameter is smoothed over a $\frac{1}{2}$-wavelength of 45 km and then the pass is retracked a second time using this fixed value of rise time. A similar approach is used for the SAR and SARIN data. In all cases the model and the data show good agreement with one notable exception where the 'toe' (the onset of the rise of the leading edge) of the SAR and SARIN waveforms is not well matched by the model. This toe is due to multilooking the SAR waveforms to improve their signal-to-noise ratio and is not properly fit by our model, which was derived by considering the nadir-looking Doppler beam only. The adverse effects of fitting a multilooked waveform using a single-look model are evaluated in Appendix 2.B and 2.C. The three lower plots in Fig. 4 show the waveform residuals for 100 waveforms in each case. As expected the misfit to the LRM waveform is greater where the power is greater and there is no systematic variation to the misfit. The misfit to the SAR waveform shows a prominent leading edge signature cause by a poor match at the 'toe'.

2.6 Noise and Coherence

To assess the noise levels of the altimeter range data we perform a statistical analysis on the retracked range values. Meanwhile, to estimate the along-track spatial resolution of these measurements we carry out a cross-spectral calculation on data from repeating tracks. For the first approach, we compute the standard deviation of the 20 Hz range estimates about the 1 Hz mean (Cheney & Coast,

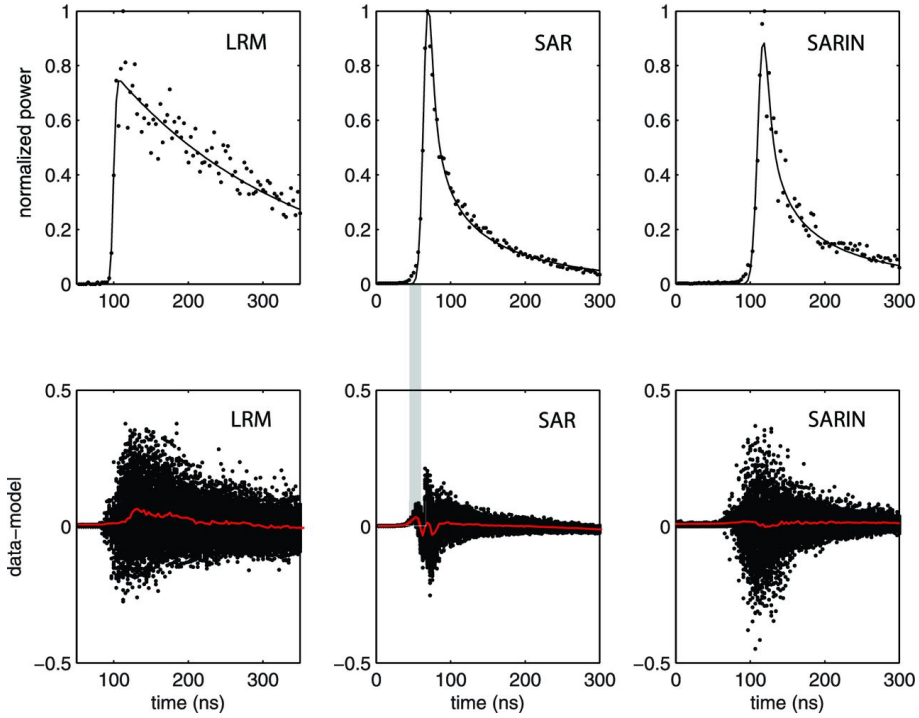

Figure 2.4: Least-squares fit of model waveforms to LRM, SAR and SARIN data. Residuals shown below are misfits from 1000 waveforms to reveal scatter as well as systematic variations (red). The SAR model single-look waveform does not match the 'toe' in the waveform data resulting in a systematic misfit (vertical grey line).

1992; Gommenginger et al., 2011). Rather than simply using the mean, we first removed a reference geoid model (EGM2008) because high geoid gradients within the 1-s time frame can increase the standard deviation. We selected a rectangular region in the North Atlantic such that the CryoSat-2 passes collected in the western half were mostly in LRM mode, while the eastern half contained SAR-mode data. We plotted this 20 Hz estimate versus SWH (white box in Fig. 2.1). We did the same analysis for Geosat, ERS-1, Envisat and Jason-1, as shown in Fig. 2.5. This was done for 3-parameter (green dots) and 2-parameter (blue dots) retracking. The solid smoothed curves are median averages of these estimates in 0.4 m SWH bins. Noise estimates of each altimeter at 2 m and 6 m SWH are provided in Table 1. To compare the statistics from our 3-parameter retracking to the MLE4 data provided with the standard Jason-1 Geophysical Data Record (GDR; (Picot et al., 2012)), we plotted the 20 Hz standard deviations provided in the GDR (red dots Fig. 2.5) and also computed the median of the 20 Hz noise in 0.4 m SWH bins. The GDR noise level is slightly lower than our 3-parameter noise level for SWH less than 3 m and greater at larger SWH. We note that the altimeter range and SWH estimated by the retracker during Jason-1 data processing chain are corrected using look up tables. These corrections are meant to alleviate the errors in range and SWH that are introduced by approximating the point target response by a Gaussian function. Note that the Jason-1 noise level for our 2-parameter retracked data is significantly lower than the GDR noise level showing that this two-step retracking approach reduces range noise at the very short wavelengths.

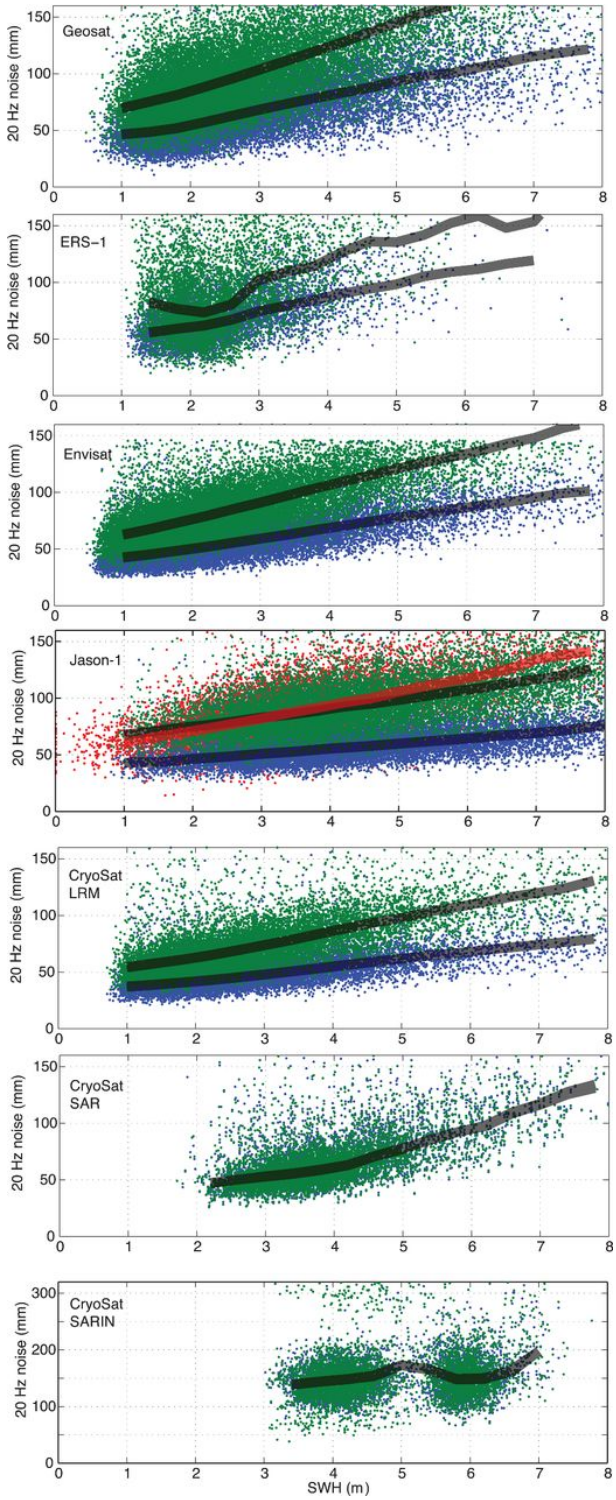
Geosat
ERS−1
Envisat
Jason-1
CryoSat
LRM
CryoSat
SAR
CryoSat
SARIN
20 Hz noise (mm)
SWH (m)

Figure 2.5 *(previous page)*: Standard deviation of retracked 20-Hz height estimates with respect to EGM2008 for all altimeter data considered in this study (Geosat, ERS-1, Envisat, Jason-1 and CryoSat-2 LRM, SAR and SARIN). The data are from a region of the North Atlantic with relatively high sea state, white box in Fig. 1 except the SARIN data are from the South Atlantic. Green dots are from 3-parameter retracking while blue dots are from 2-parameter retracking (every 10th point plotted). The red dots on the Jason-1 plot are the 1-Hz noise estimates provided with the GDR (Picot et al., 2012). They show good agreement with the 3-parameter noise estimates from our retracking code. The thick lines are the median of thousands of estimates over a 0.4 m range of SWH. Note the 2- and 3-parameter results are nearly identical for the CryoSat-2 SAR data. The 10-Hz Geosat estimates were scaled by 1.41 to approximate the errors in at a higher sampling rate of 20 Hz.

As expected, the noise level of the SAR data is between 1.8 and 1.3 times better than the other altimeters when all retracking is done using three parameters. For 2 m SWH, our computed value of 49.7 mm differs by less than a 1 mm from those obtained using different SAR waveform retracking approaches (Giles et al., 2012; Gommenginger et al., 2012). This result is somewhat less than the expected factor of 2 improvement in range precision based on an engineering analysis (Jensen & Raney, 1998; Raney et al., 2003). There are two possible reasons why we have not achieved this factor of 2 improvement. First, it is possible that our fits to the SAR waveforms are suboptimal because our model does not include the toe-signal caused by multilooking. Secondly, the estimated factor of 2 improvement was based on an open-burst SAR design where the pulsing of the radar was continuous, rather than in discrete bursts (Raney, 2012). In the case of CryoSat-2 the radar operates in a closed-burst mode where 64 pulses are emitted and then pulsing stops until the echoes of these 64 have been recorded; this causes the radar to operate only about 1/3 of the time, and is a suboptimal design (Raney, 2012). The more interesting result is that in the case of 2-parameter retracking, the reduction in noise level

Table 2.1: Standard deviation of retracked 20-Hz height estimates with respect to EGM2008. The data are from a region of the North Atlantic with relatively high sea state. The values represent the median of thousands of estimates over a 0.4 m range of SWH. The 10-Hz Geosat estimates were scaled by 1.41 to approximate the errors at the 20-Hz sampling rate. Note in all cases except for the CryoSat-2 SAR and SARIN modes, the 3-PAR to 2-PAR noise ratio is close to the 1.57 value derived from a least-squares simulation (Sandwell & Smith, 2005) (Fig. 2c).

	2 m SWH		6 m SWH	
Altimeter	3-PAR (2 m)	2-PAR (2 m)	3-PAR (6 m)	2-PAR (6 m)
Geosat	88	57	1.54	105.4
ERS-1	93.6	61.8	1.51	111.8
Envisat	78.9	51.8	1.52	88.6
Jason-1	75.9	46.4	1.63	64.2
CryoSat-2 LRM	64.7	42.7	1.51	71.7
CryoSat-2 SAR	49.5	49.7	0.996	110.9
CryoSat-2 SARIN	138.5	138.7	0.998	148.6

of the SAR waveforms is small while for the non-SAR data the noise reduction is large and very close to the expected noise reduction of 1.57 based on a Monte Carlo simulation (Sandwell & Smith, 2005) (Fig. 2c). Indeed, for 2 m SWH the noise of the CryoSat-2 LRM is lowest (42.7 mm), followed by Jason-1 (46.7 mm) and then CryoSat-2 SAR (49.7 mm). At 6 m SWH Jason-1 has the lowest noise level of 64.2 mm followed by LRM (71.7 mm), Envisat (88.6 mm) and then SAR (110.9 mm). The relatively poor performance of the SAR-mode data at the larger wave heights could reflect the increase in arrival time error with increasing SWH shown in Fig. 2.B2.

It is notable that the noise levels of the new altimeters (Envisat, Jason-1 and CryoSat-2) are lower than the noise levels of the older (Geosat and ERS-1) altimeters. This is due to the nearly factor of 2 increase in PRF in the newer

altimeters. At a PRF of $\sim$ 2 kHz, about 100 returning echoes are averaged to construct one waveform if the sampling rate is set at 20 Hz, whereas around 50 waveforms are included when the PRF is at $\sim$ 1 kHz. This increase in averaging reduces noise in the recorded waveforms, and hence in the range estimates as well.

Another finding is that the ratio of 3-parameter retracking noise to 2-parameter retracking noise for conventional pulse-limited data is largely independent of altimeter. Our calculations of this noise reduction due to the two-step retracking process are very close to a previously published value (Sandwell & Smith, 2005) (Fig. 2c) based on a least-squares simulation (Table 2.1). Together with our other results in the current study, this consistency of the noise ratio in two-step retracking implies that the technique confers the same benefits regardless of the PRF, at least for a pulse-limited altimeter.

A second common approach to noise analysis is cross-spectral coherence analysis of repeating altimeter profiles (Marks & Sailor, 1986). Through this analysis we obtain the signal-to-noise ratio as a function of wavelength. In our case, the signal is the time invariant gravity field which is common to the repeating profiles and the noise is caused by retracker noise and time varying environmental noise. The value of coherence is close to 1 at longer wavelengths where the signal dominates, and is small ($<$0.2) where the noise dominates (Bendat & Piersol, 2011). This technique has been used to characterize the shortest wavelength resolvable in the along-track altimeter data (Marks & Sailor, 1986), an important factor for designing low-pass filters to be applied to the 20 Hz data prior to gravity field construction (Yale et al., 1995). A conservative estimate of the effective resolution of the along-track data is given by the wavelength at which the coherence level is 0.5.

We selected ground tracks within a region in the North Atlantic Ocean and assembled profile pairs that repeat to within about 1 km. This set of tracks included both LRM and SAR mode data, and we performed the coherence analysis separately for each mode. For data from both modes, results from 2-parameter retracking were used to compute the along-track slopes. To obtain statistically significant coherence estimates we used Welch's modified periodogram method on

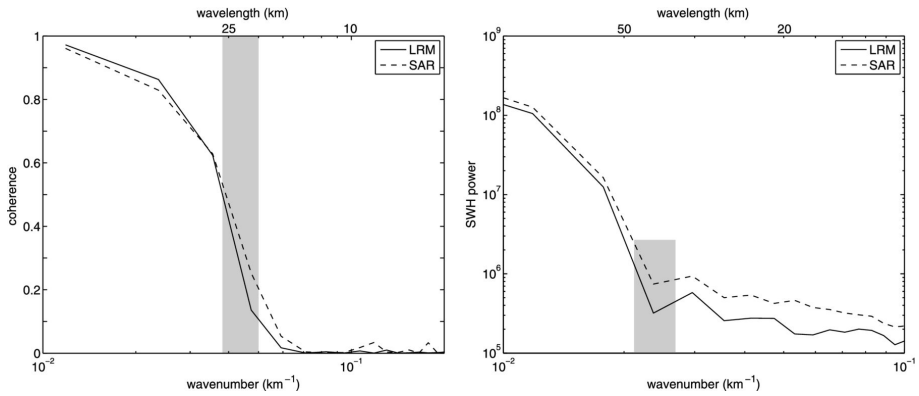

Figure 2.6: (a) Coherence versus spatial wavenumber (wavelength) for repeat along-track slope profiles in the North Atlantic (white box in Fig. 2.1). The LRM/SAR coherence falls to a value of 0.5 at a wavelength of 27/26 km and a value of 0.2 at a wavelength of 22/20 km. (b) Power in SWH versus wavenumber (wavelength) for 3-parameter retracking of LRM (solid) and SAR (dashed).

multiple passes. The data were pre-whitened by taking the along-track derivative, resulting in along-track slope. The resulting coherence curves are shown in Fig. 2.6. We found that LRM slope acquisitions have a resolution limit of 27 km, while for SAR, this was at 26 km. In comparison, previously published values using a similar analysis in another area of the Atlantic found a 33-km resolution for Geosat, and 33-km resolution for ERS-1 (Yale et al., 1995). These results suggest that the spatial resolution of CryoSat-2-derived gravity will be at least 1.2 times better than previous models.

The power spectrum of the SWH estimated in LRM and SAR mode data has a change in trend at a wavelength of 45 km (see Fig. 2.6b). This reflects the wavelength where the noise in the estimation of SWH is larger than the SWH signal. In the case of ERS-1 the break in the spectrum occurred at $\sim$ 90 km (Sandwell & Smith, 2005). Therefore, for our previous processing algorithms for the older altimeter data, we had used 90 km as the filter wavelength to smooth the SWH before 2-parameter retracking. However, our current analysis suggests that we should do less smoothing (45 km wavelength) for the CryoSat-2 data because the SWH is more accurately determined. This will provide better results in areas where there is a spatially rapid variation in swell height.

A previously unexplored issue related to this two-step retracking method is what part of the wavelength spectrum benefits most. This analysis was prompted by a study by Boy et al. (2012) where spectra of all altimeters show elevated power spectral density between the wavelengths of 45 and 5 km, which has been called a spectral 'bump'. We explored this issue in two ways. First, we computed the power spectra of sea level anomaly (SLA) from Jason-1 (i.e. sea surface heightEGM2008) for thousands of profiles in two large regions of the South Pacific (Fig. 2.7). The first area has generally high SWH and high mesoscale variability (black curves in Fig. 2.7) while the second area has generally low SWH and low mesoscale variability (blue curves in Fig. 2.7). The dashed curves are spectra for the 3-parameter retracked data while the solid curves are the spectra for the 2-parameter retracked data. In both cases the 3-parameter data has a higher power for wavelengths shorter than about 100 km. We believe this decrease in power in the 10 – 100-km wavelength band is caused by the lower noise level of the 2-parameter retracker with respect to the 3-parameter retracker. This same benefit was demonstrated using Geosat altimeter data (Sandwell & Smith, 2009) and the geographic variations in noise improvement are provided in Fig. 3 of that study; the noise reduction is greatest in areas of high SWH.

To further demonstrate the noise reduction for the 2-parameter retracker relative to the 3-parameter retracker for all the newer altimeters, we constructed power spectra of differences between the output from the two retrackers. These results are shown in Fig. 2.8. All the altimeters show elevated power spectral density between the wavelengths of 45 and 5 km, which corresponds to the spectral 'bump' (Boy et al., 2012). The fall-off in the difference spectra for wavelengths greater than 45 km simply reflects the wavelength over which the SWH was smoothed between the 3-parameter and 2-parameter retracking. At longer wavelengths, both retrackers provide the same height measurement because the profiles contain the same SWH signal. At shorter wavelengths there is a significant filtering of the SWH, so the retrackers provide very different output. At the shortest wavelength end of the difference spectrum between 10 and 3 km the outputs from the two retrackers also become similar. We speculate that this is due to the finite pulse-limited diameter

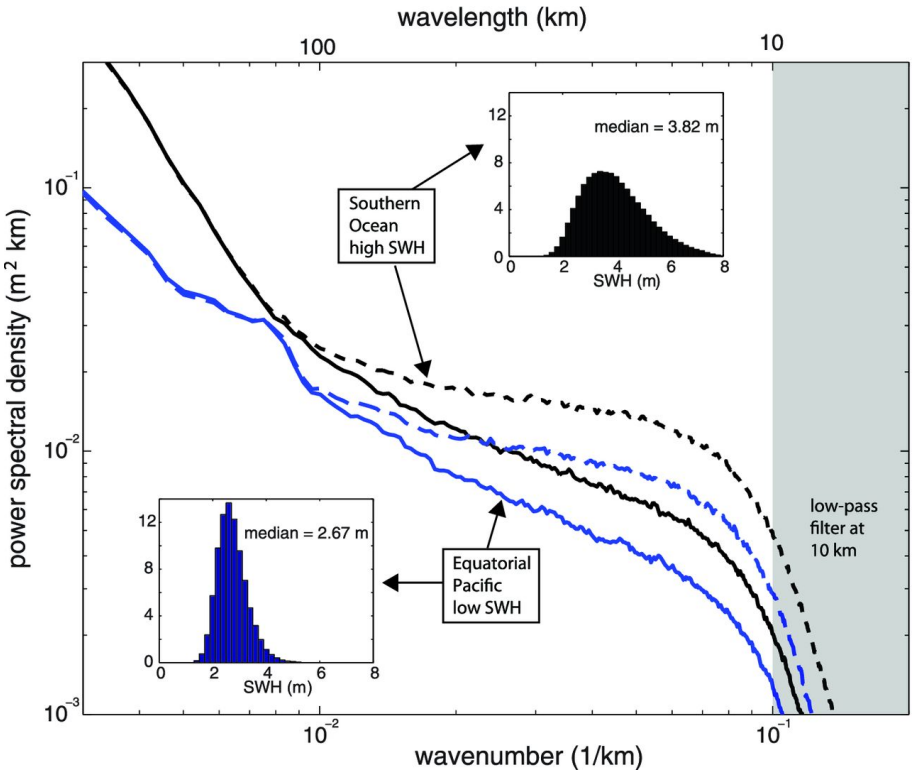

Figure 2.7: Power spectra for sea level anomaly (sea surface height minus EGM2008) as computed from Jason-1 data for two regions in the South Pacific. Dashed curves are 3-parameter retracking and solid curves are 2-parameter retracking. Black curves are from a region of generally high sea state and high mesoscale variability (longitude 190280, latitude 55 to 35, 5500 passes of length 2048). Blue curves are from a region of generally low sea state and low mesoscale variability (longitude 210285, latitude 25 to 4, 4200 passes of length 2048). Inset histograms show differences in sea state characteristics. The rapid spectral roll-off at 10 km wavelength is caused by a low-pass filter applied to the 20 Hz data prior to resampling at 5 Hz. The spectral 'bump' is more apparent for the 3-parameter retracked data than the 2-parameter retracked data. The spectra are smooth because they each represent about 10 million, 5 Hz observations.

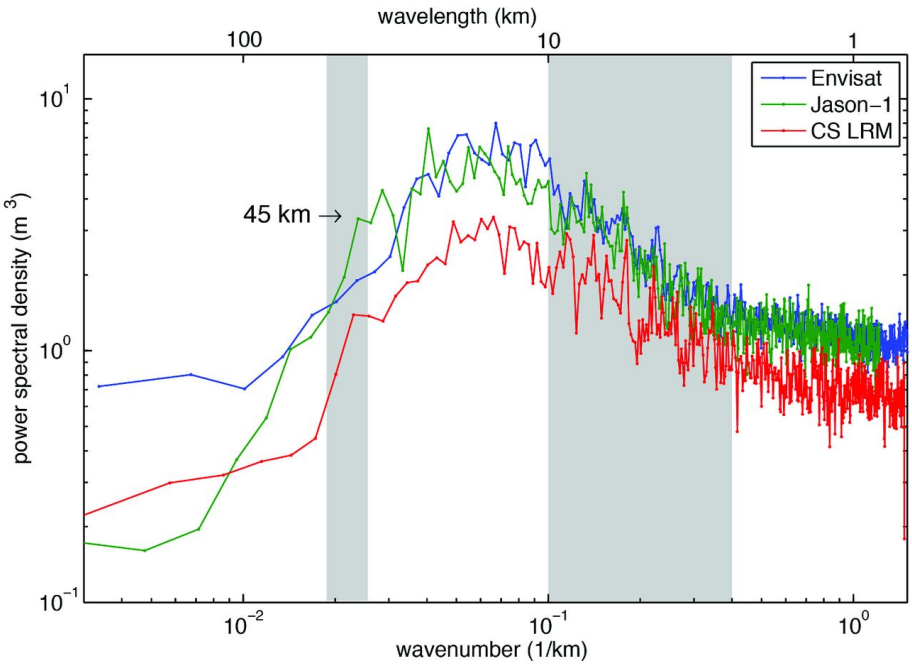

Figure 2.8: Power spectra (20 Hz) of the difference in along track height between passes retracked with the 3-parameter model and the 2-parameter model after smoothing the SWH over a 1/2-wavelength of 45 km. There is a 'bump' in the spectrum between 5 and 45 km where most of the noise reduction occurs.

of the radar footprint. We note that the shortest wavelength available in marine gravity models derived from altimetry is about 12 km so this finite footprint size is not yet a limitation on gravity field resolution. This analysis of the reduction in the spectral bump caused by SWH smoothing as well as the reduction in the correlation between residual height and SWH deserved further investigation but is somewhat beyond the scope of this paper.

2.7 Correlated Model Errors

One of the unexpected results from our analysis of the CryoSat-2 LRM and SAR waveform data is that the SAR data show no noise reduction when the two-step retracking approach is used. To investigate why this happens in the least squares fitting one can examine the 3×3 covariance matrix that is constructed

from the partial derivative of the model waveform with respect to the three model parameters A, t_0 and σ. The results are provided in Table 2.2 where the covariance values were scaled so the arrival-time variance is one. The analysis was done for both the LRM and SAR modes for SWH of 2 and 6 m. In general the SWH is more accurately estimated for the SAR than for the LRM (i.e. the σ-σ term of the covariance matrix). More important the cross correlation between σ and τ is relatively large for the LRM (0.27 at 2 m SWH and 0.43 at 6 m SWH). In contrast the cross correlation between and t0 is smaller for the SAR (0.11 at 2 m SWH and 0.19 at 6 m SWH).

Table 2.2: LRM and SAR least-squares covariance

	LRM				SAR		
	0.0678	0.1324	0.1379	A	0.1505	0.0714	0.2348
2 m	–	1.0000	**0.2694**	t_0	–	1.0000	**0.1115**
	–	–	1.3947	σ	–	–	1.0644
	A	t	σ		A	t	σ
	0.0441	0.1381	0.1392	A	0.0662	0.0749	0.1682
6 m	–	1.0000	0.4356	t_0	–	1.0000	0.1903
	–	–	1.3489	σ	–	–	1.0832

In hindsight, one might have expected these large correlations between σ and τ in LRM (found previously for ERS-1 by Sandwell & Smith (2005)) and smaller correlations in SAR from an inspection of the partial derivatives with respect to these parameters shown in Fig. 2.3. It seems clear that the two partial derivatives are more dissimilar in shape for SAR mode than in the LRM case, and so the SAR model fitting should be able to better discriminate between the two parameters. The two-step retracking of Sandwell & Smith (2005) was developed to overcome the problem of this correlation in ERS-1 (i.e. conventional, 'LRM') data. It appears that it is not needed for SAR data. One may speculate that the greater sensitivity to the model parameters in SAR data is ultimately due to the

waveform shape having both a leading and a trailing edge that changes with σ, whereas in our formulation the slope of the trailing edge of the conventional LRM waveform is unaffected by this parameter.

2.8 Conclusions

To measure marine gravity anomalies at an accuracy under 1 mGal, the error in the along-track slopes from the altimeter profiles must be about 1 μrad, or there must be enough repeated tracks to achieve the 1 μrad accuracy. This study compiles several contributions towards this goal.

We have shown that a simple analytic function, which we derived to model CryoSat-2 SAR-mode waveforms, may be used to estimate along-track sea surface slope. This is in spite of the fact that the model does not account for the multilook averaging applied in assembling the SAR waveforms. We then calculated the range precision at 20 Hz for a large set of altimeter profiles collected in SAR mode and found that it was almost two times better than earlier noise levels for ERS-1 and Geosat.

Two-step retracking was originally developed specifically for ERS-1 data (Sandwell & Smith, 2005), but we have established that this method also results in a factor of 1.5 improvement in range precision for pulse-limited altimetry waveforms for other missions. Yet we found no noise reduction from the second pass of retracking in the CryoSat-2 SAR- and SARIN-mode data. The range precision gained through the two-step retracking algorithm occurs over the 545-km wavelength band, which reduces the observed 'bump' in the sea level anomaly power spectrum. The 1.5 times improvement in range precision from the 2-step retracking, combined with the 1.4 times improvement in range precision due to the increased PRF of the newer altimeters, results in an overall factor of 2 improvement in range precision.

Taken together, advancements from SAR altimetry, as well as the application of two-step retracking to conventional altimetry, yield enhanced recovery of sea surface slopes from CryoSat-2, Envisat, and Jason-1 data when compared

to previous measurements from the geodetic missions of the Geosat and ERS-1 altimeters.

2.9 Acknowledgements

We thank Salvatore Dinardo of ESA ESRIN for providing simulation results for the CryoSat-2 SAR waveforms from the SAMOSA project. We thank the reviewers for their constructive criticism. Pierre Thibaut provided guidance in the finer points of processing Jason-1 and CryoSat-2 waveforms. We thank Robert Cullen for providing early access to the oversampled SAR waveform data. We thank Jerome Benveniste for encouraging us to use CryoSat-2 altimetry for gravity field improvement. Walter H.F. Smith contributed to the derivation provided in Appendix 2.A and helped to refine the other sections of the paper. The retracked CryoSat-2 SAR data were kindly provided by Nicolas Picot through the AVISO server. The CryoSat-2 and Envisat data were provided by the European Space agency, and NASA/CNES provided data from the Jason-1 altimeter. This research was supported by ConocoPhillips, the National Science Foundation (OCE-1128801), and the Office of Naval Research (N00014-12-1-0111). The manuscript contents are solely the opinions of the authors and do not constitute a statement of policy, decision, or position on behalf of NOAA or the U. S. Government.

Chapter 2, in full, is a reprint of the material as it appears in the Geophysical Journal International: Garcia, E.S., D.T. Sandwell, W.H.F. Smith, "Retracking CryoSat-2, Envisat and Jason-1 radar altimetry waveforms for improved gravity field recovery", *Geophysical Journal International*, 196(3): 1402-1422, doi: 10.1093/gji/ggt469, 2014. The dissertation author was the primary investigator and author of the paper.

Appendices

2.A Derivation of SAR Waveform Model

The model return waveform is the convolution of the combined point target response and wave height distribution $PG(\tau)$ with the area versus time function that is also called the flat surface response function $S(\tau)$.

$$M(\tau) = PG(\tau) * S(\tau) \tag{2.25}$$

Here, we develop an approximation to the flat surface response function and recover two dominant terms - the inverse square root of time dependence, and the exponential decay factor. This approach is similar to earlier efforts in modelling the CryoSat-2 SAR waveforms (Galin et al., 2013; Wingham & Wallis, 2010). The flat surface response is proportional to the integral of the product of the beam gain pattern $B(r, \theta)$ and the square of the one-way antenna gain pattern $G(r, \theta)$ over an infinitesimal ring of equivalent range:

$$S(\tau) = H(\tau) C \sigma^0 \int_0^{2\pi} B(\rho, \theta) G^2(\rho, \theta) \, \mathrm{d}\theta \tag{2.26}$$

Here, ρ is the radial coordinate, and θ is the azimuthal coordinate in a standard 2-D polar coordinate system. We have incorporated various constant values associated with the radar instrument design in the factor C, and σ_0 is the surface backscattering coefficient. For CryoSat-2, the antenna gain pattern can be written explicitly as

$$G(\rho, \theta) = G_0 \exp\left\{ - \left[\left(\frac{(\rho \cos\theta - \mu)^2}{\gamma_1^2} \right) + \left(\frac{(\rho \sin\theta - \xi)^2}{\gamma_2^2} \right) \right] \right\} \tag{2.27}$$

where G_0 is the boresight antenna gain. The along-track width of the antenna pattern is γ_1 while the across-track width is γ_2. The mispointing angles are denoted by μ for pitch and ξ for roll. We have not included the terms related to the surface gradient because they are very small over the ocean.

We take a somewhat different approach than that taken in Galin et al. (2013) for specifying the beam pattern. Their formulation incorporates a Hamming weighting function that is employed by the official ESA processing routine to form the synthetic Doppler beams. Meanwhile, in an earlier section of this study, we used a simplified model where the beam pattern was approximated using rectangular regions that decrease in area as the inverse square root of time (eq. 2.16). However, in forming the synthetic beam located in the nadir direction, a narrow frequency band about the zero Doppler point is selected as a result of the SAR processing. Thus, a more realistic beam pattern would be one that is represented by a sinc() function. To facilitate the evaluation of the ensuing integrals in the convolution, we approximate this using a Gaussian function, with γ_b taken to be the beam width:

$$B(r,\theta) = B_0 \exp\left[-\frac{(\rho\cos\theta)^2}{\gamma_b^2}\right] \tag{2.28}$$

and where B_0 accounts for the beam gain.

Upon making the assumption that the mispointing angles are small with respect to the angular extent of the antenna gain pattern, it may be shown that (2.27) can then be approximated by

$$\begin{aligned} S(\tau) \approxeq C_0 H(\tau) \int_0^{2\pi} & \exp\left[-\frac{(\rho\cos\theta)^2}{\gamma_b^2}\right] \\ & \times \exp\left\{-2\left[\left(\frac{(\rho\cos\theta-\mu)^2}{\gamma_1^2}\right)+\left(\frac{(\rho\sin\theta-\xi)^2}{\gamma_2^2}\right)\right]\right\} \mathrm{d}\theta \end{aligned} \tag{2.29}$$

where the factor C_0 has encapsulated several constants. This can be further manipulated using trigonometric identities,

$$\begin{aligned} S(\tau) \approxeq & C_0 H(\tau) \exp\left\{-\frac{\rho^2}{2}\left[\frac{1}{\gamma_b^2}+\left(\frac{1}{\gamma_1^2}+\frac{1}{\gamma_2^2}\right)\right]\right\} \\ & \times \int_0^{2\pi} \exp\left\{-\frac{\rho^2}{2}\cos 2\theta\left[\frac{1}{\gamma_b^2}+2\left(\frac{1}{\gamma_1^2}-\frac{1}{\gamma_2^2}\right)\right]\right\} \mathrm{d}\theta \end{aligned} \tag{2.30}$$

and after performing a suitable change of variables, the following integral representation of the modified Bessel function of order zero $I_0(x)$ can be invoked

$$\int_0^{2\pi} \exp(-x\cos\phi)\mathrm{d}\phi = 2\pi I_0(x) \tag{2.31}$$

such that (2.30) can be evaluated:

$$S(\tau) \approxeq 4\pi C_0 H(\tau) \exp\left\{-\frac{\rho^2}{2}\frac{\rho^2}{2}\left[\frac{1}{\gamma_b^2} + \left(\frac{1}{\gamma_1^2} + \frac{1}{\gamma_2^2}\right)\right]\right\} \times I_0\left\{\frac{\rho^2}{2}\cos 2\theta\left[\frac{1}{\gamma_b^2} + 2\left(\frac{1}{\gamma_1^2} - \frac{1}{\gamma_2^2}\right)\right]\right\} \tag{2.32}$$

A further simplification may be made if we assume that the beam width γ_b is narrow enough that the instrument's travel time resolution is insensitive to the along-track position of surface area elements within the beam, allowing for the use of the asymptotic form

$$I_0(x) \approxeq (2\pi x)^{-\frac{1}{2}} \exp(x) \tag{2.33}$$

Applying (2.33) to (2.32) leads to

$$S(\tau) \approxeq C_1 H(\tau) \frac{1}{\rho} \exp\left(-\frac{\rho^2}{\gamma_2^2}\right) \tag{2.34}$$

where again we have collapsed the preceding constants into a single factor C_1. Rewriting this in terms of τ by recalling (eq. 2.6), we get

$$S(\tau) \approxeq C_2 H(\tau) \tau^{-frac12} \exp\left(-\frac{hc}{\kappa\gamma_2^2}\tau\right) \tag{2.35}$$

As before, outlying constants have been gathered into C_2. From this expression we see that we recover the inverse square root of time dependence, as well as get an exponential decay factor. The decay rate is dependent on the across-track width of the antenna gain pattern.

If we assume a Gaussian functional form for both the point target response and the surface roughness distribution, then the convolution leading to the waveform model can be approximately written as the following integral, which is similar in form to (eq. 2.17):

$$M(\tau) = PG(\tau) * S(\tau)$$
$$\approxeq C_3 \int_{-\infty}^{+\infty} H(\tau'^{-\frac{1}{2}} \exp\left(-\frac{hc}{\kappa\gamma_2^2}\right) \exp\left(-\frac{(\tau-\tau')^2}{2\sigma^2}\right) \mathrm{d}\tau' \tag{2.36}$$

where C_3 is the product of several constants. After a bit of algebra one arrives at

$$M(\tau) = C_3 \exp\left(-\frac{\tau^2}{2\sigma^2}\right) \int_0^{+\infty} \tau'^{-\frac{1}{2}} \exp\left[-\left(\frac{1}{2\sigma^2}\right)\tau'^2 - \left(\frac{hc}{\kappa\gamma_2^2} - \frac{\tau}{\sigma^2}\right)\tau'\right] \mathrm{d}\tau' \tag{2.37}$$

Note that this integral can be performed analytically using the following formula (Gradshteyn & Ryzhik, 2000)

$$\int_0^{+\infty} \tau'^{-\frac{1}{2}} \exp\left(-p\tau'^2 - q\tau'\right) \mathrm{d}\tau' = (2p)^{-\frac{1}{4}}\Gamma\left(\frac{1}{2}\right) \exp\left(\frac{q^2}{8p}\right) D_{-1/2}\left(\frac{q}{(2p)^{\frac{1}{2}}}\right) \tag{2.38}$$

where $D_{-1/2}(x)$ is the parabolic cylinder function and $\Gamma(x)$ is the gamma function for some argument x. Note that $\Gamma(\frac{1}{2}) = \pi^{\frac{1}{2}}$. We make the substitutions $p = 1/(2\sigma^2)$ and $q = (hc/\kappa\gamma_2^2) - (\tau/\sigma^2)$ so the integral becomes

$$\int_0^{+\infty} \tau'^{-\frac{1}{2}} \exp\left[-\left(\frac{1}{2\sigma^2}\right)\tau'^2 - \left(\frac{hc}{\kappa\gamma_2^2} - \frac{\tau}{\sigma^2}\right)\tau'\right] \mathrm{d}\tau' =$$
$$C_4\sigma^{\frac{1}{2}} \exp\left[\frac{1}{4}\left(\frac{hc}{\kappa\gamma_2^2}\sigma\right)^2\right] \exp\left(-\frac{1}{2}\frac{hc}{\kappa\gamma_2^2}\right) \exp\left(-\frac{\tau^2}{4\sigma^2}\right) D_{-1/2}\left(\frac{hc}{\kappa\gamma_2^2}\sigma - \frac{\tau}{\sigma}\right) \tag{2.39}$$

Skipping some details, the final result is

$$M(\tau) \approxeq C_4\sigma^{\frac{1}{2}} \exp\left(-\frac{1}{2}\frac{hc}{\kappa\gamma_2^2}\sigma\right) \exp\left(-\frac{1}{2}\frac{hc}{\kappa\gamma_2^2}\tau\right) \exp\left(-\frac{\tau^2}{4\sigma^2}\right) D_{-1/2}\left(\frac{hc}{\kappa\gamma_2^2}\sigma - \frac{\tau}{\sigma}\right) \tag{2.40}$$

We take the term $hc\sigma/\kappa\gamma_2^2$ to be small, and thus the term $\exp(-hc\sigma/2\kappa\gamma_2^2)$ can be treated as being close to a constant, and the only remaining term for the argument of the parabolic cylinder function would then be $-\tau/\sigma$. Upon combining constants, we arrive at

$$M(\tau) \cong \exp\left(-\frac{\tau^2}{4\sigma^2}\right) D_{-1/2}\left(-\frac{\tau}{\sigma}\right) \exp(-\alpha\tau) \tag{2.41}$$

where $\alpha = hc/2\gamma_2^2$. This is the model provided in eq. (2.18) of the paper. The parameter A is related to the maximum amplitude of the recorded waveform.

As in the case of the Brown model, we would like to compute the partial derivatives of the model with respect to t_0, σ and A. The derivative of the model with respect to the amplitude parameter A is simply

$$\frac{\partial M}{\partial A} = \frac{M}{A} \tag{2.42}$$

To compute the other derivatives we make use of the identity (DLMF, 2010)

$$\frac{\partial}{\partial z}\left[\exp\left(-\frac{z^2}{4}\right) D_{-1/2}(z)\right] = -\exp\left(-\frac{z^2}{4}\right) D_{1/2}(z) \tag{2.43}$$

Now, we let $z = -\tau/\sigma$ Using the chain rule, the derivative with respect to t_0 becomes

$$\frac{\partial M}{\partial t_0} = \frac{\partial M}{\partial z}\frac{\partial z}{\partial t_0} \tag{2.44}$$

where $\partial z/\partial t_0 = 1/\sigma$ upon recalling that $\tau = t - t_0$.

Using the expression above, the derivative of the model M with respect to z is

$$\frac{\partial M}{\partial z} = -A\sigma^{-1/2} \exp\left(-\frac{z^2}{4}\right) D_{1/2}(z) \tag{2.45}$$

Combining terms one gets

$$\frac{\partial M}{\partial t_0} = A\sigma^{-3/2} \exp\left(-\frac{z^2}{4}\right) D_{1/2}(z) \tag{2.46}$$

A similar approach can be used to calculate the derivative with respect to σ:

$$\frac{\partial M}{\partial \sigma} = \frac{\partial M}{\partial z}\frac{\partial z}{\partial \sigma} \tag{2.47}$$

By rewriting the waveform model as $M = A\sigma^{-\frac{1}{2}} \exp(-z^2/4) D_{-1/2}(z)$, we can then form the derivative from the sum of two terms. The first term is

$$\left(\frac{\partial M}{\partial \sigma}\right)_1 = -\frac{1}{2} A\sigma^{-\frac{3}{2}} \exp\left(-\frac{z^2}{4}\right) D_{-1/2}(z) \tag{2.48}$$

The second term is

$$\left(\frac{\partial M}{\partial \sigma}\right)_2 = -A\tau\sigma^{-\frac{5}{2}} \exp\left(-\frac{z^2}{4}\right) D_{1/2}(z) \tag{2.49}$$

Recalling that $\partial z/\partial \sigma = \tau/\sigma^2$, and then by combining terms we find that

$$\begin{aligned} \frac{\partial M}{\partial \sigma} &= \left(\frac{\partial M}{\partial \sigma}\right)_1 + \left(\frac{\partial M}{\partial \sigma}\right)_2 \\ &= -A\sigma^{-\frac{3}{2}} \exp\left(-\frac{1}{4}z^2\right) \left[\frac{1}{2} D_{-1/2}(z) + \frac{\tau}{\sigma} D_{1/2}(z)\right] \end{aligned} \tag{2.50}$$

The results are summarized in eqs (2.19)-(2.21).

To obtain numerical values of the parabolic cylinder functions, we use Fortran subroutines that are based on a library for the computation of special functions (Zhang & Jin, 1996). The algorithms, in turn, are derived from polynomial approximations for certain ranges of the argument values as specified in (Abramowitz & Stegun, 1964). The subroutines were modified slightly to evaluate the entire expression $\exp(-z^2/4) D_{-1/2}(z)$ instead of just $D_{-1/2}(z)$.

2.B Assessment of Approximate SAR Model

Our approximation of the SAR waveform model shape is derived under the assumptions that: (1) only the nadir-looking Doppler beam contributes significantly to the multilooked waveform; (2) mispointing of the antenna is small compared to the antenna beamwidth; (3) the half-width of the nadir-looking Doppler beam is very narrow compared to the radius of the pulse-limited circle. It is clear from Fig. 2.4 hat our model is not correctly fitting the 'toe' of the waveform at

the onset of the rise of the leading edge, and from Fig. 2.5 that our model is not estimating very low values of SWH. In this appendix we compare our model to synthetic waveforms generated from a complete simulation of all of the important complications in both single-looked (at nadir) and multilooked SAR waveforms (Cotton et al., 2010).

The SAMOSA waveform model (Gommenginger et al., 2012) was developed from physical principles, leading to a simple analytical formulation to generate 2-D delay Doppler arrays of return power. Doppler beamforming and multilook averaging are then applied, resulting in a model that is a function of delay time and dependent on the parameters of SWH, backscatter and the roll and pitch mispointing angles.

Mispointing and multilooking can have important effects on the shape of the model waveform (Wingham et al., 2004; Cotton et al., 2010). To date there is no completely analytical expression for the shape of the multilooked SAR model waveform and its partial derivatives with respect to arrival time, SWH and off-nadir pointing angle. Computation of a fully accurate model (Phalippou & Enjolras, 2007) involves multiple numerical integrations and thus the only practical retracking approach will involve pre-computing models and partial derivatives for a suite of model parameters and building a retracking code that rapidly retrieves template models. This purely numerical approach will require extensive development and testing. Our aim is to avoid this heavy computation burden by making simplifications adequate for sea surface slope recovery. We stress that we are not trying to recover fully calibrated sea surface height, SWH or backscatter. This is in contrast to other efforts, such as the CNES Cryosat Processing Prototype (Labroue et al., 2012), that enlist numerical methods to estimate all these parameters.

We show next that under certain conditions of moderate SWH and small off-nadir pointing angle, our analytic model (eq. 2.18) is adequate for estimating along-track slope to better than 1 μrad. Moreover because the formulation has analytic derivatives with respect to the model parameters, we can retrack 12 months of CryoSat-2 SAR waveforms in about a day on a desktop computer. This rapid analysis enables us to explore and refine least-squares approaches and waveform

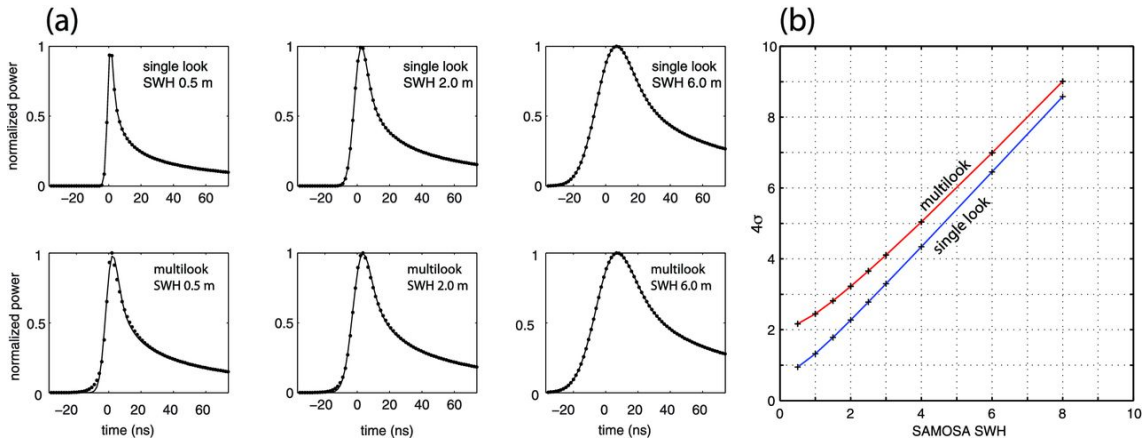

Figure 2.B.1: (a) Fit of analytic model to SAMOSA data (black dots) for single look (top row) and multilooked waveforms (bottom row) for wave heights of 0.5, 2.0 and 6.0 m and 0° off-nadir roll angle. Note the poor fit of the analytic model to the 'toe' of the multilooked waveform when the SWH is low (0.5 m). (b) Comparison of the rise time from the best-fit analytic model to the SWH for the single- and multilooked waveforms. Except at low SWH, the rise time of the analytic model shows a good one-to-one relationship with the SWH. Meanwhile, the relationship for the multilooked waveform is not one-to-one suggesting that the analytic model accommodates the shape of the multilooked waveform by increasing the model rise time σ.

weighting functions as well as parameter reduction approaches (e.g., Sandwell & Smith, 2005). We have found that whether for LRM or SAR-mode data, subtle factors such as the number of 20 Hz waveforms that are assembled in a single least-squares fit or the amount of along-track smoothing of the SWH between the 3-parameter and 2-parameter retracking can have a significant effect on the along-track slope precision.

To assess the accuracy of the simple analytical model for estimating waveforms, we used our approach to retrack waveforms generated from the full-multilooked theoretical model including variations in SWH (0.58 m), and off-nadir roll angle (0.0° - 0.30°; Salvatore Dinardo 2012, personal communication, SAMOSA Project). The simulated waveform data was provided at a sampling of 1.5625 ns (or half the original tracking gate interval) to match the new L1b SAR format being provided by ESA in ground processor version 'B'. The first test involved retracking a single-looked (nadir Doppler beam only) SAMOSA waveform over the range of SWH and off-nadir roll angle shown in Fig. 2.B.1(a). When the off-nadir roll is 0°, the analytic model and SAMOSA model waveforms agree in shape to better than 1 part in 1000 at all gates for the full range of SWH. An exponential trailing edge decay function of the form $\exp(-\tau/\alpha)$ was used to improve the fit where the best-fit α was 0.0149 gate^{-1}. The arrival time estimated from the fit of the analytical model to the nadir-pointing SAMOSA data agreed to better than 1 mm in absolute range. The parameter from the least-squares model fit shows a good linear relationship with the SWH for the SAMOSA data with a misfit at smaller SWH due to the detailed shape of the point target response function not being fully characterized by our Gaussian analytic formulation. This comparison confirms that our model is a good description of the single-look, nadir-pointing case.

The least-squares fit of the analytic model to the multilooked (253 looks) SAMOSA waveform data show good visual fits for larger SWH but a poor fit at the base of the leading edge of the waveform (15 to 5 ns prior to epoch) for a very low SWH of 0.5 m. This feature is referred to as the toe of the waveform. Multilooking is essentially an incoherent sum of looks in all fore and aft directions in order to improve the signal-to-noise ratio of the 20 Hz waveforms (Wingham et al., 2004).

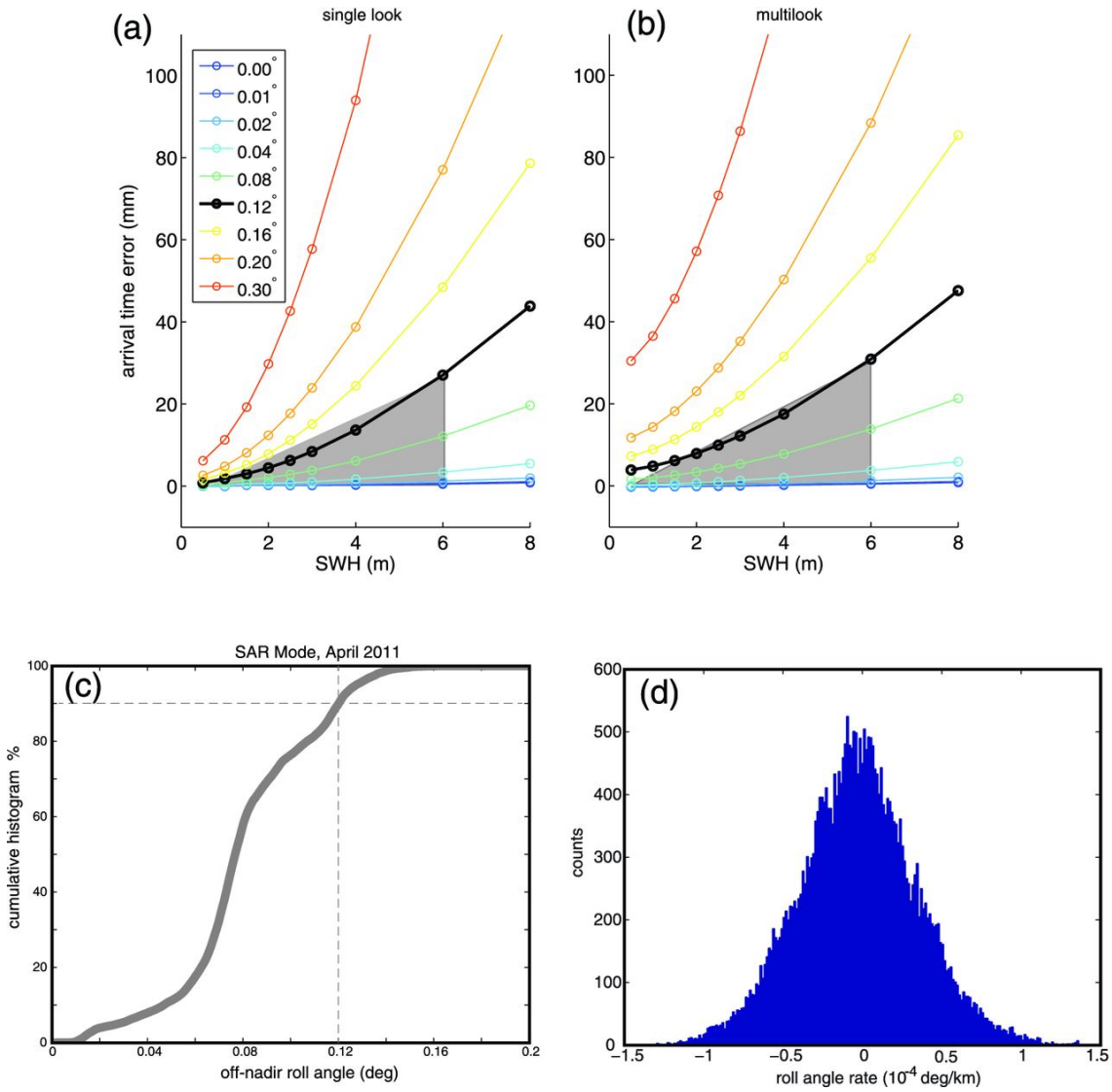

Figure 2.B.2: Error in arrival time for analytic model as a function of SWH for a range of off-nadir roll angles. Fits to both single- and multi-looked waveforms are shown. (c) Cumulative histogram of the absolute value of the off-nadir roll angle. A roll bias of 0.085° has been included Smith & Scharroo (2011). Grey shading shows the restricted parameter ranges to be used for gravity analysis. (d) Roll angle rate for a SAR pass across the Pacific.

Prior to summation, the off-nadir beams are shifted in range according to their extra path length compared to the nadir beam; this is the 'delay' compensation in 'delay-Dopper' altimetry (Raney, 1998). Multilook averaging causes an overall smoothing of the waveform. The broad off-nadir beams create the 'toe' at the leading edge that is not available in our approximate model. It should be noted that this multilook processing is designed for recovery of ice topography where multimeter surface roughnesses are common. Therefore, in the ice application the beneficial effects of a more robust waveform amplitude are more important than retaining the sharpest possible leading edge.

Although the multilook averaging has a significant effect on the entire shape of the waveform, it is nevertheless, still possible to adjust the parameters of our model to provide a good match. The question is how does this adjustment of the wrong-shaped analytic model affect the recovered parameters of arrival time and rise time? Remarkably, in the case of zero roll angle, the recovered arrival time agrees to better than 1 mm with the actual arrival time over the full range of SWH. However, the estimated rise time is overestimated with respect to the true SWH, especially when the SWH is low as shown in Fig. 2.B.1(b). Indeed, based on this analysis one could conclude that recovery of SWH less than 2 m will be challenging and perhaps impossible because the multilooking blurs the waveform in a way that is well approximated by convolution of a 2−m Gaussian wave height distribution. The conclusion is that the arrival time estimated by fitting our model to a multilooked waveform, having zero roll angle, is accurate to better then 1 mm. Of course when the actual noisy waveforms are modelled, the estimated arrival time parameter will be less accurate but this analysis suggests that there is not a significant range bias caused by applying our simple retracker to multilooked waveforms.

The more important issue is the arrival time error caused by a non-zero off-nadir roll angle. Again, we can use the simulated SAMOSA data to estimate the magnitude of this effect. The results of this analysis are shown in Fig. 2.B.2 where we plot the arrival time error from the fit of the analytic model as a function of SWH and off-nadir roll angle. We performed this analysis using both single look

(Fig. 2.B.2a) and multilooked (Fig. 2.B.2b) waveforms and the results are quite similar. When the off-nadir roll angle is less than 0.02°, the error is less than 7 mm. Following the approach of Smith & Scharroo (2011), we calculated the off-nadir roll angle from the spacecraft orientation data provided in the L1b product for the month of 2011 April. A constant 0.085° roll bias found by Smith & Scharroo (2011) was included in the analysis. A cumulative histogram of off-nadir roll shows that 90 percent of the data were acquired when the off-nadir roll angle is less than 0.12° (Fig. 2.B.2c). Our least-squares fits to the SAMOSA waveforms having off-nadir roll of 0.12° show misfits of 1 mm error at SWH of 1 m rising to 3.6 mm at an SWH of 2 m and in the most extreme case of SWH of 6 m, the error is 23 mm. Our objective for slope precision is 1 μrad. To determine the maximum slope error that could be caused by this range error associated with the roll angle we also calculated the roll rate for an example SAR pass across the Pacific. The maximum roll rate is 1.5×10^{-4} degrees per km along the satellite track. Based on the analysis of the range error of 23 mm caused by a change in roll angle of 0.12°, we calculate an upper bound on slope error of 0.029 μrad. This upper bound is 35 times smaller than our accuracy goal of 1 μrad so this error source is not important for construction of marine gravity. However, it is likely and possible to have a range error of 23 mm over the length of a few thousand kilometres. This magnitude of error is significant for construction of sea surface height models. So, we reiterate that our retracking approach, which does not account for mispointing error, is adequate for measuring sea surface slope but not height.

2.C Assessment of Slope Accuracy from Approximate SAR Retracker

Another approach to assessing the accuracy of along-track slopes derived from our SAR retracking is to compare our SIO/NOAA results with retracked SAR data provided by the CNES/CLS CryoSat Processing Prototype (CPP) (Labroue et al., 2012). We selected one descending track across the central Pacific and compared the height and slope of the ocean surface from the two groups. The 20-

Hz data records have exactly the same raw waveforms although there are differences in the corrections and orbits used by the two groups. Most significantly we did not apply the timing bias to the original ESA data used for our results while the CLS group did apply the correction. Therefore, the sea surface height (SSH) values along the ESA tracks were resampled and interpolated to the coordinates of the CPP ground tracks. A Gaussian filter with a width of 18 km was applied to all the sea surface height profiles. Then, the cumulative tide effect as predicted by the CSR 4.0 tide model was removed from the SIO heights. Finally, the sea surface slopes were computed using first differences. Both least-squares and 1-norm statistics were used to compare height and slope differences because the 20 Hz data still contain a few outliers.

The overall results confirm several aspects of the biases in our approximate SAR retracker as shown in Fig. 2.C.1. Figs 2.C.1(a) and (b) show the sea surface heights and height differences. The mean difference in height is more than 9 m. In addition, there is a change in height difference of $\sim$ 0.2 m along this $\sim$ 2000 km track. We attribute most or all of this error to our retracked product which has a $\sim$ 9 m error in absolute height and a significant change in along-track height error, perhaps due to the differences in tide models, other corrections, or timing bias. Such errors would be unacceptable for any application using sea surface height or sea level anomaly. However note that the $\sim$ 0.2 m error distributed over 2000 km amounts to a slope error of only $\sim$ 0.1 μrad, which is well below a significant error for gravity applications.

The magnitude of the slope error due to differences in data processing are shown in Figs 2.C.1(c)(e). The median difference in slope is -0.115 μrad (Fig. 2.C.1e) in accordance with the overall slope seen in the height difference plot (Fig. 2.C.1b). The standard deviation and median absolute deviation are around 2 μrad and 1.66 μrad, respectively. Figs 2.C.1b)(c) and (d) show that the slopes are in good agreement at length scales greater than about 50 km but have differences at smaller length scales due to differences in the retrackers. In addition to comparing the along track slope from the two groups, we also compared the along-track slope from each group with the corresponding slope from the CNES/CLS 2010 mean sea

surface (MSS) height model. The median absolute deviations for the CNES and SIO groups are 2.30 μrad and 2.64 μrad, respectively. The main conclusion is that the differences in slope between the CNES and SIO products are smaller than their individual differences from the best available MSS so these independent products have excellent agreement for along-track slope.

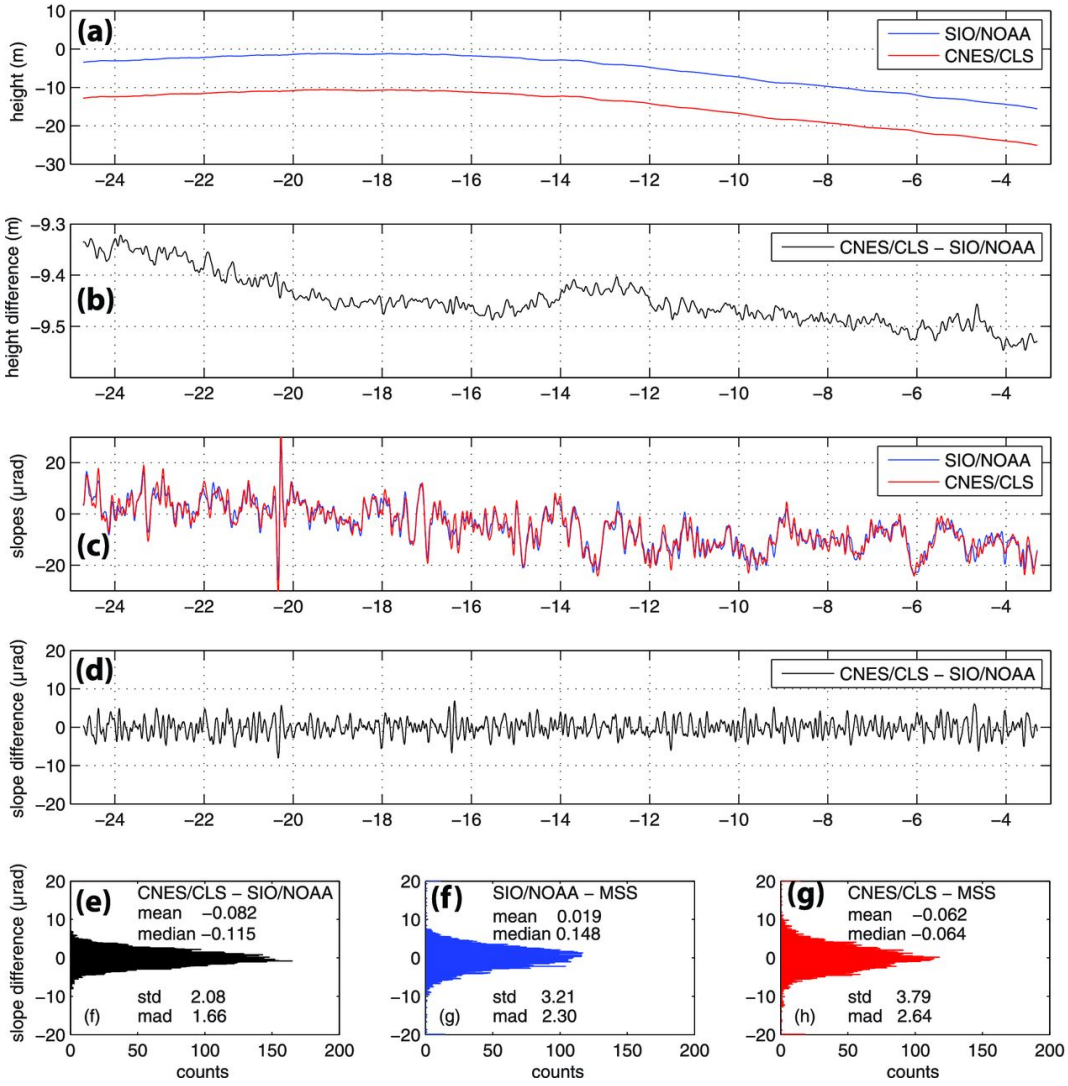

Figure 2.C.1: (a) Sea surface height in metres from the CNES/CLS (red) and SIO/NOAA (blue) retracking estimates, with the tide effect removed then filtered at 18 km. (b) Height differences have a $\sim$ 9 m bias and a $\sim$ 0.2 m height change along the 2000-km long pass. (c) Sea surface slope in microradian from the CNES/CLS (red) and SIO (blue) retracking estimates filtered at 18 km. (d) Slope differences have very small biases and trends. Histograms and statistics for differences between CNES and SIO (e), SIO and MSS (f) and CNES and MSS (g).

References

Abramowitz, M. & Stegun, I. A., 1964. *Handbook of mathematical functions: with formulas, graphs, and mathematical tables*, vol. 55, Courier Corporation.

Amarouche, L., Thibaut, P., Zanife, O., Dumont, J.-P., Vincent, P., & Steunou, N., 2004. Improving the jason-1 ground retracking to better account for attitude effects, *Marine Geodesy*, **27**(1-2), 171–197.

Andersen, O. B., Knudsen, P., & Berry, P. A., 2010. The dnsc08gra global marine gravity field from double retracked satellite altimetry, *Journal of Geodesy*, **84**(3), 191–199.

Bendat, J. S. & Piersol, A. G., 2011. *Random data: analysis and measurement procedures*, vol. 729, John Wiley & Sons.

Boy, F., Desjonquères, J.-D., Picot, N., Moreau, T., Labroue, S., Poisson, J., & Thibaut, P., 2012. Cryosat processing prototype: Lrm and sar processing on cnes side, in *Proceedings of the Ocean Surface Topography Science Team Meeting*.

Brown, G. S., 1977. The average impulse response of a rough surface and its applications, *Antennas and Propagation, IEEE Transactions on*, **25**(1), 67–74.

Chelton, D. B., Walsh, E. J., & MacArthur, J. L., 1989. Pulse compression and sea level tracking in satellite altimetry, *Journal of atmospheric and oceanic technology*, **6**(3), 407–438.

Chelton D.B., Ries J.C., H. B. F. L.-L. & P.S, C., 2001. Satellite altimetry, in *Satellite Altimetry and Earth Sciences*, chap. 1, pp. 1–131, eds L.-L., F. & Cazenave, A., Academic Press.

Cheney, R. E. & Coast, U., 1992. *The complete Geosat altimeter GDR handbook*, US Department of Commerce, National Oceanic and Atmospheric Administration, National Ocean Service, Coast and Geodetic Survey.

Childers, V. A., McAdoo, D. C., Brozena, J. M., & Laxon, S. W., 2001. New gravity data in the arctic ocean- comparison of airborne and ers gravity, *Journal of Geophysical Research*, **106**(5), 8871–8886.

Cotton, P., Andersen, O., Berry, P., Cipollini, P., Gommenginger, C., Martin-Puig, C., Stenseng, L., Benveniste, J., & Dinardo, S., 2010. The samosa project: assessing the potential improvements offered by sar altimetry over the open ocean, coastal waters, rivers and lakes, in *Proceedings of the ESA Living Planet Symposium*.

Dibarboure, G., Renaudie, C., Pujol, M.-I., Labroue, S., & Picot, N., 2012. A demonstration of the potential of cryosat-2 to contribute to mesoscale observation, *Advances in Space Research*, **50**(8), 1046–1061.

DLMF, 2010. Nist digital library of mathematical functions, http://dlmf.nist.gov/, Release 1.0.10 of 2015-08-07.

ESRIN, E. S. A. & University College London, M. S. S. L., 2013. *CryoSat Product Handbook*.

European Space Agency, 2013. *CryoSat Mission online resources*.

Ford, P. G. & Pettengill, G. H., 1992. Venus topography and kilometer-scale slopes, *Journal of Geophysical Research: Planets*, **97**(E8), 13103–13114.

Galin, N., Wingham, D. J., Cullen, R., Fornari, M., Smith, W. H., & Abdalla, S., 2013. Calibration of the cryosat-2 interferometer and measurement of across-track ocean slope, *Geoscience and Remote Sensing, IEEE Transactions on*, **51**(1), 57–72.

Giles, K., Wingham, D., Galin, N., Cullen, R., & Smith, W., 2012. Precise estimates of ocean surface parameters from cryosat, *Proc. Ocean Surf. Topogr. Sci. Team Meet*, pp. 1–13.

Gommenginger, C., Martin-Puig, C., Dinardo, S., Cotton, D., Srokosz, M., & Benveniste, J., 2011. Improved altimetric accuracy of sar altimeters over the

ocean: Observational evidence from cryosat-2 sar and jason-2, *Proc. OSTST Meet*, pp. 19–21.

Gommenginger, C., Cipollini, P., Cotton, D., Dinardo, S., & Benveniste, J., 2012. Finer, better, closer: Advanced capabilities of sar altimetry in the open ocean and the coastal zone, *Proc. Ocean Surf. Topogr. Sci. Team Meet*, pp. 1–24.

Gradshteyn, I. S. & Ryzhik, I., 2000. Table of integrals, series, and products. translated from the russian. translation edited and with a preface by alan jeffrey and daniel zwillinger.

Hayne, G. S., 1980. Radar altimeter mean return waveforms from near-normal-incidence ocean surface scattering, *Antennas and Propagation, IEEE Transactions on*, **28**(5), 687–692.

Jensen, J. R. & Raney, R. K., 1998. Delay/doppler radar altimeter: Better measurement precision, in *Geoscience and Remote Sensing Symposium Proceedings, 1998. IGARSS'98. 1998 IEEE International*, vol. 4, pp. 2011–2013, IEEE.

Labroue, S., Boy, F., Picot, N., Urvoy, M., & Ablain, M., 2012. First quality assessment of the cryosat-2 altimetric system over ocean, *Advances in Space Research*, **50**(8), 1030–1045.

Laxon, S. & McAdoo, D., 1994. Arctic ocean gravity field derived from ers-1 satellite altimetry, *Science*, **265**(5172), 621–624.

Louis, G., Lequentrec-Lalancette, M.-F., Royer, J.-Y., Rouxel, D., Géli, L., Maïa, M., & Faillot, M., 2010. Ocean gravity models from future satellite missions, *Eos, Transactions American Geophysical Union*, **91**(3), 21–22.

Marks, K. M. & Sailor, R. V., 1986. Comparison of geos-3 and seasat altimeter resolution capabilities, *Geophysical research letters*, **13**(7), 697–700.

Maus, S., Green, C. M., & Fairhead, J. D., 1998. Improved ocean-geoid resolution from retracked ers-1 satellite altimeter waveforms, *Geophysical Journal International*, **134**(1), 243–253.

Olgiati, A., Balmino, G., Sarrailh, M., & Green, C., 1995. Gravity anomalies from satellite altimetry: comparison between computation via geoid heights and via deflections of the vertical, *Bulletin géodésique*, **69**(4), 252–260.

Parker, R., 1973. The rapid calculation of potential anomalies, *Geophysical Journal International*, **31**(4), 447–455.

Pavlis, N. K., Holmes, S. A., Kenyon, S. C., & Factor, J. K., 2012. The development and evaluation of the earth gravitational model 2008 (egm2008), *Journal of geophysical research: solid earth*, **117**(B4).

Phalippou, L. & Enjolras, V., 2007. Re-tracking of sar altimeter ocean power-waveforms and related accuracies of the retrieved sea surface height, significant wave height and wind speed, in *Geoscience and Remote Sensing Symposium, 2007. IGARSS 2007. IEEE International*, pp. 3533–3536, IEEE.

Picot, N., Case, K., Desai, S., Vincent, P., & Bronner, E., 2012. *AVISO and PODAAC User Handbook. IGDR and GDR Jason Products, SALP-MU-M5-OP-13184-CN (AVISO), JPL D-21352 (PODAAC).*

Raney, R., Smith, W., Sandwell, D., Jensen, J., Porter, D., & Reynolds, E., 2003. Abyss-lite: Improved bathymetry from a dedicated small satellite delay-doppler radar altimeter, in *Geoscience and Remote Sensing Symposium, 2003. IGARSS'03. Proceedings. 2003 IEEE International*, vol. 2, pp. 1083–1085, IEEE.

Raney, R. K., 1998. The delay/doppler radar altimeter, *Geoscience and Remote Sensing, IEEE Transactions on*, **36**(5), 1578–1588.

Raney, R. K., 2012. Cryosat SAR-mode looks revisited, *Geoscience and Remote Sensing Letters, IEEE*, **9**(3), 393–397.

Rodríguez, E., 1988. Altimetry for non-gaussian oceans: Height biases and estimation of parameters, *Journal of Geophysical Research: Oceans*, **93**(C11), 14107–14120.

Rodriguez, E. & Martin, J. M., 1994. Assessment of the topex altimeter performance using waveform retracking, *Journal of Geophysical Research: Oceans*, **99**(C12), 24957–24969.

Sandwell, D. T., 1984. A detailed view of the south pacific geoid from satellite altimetry, *Journal of Geophysical Research: Solid Earth*, **89**(B2), 1089–1104.

Sandwell, D. T. & McAdoo, D. C., 1990. High-accuracy, high-resolution gravity profiles from 2 years of the geosat exact repeat mission, *Journal of Geophysical Research*, **95**(C3), 3049–3060.

Sandwell, D. T. & Smith, W. H., 2005. Retracking ers-1 altimeter waveforms for optimal gravity field recovery, *Geophysical Journal International*, **163**(1), 79–89.

Sandwell, D. T. & Smith, W. H., 2009. Global marine gravity from retracked geosat and ers-1 altimetry: Ridge segmentation versus spreading rate, *Journal of Geophysical Research: Solid Earth*, **114**(B1).

Smith, W., 2004. Introduction to this special issue on bathymetry from space, *Oceanography*, **17**(1), 6–8.

Smith, W. & Scharroo, R., 2011. Retracking range, swh, sigma-naught, and attitude in cryosat conventional ocean data, *Proc. OSTST Meet*, pp. 19–21.

Smith, W., Scharroo, R., Lillibridge, J., & Leuliette, E., 2011. Retracking cryosat waveforms for near-real-time ocean forecast products, platform attitude, and other applications, in *AGU Fall Meeting Abstracts*, vol. 1, p. 06.

Smith, W. H., 1998. Seafloor tectonic fabric from satellite altimetry 1, *Annual review of earth and planetary sciences*, **26**(1), 697–747.

Smith, W. H. & Sandwell, D. T., 1994. Bathymetric prediction from dense satellite altimetry and sparse shipboard bathymetry, *Journal of Geophysical Research: Solid Earth*, **99**(B11), 21803–21824.

Stenseng, L. & Andersen, O. B., 2012. Preliminary gravity recovery from cryosat-2 data in the baffin bay, *Advances in Space Research*, **50**(8), 1158–1163.

Stewart, R. H., 1985. *Methods of satellite oceanography*.

Thibaut, P., Poisson, J., Bronner, E., & Picot, N., 2010. Relative performance of the mle3 and mle4 retracking algorithms on jason-2 altimeter waveforms, *Marine Geodesy*, **33**(S1), 317–335.

Walsh, E. J., 1974. Analysis of experimental nrl radar altimeter data, *Radio Science*, **9**(8-9), 711–722.

Walsh, E. J., 1982. Pulse-to-pulse correlation in satellite radar altimeters, *Radio Science*, **17**(4), 786–800.

Walsh, E. J., Uliana, E., & Yaplee, B., 1978. Ocean wave heights measured by a high resolution pulse-limited radar altimeter, *Boundary-Layer Meteorology*, **13**(1-4), 263–276.

Wessel, P. & Chandler, M. T., 2011. The spatial and temporal distribution of marine geophysical surveys, *Acta Geophysica*, **59**(1), 55–71.

Wingham, D. & Wallis, D., 2010. The rough surface impulse response of a pulse-limited altimeter with an elliptical antenna pattern, *Antennas and Wireless Propagation Letters, IEEE*, **9**, 232–235.

Wingham, D., Francis, C., Baker, S., Bouzinac, C., Brockley, D., Cullen, R., de Chateau-Thierry, P., Laxon, S., Mallow, U., Mavrocordatos, C., et al., 2006. Cryosat: A mission to determine the fluctuations in earths land and marine ice fields, *Advances in Space Research*, **37**(4), 841–871.

Wingham, D. J., Phalippou, L., Mavrocordatos, C., & Wallis, D., 2004. The mean echo and echo cross product from a beamforming interferometric altimeter and their application to elevation measurement, *Geoscience and Remote Sensing, IEEE Transactions on*, **42**(10), 2305–2323.

Yale, M. M., Sandwell, D. T., & Smith, W. H., 1995. Comparison of along-track resolution of stacked geosat, ers 1, and topex satellite altimeters, *Journal of Geophysical Research: Solid Earth*, **100**(B8), 15117–15127.

Zhang, S. & Jin, J.-M., 1996. *Computation of special functions*, Wiley-Interscience.

Chapter 3

An Iterative Spectral Solution Method for Thin Elastic Plate Flexure with Variable Rigidity

Abstract

Thin plate flexure theory provides an accurate model for the response of the lithosphere to vertical loads on horizontal length scales ranging from tens to hundreds of kilometers. Examples include flexure at seamounts, fracture zones, sedimentary basins, and subduction zones. When applying this theory to real world situations, most studies assume a locally uniform plate thickness to enable simple Fourier transform solutions. However, in cases where the amplitude of the flexure is prominent, such as subduction zones, or there are rapid variations in seafloor age, such as fracture zones, these models are inadequate. Here we present a computationally efficient algorithm for solving the thin plate flexure equation for non-uniform plate thickness and arbitrary vertical load. The iterative scheme takes advantage of the 2-D Fast Fourier Transform to perform calculations in both the spatial and spectral domains, resulting in an accurate and computationally efficient solution. We illustrate the accuracy of the method through comparisons with known analytic solutions. Finally, we present results from three simple models

demonstrating the differences in trench outer rise flexure when 2-D variations in plate rigidity and applied bending moment are taken into account. Although we focus our analysis on ocean trench flexure, the method is applicable to other 2-D flexure problems having spatial rigidity variations such as seamount loading of a thermally eroded lithosphere or flexure across the continental-oceanic crust boundary.

3.1 Introduction

The oceanic lithosphere has an almost uniform composition and a well understood thermal evolution away from spreading ridges (Parsons & Sclater, 1977). Simple thermal evolution models, combined with isostasy and thin plate flexure theory, form the foundational methodology for understanding the gravity and topography of the deep oceans (Watts, 2001). Examples include flexure at seamounts (Kim & Wessel, 2010), spreading ridges (Luttrell & Sandwell, 2012), fracture zones (Sandwell & Schubert, 1982), continental margins (Erickson, 1993), and most importantly subduction zones (Watts & Talwani, 1974; Parsons & Molnar, 1976; Levitt & Sandwell, 1995; Bry & White, 2007). In most of these cases, the flexural modelling uses a uniform-thickness plate (or, in some instances, a plate with smooth thickness variations over wavelengths greater than the flexural wavelength) because it is theoretically simple, computationally fast, and usually provides an adequate description of the data if the results are interpreted in terms of an effective elastic thickness (Goetze & Evans, 1979; McNutt & Menard, 1982).

Over the past decade there have been dramatic improvements in the accuracy of the marine gravity field from satellite altimetry (Sandwell et al., 2013). In addition the multibeam coverage of the seafloor topography has expanded. Inverse spectral techniques have been used to estimate elastic thickness of the oceanic lithosphere by examining the admittance and coherence between gravity and topography measurements (Kirby, 2014). The spatial resolution of these estimates can be increased by using either wavelets (Kirby & Swain, 2011), multitapers (Perez-Gussinye et al., 2009), or a convolution method (Braitenberg et al., 2002).

However, variations in rigidity may occur over short spatial scales that are smaller than the typical flexural wavelength of a uniform rigidity plate. There is now an advanced understanding of the fracturing that occurs on the outer trench walls of subduction zones when the plates are bent beyond their elastic limits (e.g., Massell, 2002; Ranero et al., 2003). Therefore, realistic models, which account for spatial variations in rigidity arising from the combination of along-trench age gradients and inelastic yielding on the outer trench wall are needed to explain the improved seafloor data.

Most previous studies on trench flexure have adopted an elastic rheology and focused on reproducing profiles along one dimension perpendicular to the trench (Caldwell et al., 1976; Hanks, 1971; Watts & Talwani, 1974; Bodine & Watts, 1979; Levitt & Sandwell, 1995). However, in an attempt to explain the misfit in results for some trenches, other rheologies have been proposed for the oceanic lithosphere that account for perfectly plastic (Lobkovsky & Sorokhtin, 1976), elastic-perfectly plastic (Turcotte et al., 1978), viscoelastic (Melosh, 1978), or fully viscous behavior (de Bremaecker, 1977). One approach that allows plate rheology and failure condition to vary with depth is to construct a yield strength envelope (Goetze & Evans, 1979; McNutt & Menard, 1982). In this formulation, brittle failure in the upper, colder portion of the lithosphere together with ductile flow in the lower, hotter portion serve to constrain the thickness of an unyielded layer in the middle of the plate that behaves elastically. This effective elastic thickness T_e can be related to the flexural rigidity D of a thin plate, given a Young's modulus E and Poisson's ratio ν, through the relation

$$D(x,y) = \frac{ET_e^3(x,y)}{12(1-\nu^2)} \tag{3.1}$$

By letting the effective elastic thickness, or more generally the flexural rigidity, serve as a proxy for a more complete description of oceanic lithosphere rheology, we are able to adopt a thin elastic plate model for lithospheric flexure. In doing so, we can mathematically capture the gross behavior of a plate with varying and non-elastic rheology without having to specify an exact rheological structure. At well-studied outer rise regions, high-resolution multibeam

bathymetry data (Massell, 2002) , seismic refraction profiles (Ranero et al., 2003) and focal mechanism orientations (Craig et al., 2014) indicate pervasive extensional faulting. This increased yielding at the top of the plate decreases the plate's effective elastic thickness and hence flexural rigidity. As such, it is important to develop a computational model which includes variable rigidity in thin elastic plate flexure. In particular, two-dimensional variation is likely to be significant in some instances.

For example, elastic plates with variable rigidity in two dimensions were used to model the deformation of continental lithosphere in rifted basins (van Wees & Cloetingh, 1994) and foreland basins (Garcia-Castellanos, 2002). Flexure of the oceanic lithosphere at the trench outer rise has also been modeled using variable rigidity (Manriquez et al., 2014). These studies all noted the importance of including realistic variations in rigidity for successfully matching the observed topography (or bathymetry) with the output of their computational models. In the first two examples, the governing flexural equations were solved using finite difference techniques, while a finite element approach was taken in the last case. In this work, we present a method that solves the flexural equations by iteration in the spectral domain.

This iterative spectral method was originally developed in one dimension to model elastic flexure at oceanic fracture zones (Sandwell, 1984), and has been further extended to two-dimensional applications for other geophysical problems dealing with inhomogeneous elastic media (Barbot et al., 2008; Luttrell & Sandwell, 2012). Our method is able to obtain sufficiently accurate solutions for the deflection of a thin elastic plate with variable rigidity in two dimensions subject to arbitrary vertical loading and constant in-plane forces. When restrictions on the scale and amplitude of the variations in plate rigidity are followed, the iterative scheme converges rapidly. The high computational speed of our model is an advantage because it allows for finer grid spacing. Direct comparisons between model output and high-resolution data can be carried out without resorting to interpolation. Similarly, wider or more extensive searches for parameter values would then be possible for inverse problems.

In the following sections, we describe the mathematical framework of our computational scheme, and then report on its performance with respect to benchmark tests based on available analytic solutions. Finally, we demonstrate the potential utility of such a scheme by discussing some example cases of lithosphere flexure in a downgoing oceanic slab with varying rigidity due to an arcuate trench shape or to subduction of a plate of varying age subject to inelastic yielding.

3.2 Theory

Consider a thin elastic plate extending infinitely along two horizontal dimensions x and y. The plate's flexural rigidity $D(x, y)$ is in general a spatially varying function, and the plate is floating on an inviscid fluid substratum. The upward deflection of the plate surface $w(x, y)$ is the flexural response to the application of a vertical load distribution $p(x, y)$ and a constant in-plane force with components N_x, N_y, and N_{xy}. The values of these in-plane forces are taken to be positive when the plate is subject to tension, and negative when it is under compression. Furthermore, a restoring force is exerted by the material of the substratum. This force is proportional to the acceleration due to gravity g and the density contrast $\Delta\rho$ between the substratum and the material in-fill above the plate.

The partial differential equation describing the vertical flexural deflection w of the plate can then be written as:

$$\nabla^2 \left[D\nabla^2 w \right] - (1-\nu) \left[\frac{\partial^2 D}{\partial x^2}\frac{\partial^2 w}{\partial y^2} - 2\frac{\partial^2 D}{\partial x \partial y}\frac{\partial^2 w}{\partial x \partial y} + \frac{\partial^2 D}{\partial y^2}\frac{\partial^2 w}{\partial x^2} \right] - N_x \frac{\partial^2 w}{\partial x^2} - 2N_{xy}\frac{\partial^2 w}{\partial x \partial y} - N_y \frac{\partial^2 w}{\partial y^2} + \Delta\rho g w = p \qquad (3.2)$$

The boundary conditions are such that the deflection w vanishes at infinity,

$$\lim_{|x|,|y|\to\infty} w = 0 \qquad (3.3)$$

as should the slopes of the deflection along the corresponding dimensions:

$$\lim_{|x|\to\infty} \frac{\partial w}{\partial x} = 0, \quad \lim_{|y|\to\infty} \frac{\partial w}{\partial y} = 0 \tag{3.4}$$

When the rigidity D has a spatially uniform value D_0, the solution for 2-D flexure of a plate with uniform rigidity D_0 subjected to arbitrary vertical and in-plane loads may be written in the wavenumber domain of k_x and k_y (Banks et al., 1977; Wessel, 1996). Denoting the Fourier transform of the deflection $\mathcal{F}[w(x,y)]$ by $\hat{w}(k_x,k_y)$, the uniform plate solution can be written as

$$\hat{w_0}(k_x,k_y) = \hat{p}(k_x,k_y)\hat{\Phi}(k_x,k_y). \tag{3.5}$$

where we have defined a "uniform response function" $\hat{\Phi}(k_x,k_y)$:

$$\hat{\Phi}(k_x,k_y) = \left[(2\pi)^4 D_0 \left(k_x^2+k_y^2\right)^2 + (2\pi)^2 \left(N_x k_x^2 + 2N_{xy}k_x k_y + N_y k_y^2\right) + \Delta\rho g\right]^{-1} \tag{3.6}$$

The thin elastic plate formulation as expressed in (3.2) is valid when the rigidity $D(x,y)$ is slowly varying. To make this requirement explicit, the form of the rigidity must be such that it can be decomposed into a spatially uniform value D_0 and a spatially variable part $D'(x,y)$,

$$D(x,y) = D_0 + D'(x,y) \tag{3.7}$$

By using the decomposition in (3.7), we can rewrite (3.2) as an integral equation in the wavenumber domain,

$$\hat{w}(k_x,k_y) = p(k_x,k_y)\hat{\Phi}(k_x,k_y) - (2\pi)^4\Bigg\{\int_{-\infty}^{+\infty}\int_{-\infty}^{+\infty} ds_x\, ds_y\, \hat{D}'(k_x-s_x,k_y-s_y)\hat{w}(s_x,s_y) \times \Bigg\{(k_x^2+k_y^2)(s_x^2+s_y^2) - (1-\nu)\left[(k_x-s_x)^2 s_y^2 - 2(k_x-s_x)(k_y-s_y)s_x s_y + (k_y-s_y)^2 s_x^2\right]\Bigg\}\Bigg\} \tag{3.8}$$

We show in Appendix 3.A that (3.8) is in the form of a two-dimensional Fredholm integral equation of the second kind, and may be solved through an iterative process as described in Appendix 3.B. Our iterative solution to this problem for arbitrary, square-integrable rigidity D and load distribution p is developed using Fourier transforms in the wavenumber domain, but some calculations are performed in the space domain to improve accuracy and execution time. The iteration that is implemented in our computer algorithm is

$$\hat{w}^{(n)}(k_x,k_y) = \hat{w}_0(k_x,k_y) - \hat{\Phi}(k_x,k_y)\mathcal{F}\Bigg\{\nabla^2\left[D'\nabla^2 w^{(n-1)}\right] - (1-\nu)\left[\frac{\partial^2 D'}{\partial x^2}\frac{\partial^2 w}{\partial y^2}^{(n-1)} - 2\frac{\partial^2 D'}{\partial x\partial y}\frac{\partial^2 w}{\partial x\partial y}^{(n-1)} + \frac{\partial^2 D'}{\partial y^2}\frac{\partial^2 w}{\partial x^2}^{(n-1)}\right]\Bigg\} \tag{3.9}$$

An updated solution $\hat{w}^{(n)}$ in the wavenumber domain is equal to the uniform plate solution $\hat{w}_0$ that is corrected by a small perturbation related to the spatial derivatives of the varying part of the rigidity D' , as well as the spatial derivatives of the previous solution $w^{(n-1)}$. The iteration is allowed to continue until the root mean square differences between successive solution estimates w_n and w_{n-1} drop below a specified tolerance value. The boundary conditions (3.3) and (3.4) are enforced by setting the mean value of plate deflection to zero which corresponds to setting the zero wavenumber component to zero. In addition, the applied load distribution p must have zero mean.

While the differential equation and boundary conditions could be solved in the space domain using a finite difference or finite element approach, the Fourier analysis is helpful in four areas. 1) The Fourier approach provides an optimal initial guess as the well-known solution to flexure of a uniform rigidity plate under an arbitrary load (Banks et al., 1977; Wessel, 1996). 2) For periodic band-limited functions $D'(x, y)$ and $w(x, y)$, the most accurate estimates of the derivatives with respect to x and y are performed by wavenumber multiplication in the Fourier domain (Trefethen, 2000). One could design an optimal finite difference operation in the space domain to perform the derivative, but as shown in (Trefethen, 2000), the length of that space domain operator is equal to the length of the w or D' arrays. The most accurate and efficient way to perform this differentiation is by taking the discrete Fourier transform of each array, multiplying by the appropriate wavenumbers, and then inverse transforming the result. The three terms involving spatial derivatives of the D' array need to be evaluated only once while the three spatial derivatives of the w array need to be evaluated at each iteration. 3) By iterating in the Fourier domain, the band-limited requirement for convergence can be enforced by suppressing numerical instabilities that can occur at the shortest wavelengths. 4) Finally, the conditions for convergence of the iterative scheme are best exposed in the Fourier domain as shown in Appendix 3.C.

3.3 Benchmarks

We tested the accuracy of the iterative algorithm given in equation (3.9) through comparisons with analytic, closed-form solutions to thin plate flexure problems. As there is a paucity of such solutions in two dimensions which involve variable rigidity, we drew most benchmark cases from textbook examples of one-dimensional solutions (Turcotte & Schubert, 2002; Hetenyi, 1946). The numerical algorithm was coded in FORTRAN and utilizes a multidimensional FFT routine written by Brenner (Brenner, 1967). The inputs to the program are grids of plate rigidity $D(x, y)$ and the load distribution $p(x, y)$. The program calculates grids of plate deflection, plate curvature, and gravity anomaly as output. Typical grid sizes

are 2048 by 2048 pixels and grid spacing is about one hundredth of the flexural wavelength so most cases had grid sizes of 20 flexural wavelengths across both grid dimensions. Such spatially large grids are needed to ensure that the numerical solutions approach zero at the boundaries.

The benchmark results, (a) through (g), are summarized in Figure 3.1. The first column of the figure provides a short description of the benchmark as well as the equation in this section for the analytic formula. The second column shows the loading configurations of benchmarks in diagrams. Note all these cases are 1-D benchmarks except for (f). Also note that only benchmarks (b) and (g) have variable rigidity. The third column shows profiles of plate deflection taken across each model where the horizontal scale is normalized by the appropriate flexural parameter. At this vertical scale the profiles from the numerical models and analytic solutions cannot be distinguished. The last column shows the difference between the numerical and analytic solutions, which range from about 1% to 10% depending on the benchmark.

(a) Line load, uniform D

The first benchmark is a line load on a plate with uniform rigidity D_0 (Figure 3.1a). The load distribution has the form $p(x, y) = V_0\delta(x)$, where V_0 is the amplitude of the vertical load. The upward deflection $w(x)$ then has the expression (Turcotte & Schubert, 2002; Hetenyi, 1946):

$$w = -w_l \exp\left(-\frac{|x|}{\alpha}\right)\left[\cos\left(\frac{x}{\alpha}\right) + \sin\left(\frac{|x|}{\alpha}\right)\right] \tag{3.10}$$

where the amplitude is $w_l = V_0\alpha^3/8D_0$ and the flexural parameter α is given by

$$\alpha = \left[\frac{4D_0}{\Delta\rho g}\right]^{1/4} \tag{3.11}$$

In this case as well as the other tests that followed, we assumed a density contrast $\Delta\rho$ that is appropriate for the oceanic lithosphere, where the substrate has a density similar to that of the uppermost mantle and the in-fill above the plate has the density of seawater.

Benchmark Case	Schematic of Load Configuration	Algorithm Output	Algorithm Error
(a) line load uniform D *analytic solution: eq. (10)*	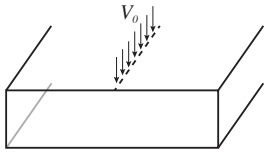	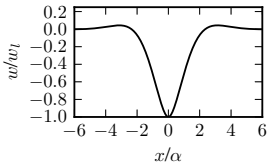	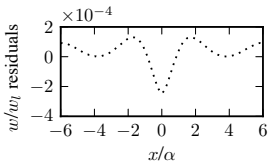
(b) line load variable D (line crack) *analytic solution: eq. (12)*	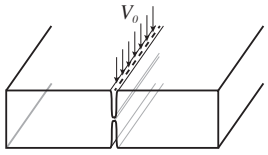	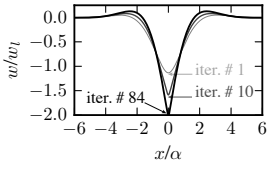	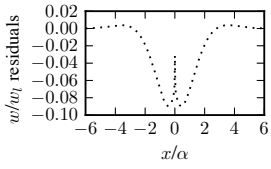
(c) line load in-plane load (compression) uniform D *analytic solution: eq. (13)*	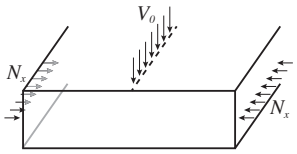	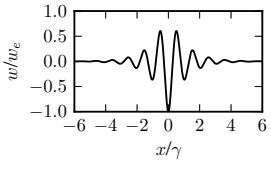	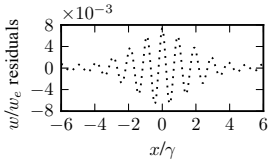
(d) line moment uniform D *analytic solution: eq. (17)*	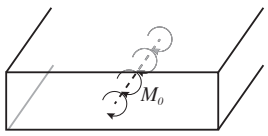	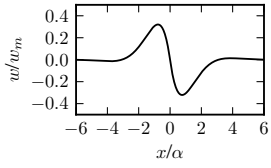	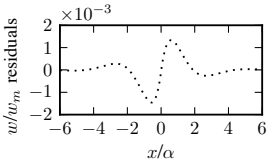
(e) line moment in-plane load (compression) uniform D *analytic solution: eq. (18)*	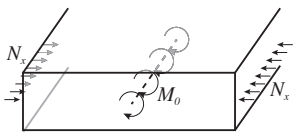	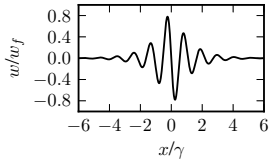	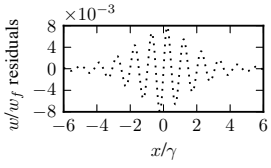
(f) concentrated moment uniform D *analytic solution: eq. (19)*	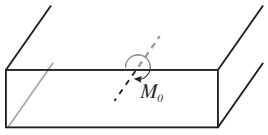	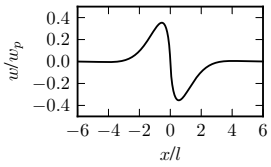	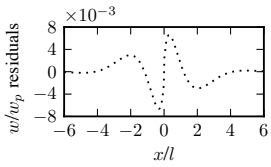
(g) line moment variable D (sharp contrast) *analytic solution: eqs. (22)-(23)*	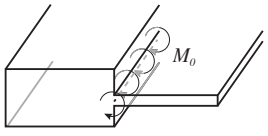	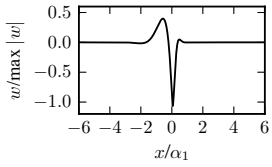	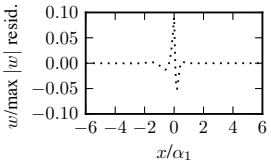

Figure 3.1: Summary of benchmark tests.

We use our numerical approach to simulate this simple case. The difference between the analytic and numerical solutions are everywhere smaller than 1%. The difference is caused by the finite length of the numerical model and could be improved by increasing the x-dimension of the model.

(b) Line load, variable D (line crack)

The second benchmark is a line load on a cracked plate (Figure 3.1b). The analytic solution is (Turcotte & Schubert, 2002; Watts, 2001)

$$w = -2w_l \exp\left(-\frac{|x|}{\alpha}\right) \cos\left(\frac{x}{\alpha}\right) \tag{3.12}$$

where w_l and α have the same values as in (3.10). We model this broken plate as a sharp reduction in rigidity at the origin. In practice, the code will not converge if the rigidity contrast between the plate and the hole is greater than about 1000, corresponding to a reduction in elastic thickness by an order of magnitude. In addition the shape of the rigidity reduction was modeled using a Gaussian function with a half width of 20 pixels while the load was 1 pixel wide. This finite width of the rigidity hole corresponds to smoothing the rigidity to enable convergence as discussed in Appendix 3.C while still permitting variation over wavelengths considerablt shorter than the flexural wavelngth. The path to convergence is shown in Figure 3.1b. The first iteration provides a good fit to the uniform rigidity plate flexure solution. After 10 iterations the fit at the origin improves and by 84 iterations the solution has converged. The model error plot shows some large differences of up to 10% between the converged numerical solution and the analytic solution (3.12). These are primarily due to the need to have a finite width flexural rigidity hole, which moves the region of maximum flexure by about 5 pixels away from the origin. This misfit illustrates the band-limited nature of this numerical modelling approach and demonstrates the error introduced when this smoothness constraint is not met.

(c) Line load, in-plane compression, uniform D

The third benchmark is a line load on a uniform rigidity plate (Figure 3.1c). An additional constant compressional in-plane force N_x is applied along the x-direction. The analytic solution is (Hetenyi, 1946):

$$w = -w_e \exp\left(-\frac{|x|}{\beta}\right)\left[\beta\cos\left(\frac{x}{\gamma}\right) + \gamma\sin\left(\frac{|x|}{\gamma}\right)\right] \tag{3.13}$$

where $w_e = V_0/2\alpha^2\Delta\rho g$ with α as in (3.11) and the other flexural parameters β and γ have the expressions

$$\beta = \left[\left(\frac{\Delta\rho g}{4D_0}\right)^{1/2} + \left(\frac{N_x}{4D_0}\right)\right]^{-1/2} \tag{3.14}$$

$$\gamma = \left[\left(\frac{\Delta\rho g}{4D_0}\right)^{1/2} - \left(\frac{N_x}{4D_0}\right)\right]^{-1/2} \tag{3.15}$$

From the form of β and γ, we can identify the critical buckling load N_c as

$$N_c = 2\left(\Delta\rho g D_0\right)^{1/2} \tag{3.16}$$

We tested both extensional and compressional regimes for our benchmarks, but here we show only one case in which the magnitude of the compressional in-plane force is $0.95N_c$ (Figure 3.1c). The numerical model differs from the analytic formula by less than 1% even when the loading conditions are close to inducing plate buckling.

(d) Line moment, uniform D

The fourth benchmark is a line moment on a uniform rigidity plate (Figure 3.1d). The deflection w may be found by approximating the applied moment as a couple of equal and opposing vertical loads (Hetenyi, 1946; Watts, 2001). We illustrate the assumptions and implications of this approximation in Appendix 3.D. Adapting the 1-D solution arising from this approximation for the case of a line moment applied along the y-direction on a plate leads to the expression

$$w = -w_m \exp\left(-\frac{|x|}{\alpha}\right) \sin\left(\frac{x}{\alpha}\right) \tag{3.17}$$

where $w_m = M_0\alpha^2/4D_0$. The numerical model differs from the analytic formula by less than 1% for this case.

(e) Line moment, in-plane compression, uniform D

The fifth benchmark is a line moment on a uniform rigidity plate including an in-plane force (Figure 3.1e). The deflection may be obtained as (Hetenyi, 1946),

$$w = -w_f \exp\left(-\frac{|x|}{\beta}\right) \sin\left(\frac{x}{\gamma}\right) \tag{3.18}$$

where in this case $w_f = M_0\beta\gamma/4D_0$ and the same expressions for β and γ as in (3.14) and (3.15) are used. As with the previous example, the numerical model differs from the analytic formula by less than 1%.

(f) Concentrated moment, uniform D

The sixth benchmark is a concentrated moment applied to a uniform rigidity plate (Figure 3.1f). The moment is oriented along the x-direction and is applied at the origin. The deflection due to this concentrated moment is given by:

$$w = w_q \left[\frac{x}{2^{1/2} l \left(x^2+y^2\right)^{1/2}}\right] \left\{ \mathrm{Kei}_1 \left[\frac{\left(x^2+y^2\right)^{1/2}}{l}\right] - \mathrm{Ker}_1 \left[\frac{\left(x^2+y^2\right)^{1/2}}{l}\right] \right\} \tag{3.19}$$

where we are using Kelvin-Bessel functions Ker and Kei of order 1, and $w_q = M_0 l^2/2\pi D_0$. The flexural parameter l has the form,

$$l = \left[\frac{D_0}{\Delta\rho g}\right]^{1/4} \tag{3.20}$$

The numerical model differs from the analytic formula by less than 1% for this case as well.

(g) Line moment, variable D (sharp contrast)

The final benchmark is a line moment applied to a plate with a stepwise change in rigidity (Figure 3.1g). The rigidity has a variation described by

$$D(x) = \begin{cases} D_1 & : x < 0 \\ D_2 & : x > 0 \end{cases} \tag{3.21}$$

and a line moment is applied along the boundary at $x = 0$ between the two regions of the plate. As derived in Appendix 3.E, the formulas for the deflection w_1 and w_2 in each region are

$$w_1 = \exp\left(\frac{x}{\alpha_1}\right)\left[A_1 \cos\left(\frac{x}{\alpha_1}\right) + B_1 \sin\left(\frac{x}{\alpha_1}\right)\right] \quad : x < 0 \tag{3.22}$$

$$w_2 = \exp\left(-\frac{x}{\alpha_2}\right)\left[A_2 \cos\left(\frac{x}{\alpha_2}\right) + B_1 \sin\left(\frac{x}{\alpha_2}\right)\right] \quad : x > 0 \tag{3.23}$$

where α_1 and α_2 are the flexural parameters for the plate regions on each side of the boundary. The values for the coefficients A_1, A_2, B_1, and B_2 are given in Appendix 3.E. The deflection computed by the iterative spectral method agrees to within 10% with the analytic solutions for a rigidity contrast of a factor of 1000 (corresponding to a T_e contrast of ∼10 times).

3.4 Discussion

3.4.1 Example 2-D models

In the previous section we evaluated the accuracy of the iterative spectral method through comparisons with analytic solutions, under a variety of the loading and rigidity configurations. We also examined the validity of the vertical load couple approximation to the effect of an applied moment in the plate interior. This new modelling approach is particularly appropriate for simulating plate flexure outboard of deep ocean trenches. The most general case of trench flexure has a plate of variable age, and thus variable flexural rigidity, being subducted along a trench that has an arcuate planform. The first two models presented in this

study illustrate the importance of these two effects as well as the robustness of our solution algorithm by deliberately exaggerating the rigidity contrast and rigidity contrast. The computer algorithm can accommodate both effects simultaneously but we separate the effects to isolate their relative importance, then show their combined effects in the third and last model.

The first case illustrates the importance of an arcuate trench planform on trench depth and outer rise height. The model trench has a sinusoidal planform as shown in Figure 3.2, representing an extreme case of an arcuate trench. A uniform bending moment of 1.0×10^{15} N was applied along the trench by constructing a 2-D force grid containing mostly zeros but having force couples that are approximated by the derivative of a Gaussian function, effectively producing a force couple with a finite width of one pixel. The plate on the left side of the trench was assigned a uniform flexural rigidity of 1.0×10^{23} Nm while the plate on the right side was assigned a rigidity 1000 times smaller, corresponding to a T_e of $\sim$ 25 km and $\sim$ 2.5 km respectively. In an actual subduction zone, the subducted plate ends somewhere deep in the mantle. Our solution method is designed only for continuous plates where the deformation goes to zero at the edges of the model. To simulate the plate having an end in the mantle we dramatically weaken the subducted plate so its finite strength does not have a dominant effect on the flexure outboard of the trench. The sinusoidal model with variable rigidity, was embedded in a larger 2048 by 2048 grid with a pixel spacing of 1.85 km. The larger grid has a uniform rigidity around the perimeter of the smaller subgrid. Convergence to an accuracy of better than 0.004 was achieved after 60 iterations in 130 seconds of CPU time on a personal computer.

The results (Figure 3.2) illustrate the importance of accomodating a realistic trench planform as well as the ability to dramatically lower the flexural rigidity of the "subducted" plate. Figure 3.2 shows a contour plot of the plate deflection. Similarly as in (Tanimoto, 1998), the physical interpretation of the "outboard" deflection should be restricted to regions where the deflection curve is concave downward, which for Figure 3.2b is to the right of 25 km for profile 1 and 50 km for profile 2. There, the flexure has a broader response than the flexure on the

right side of the trench. This is due to the 1000 times difference in flexural rigidity. By simulating a broken end of the subducted plate in the mantle in this way, the numerical values of the applied loads lose absolute physical meaning, but the deflection and curvature of the trench and outer rise are accurately preserved. Two profiles taken across the most concave (profile 1) and convex (profile 2) planforms of the trench illustrate the impact of trench curvature on both the amplitude and wavelength of the flexure. Profile 1 has an outer rise that is 1.5 times taller than profile 2 and the distance to the first zero crossing outboard of the outer rises is significantly different. If one modeled these two flexure profiles using the standard 1-D approach the estimates of bending moment and flexural rigidity for profile 1 would be too large while the same estimates for profile 2 would be too small. When modelling real seafloor topography data, the position of the trench and outer rise will depend on the location of the applied bending moment. The benchmarks provided above show that the location of the first zero crossing point seaward of the trench axis can be adjusted by changing the ratio of the downward load V_0 and the bending moment M_0 (Turcotte & Schubert, 2002).

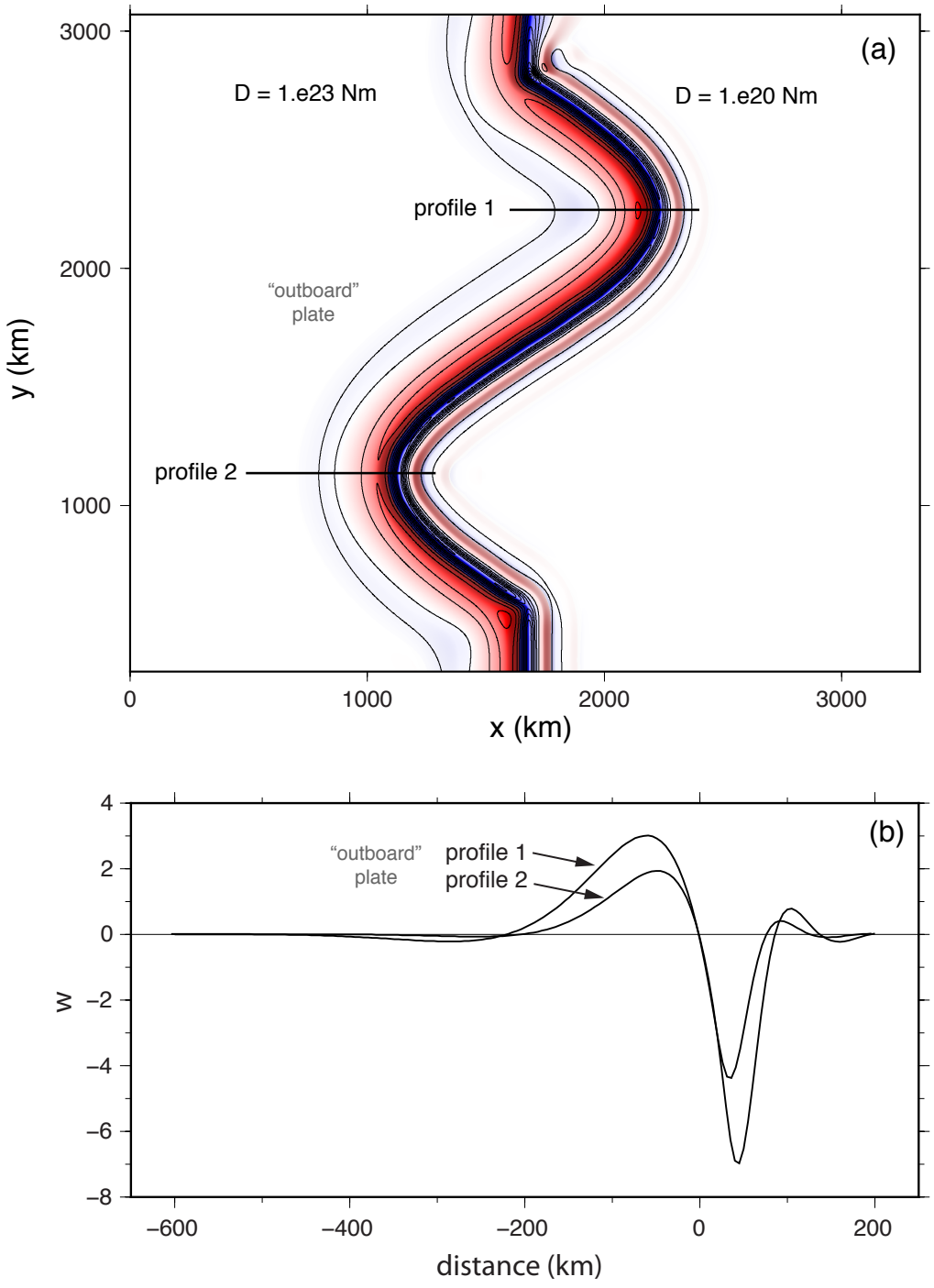
(a)
D = 1.e23 Nm
D = 1.e20 Nm
profile 1
profile 2
"outboard" plate
y (km)
x (km)
3000
2000
1000
0
1000
2000
3000
(b)
"outboard" plate
profile 1
profile 2
w
distance (km)
4
2
0
−2
−4
−6
−8
−600
−400
−200
0
200

Figure 3.2 *(previous page)*: (a) Plate deflection due to a uniform bending moment applied to a trench having a sinusoidal planform. The flexural rigidity of the plate to the right of the trench is 1000 times less than the flexural rigidity on the left side of the trench resulting in an asymmetry across the trench. Red color indicates deflection upwards while blue color indicates deflection downwards. Contours of deformation shown every 1 m. (b) Profiles across the most concave and convex parts of the trench illustrate the effects of curvature on the amplitude and wavelength of the flexure.

The second case illustrates the ability and importance of varying the flexural rigidity along the strike of the trench. When modelling actual trenches, the rigidity outboard of the trench will vary according to the rigidity expected for the actual age of the plate. In this model, the flexural rigidity varies smoothly over a range appropriate for oceanic lithosphere (T_e of 5 km to 25 km) as shown in Figure 3.3. This corresponds to an along-strike variation in rigidity of 125 times. Elastic thicknesses and flexural rigidity are provided along 6 sample profiles in Figure 3.3. As in the previous case a uniform bending moment of 1.0×10^{15} N was applied along the trench by constructing a 2-D force grid and utilizing the derivative of a Gaussian to assign forces to pixels. The results show a reduction in flexural amplitude and an increase in flexural wavelength as the flexural rigidity is increased from the bottom to the top of the plate, as is expected in a plate with gradually varying rigidity.

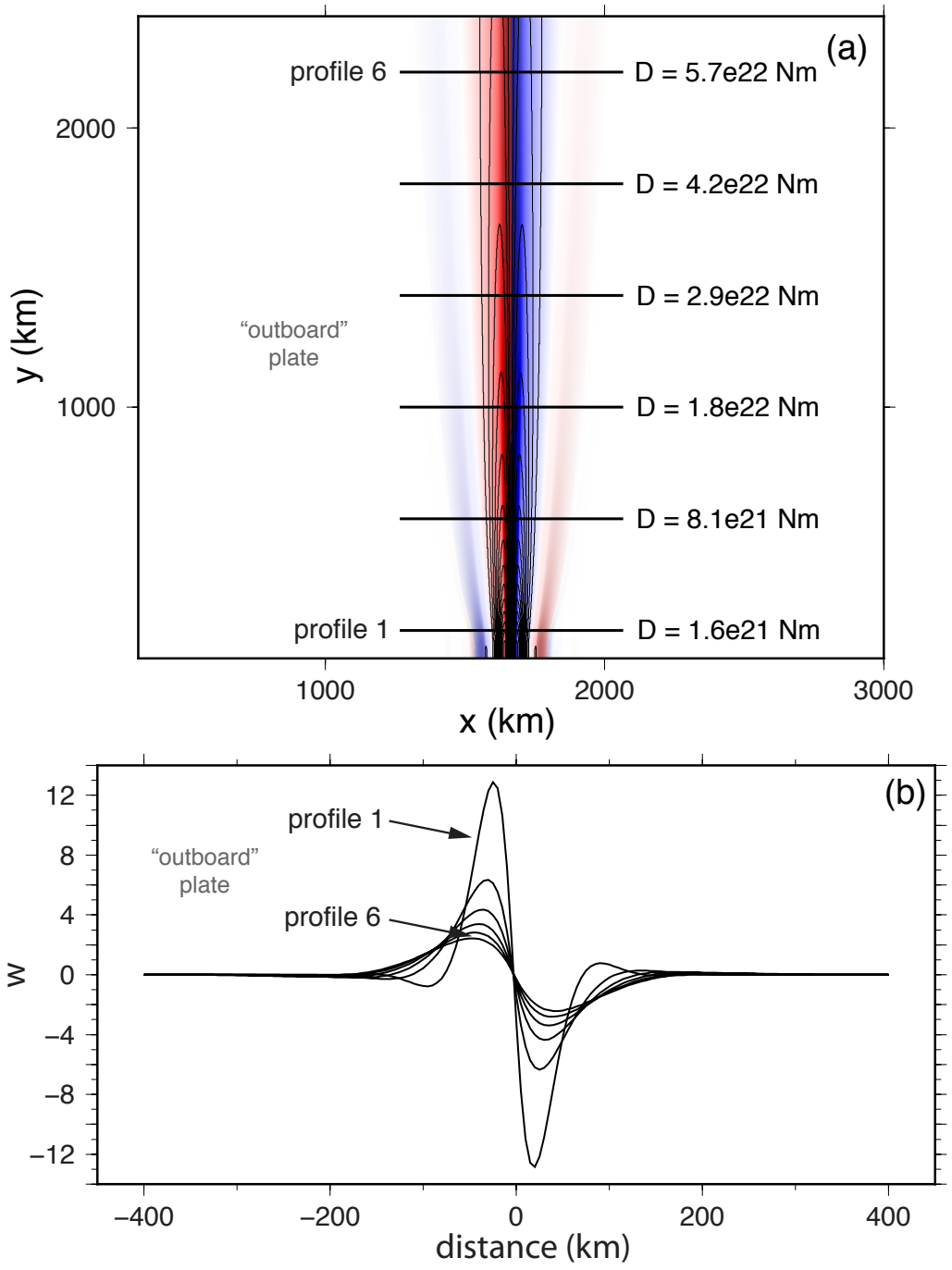
(a)
profile 6
D = 5.7e22 Nm
D = 4.2e22 Nm
D = 2.9e22 Nm
D = 1.8e22 Nm
D = 8.1e21 Nm
profile 1
D = 1.6e21 Nm
"outboard" plate
2000
1000
y (km)
1000
2000
3000
x (km)
(b)
profile 1
profile 6
"outboard" plate
12
8
4
0
−4
−8
−12
w
−400
−200
0
200
400
distance (km)

Figure 3.3 *(previous page)*: Plate deflection due to a uniform line moment applied to a plate of spatially variable rigidity. (a) The rigidity variations from the bottom to the top of the plate correspond to elastic thickness variations appropriate for oceanic lithosphere (5 - 25 km). Red color indicates deflection upwards while blue color indicates deflection downwards. Contours of deformation shown every 1 m. (b) Six profiles extracted from the plate deflection model illustrate the changes in amplitude and flexural wavelength due to along-strike variations in rigidity.

The third and final case we present is a toy model of the expected plate deflection along a portion of the South America trench offshore Chile (Figure 3.4a), using the actual trench geometry but synthetic estimates of the rigidity and loading properties. We caution the reader that is outside of the scope of the present study to obtain rigorous estimates for these parameters that agree well with observations. For this toy model, the vertical loads and moments were applied along a digitized planform of the trench that was divided into 25-km long segments. The magnitudes for this load distribution were chosen arbitrarily in order to reasonably simulate variations in loading along the Chile trench (Bry & White, 2007; Contreras-Reyes & Osses, 2010). The rigidity variations (shown in Figure 3.4e and f) outboard of the trench reflect a reasonable estimate of variations due to lithosphere age and plate weakening due to yielding, while the rigidity inboard of the trench was set to a constant value which is an order of magnitude lower. Note that the rigidity values assumed here will differ from those corresponding to previous estimates of effective elastic thickness for the outer rise at this particular region (Bry & White, 2007; Contreras-Reyes & Osses, 2010), in part due to the choice of thermal parameters. However, what we seek to demonstrate here is the significance of relative variations in rigidity. When lithospheric yielding is taken into account in our model, the plate can be as much as ten times weaker at the trench than otherwise. This in turn results in significant curvature of the model deflection at the outer rise that is not captured when plate rigidity varies only with age without any imposed weakening (Figure 3.4b and d). While the depth at the

trench is about the same for both test cases, the outer rise is more prominent for the case that allows yielding. This model, though using synthetic rigidity and loading parameters, demonstrates the potential utility of our iterative solution to future studies involving flexural modelling, particularly those concerned with the curvature of the outer rise in subducting oceanic plates.

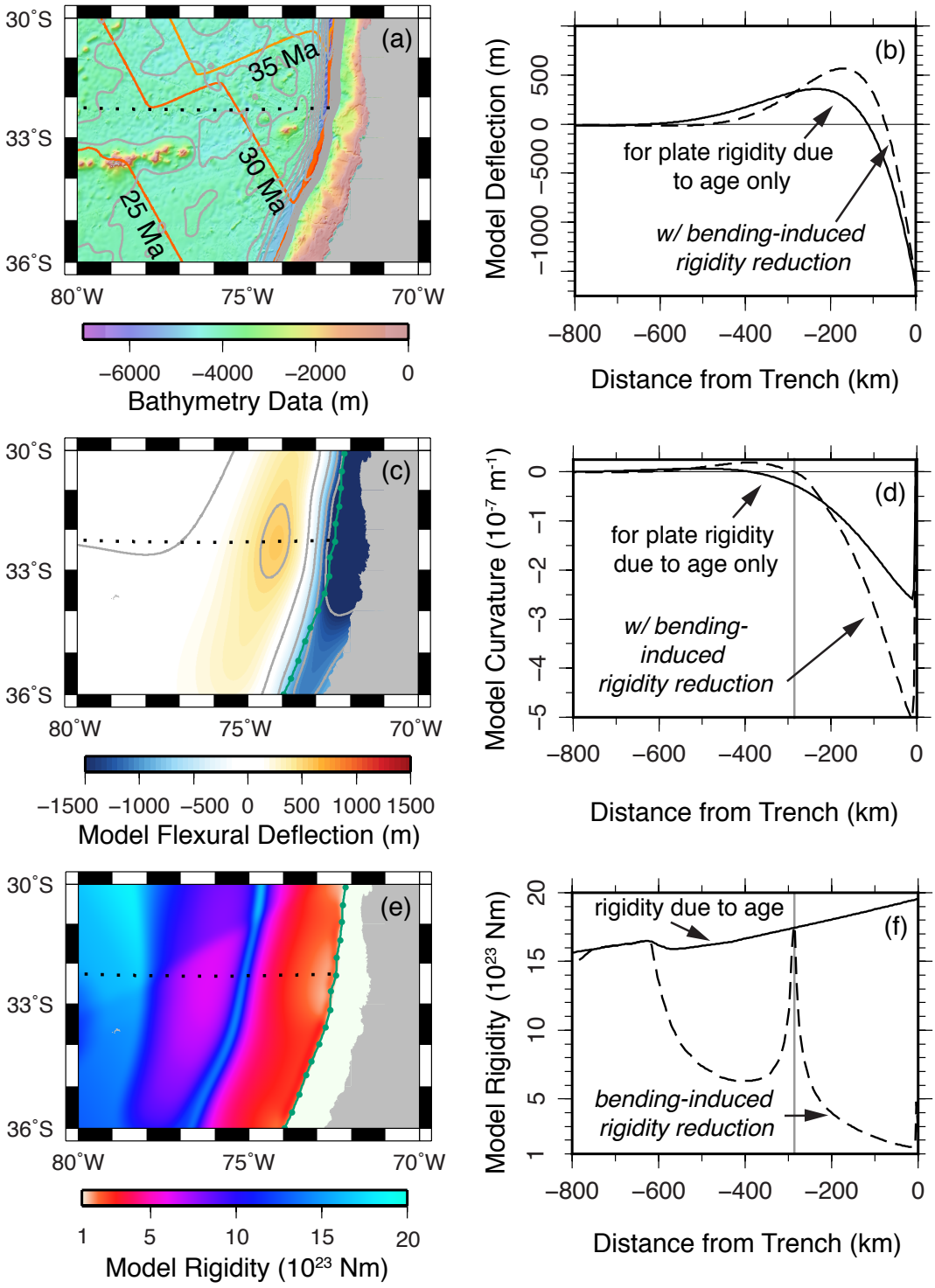
30°S
33°S
36°S
80°W
75°W
70°W
(a)
35 Ma
30 Ma
25 Ma
−6000 −4000 −2000 0
Bathymetry Data (m)
(b)
Model Deflection (m)
500 0 −500 −1000
−800 −600 −400 −200 0
for plate rigidity due to age only
w/ bending-induced rigidity reduction
Distance from Trench (km)
(c)
−1500 −1000 −500 0 500 1000 1500
Model Flexural Deflection (m)
(d)
Model Curvature (10⁻⁷ m⁻¹)
0 −1 −2 −3 −4 −5
for plate rigidity due to age only
w/ bending-induced rigidity reduction
Distance from Trench (km)
(e)
1 5 10 15 20
Model Rigidity (10²³ Nm)
(f)
Model Rigidity (10²³ Nm)
1 5 10 15 20
rigidity due to age
bending-induced rigidity reduction
Distance from Trench (km)

Figure 3.4 *(previous page)*: Plate deflection due to a varying moment and vertical load applied to a plate of spatially variable rigidity based on plate age and lithospheric yield strength envelopes. (a) Map of high-resolution multibeam and predicted bathymetry (Smith & Sandwell, 1997) with contours every 500 m from depths of 4 to 6 km. Contours of seafloor age (Müller et al., 2008) every 5 Ma are also shown. (b) Profiles of flexural deflection are compared for the cases when the plate rigidity is only based on age, and when weakening from increased curvature due to bending occurs. The location of the profile is shown as a dotted track in the maps along the left panel. (c) Model results for flexural deflection, with contours every 500 m. The moment and vertical loads were applied along the trench planform outlined in dark green. (d) Profiles of the deflection curvature (second spatial derivative). (e) The rigidity grid used to compute the final deflection solution displays some weakening towards the trench, with cooler colors representing a stronger plate and warmer colors corresponding to a weaker plate. The transition from cool to warm colors occurs around the mean value of the rigidity for this grid, which is around 5×10^{23} N $\cdot$ m^2. (f) Rigidity values along the profile are compared. The sharp spike upwards in rigidity around 300 km away from the trench corresponds to a change in the sign of the curvature.

3.4.2 Some practical considerations

In all of the test cases and benchmark models described above, the load and rigidity are embedded in a grid having dimensions of a power of 2. In actuality, any grid having dimensions that can be factored into small prime numbers is nearly optimal for the FFT algorithm (Brenner, 1967). One minor issue occurs at the boundaries of the model when there are sharp variations in rigidity. The Fourier analysis assumes all the functions repeat cyclically over the length and height of the grid. The rate of convergence of the iteration method depends on both the magnitude and rate of variation of the flexural rigidity grid. To improve convergence rate, the part of the rigidity grid that is external to the model area is smoothly tapered to a constant background value. Hence the rigidity along the

perimeter of the total grid becomes set to a constant value as well. In addition the rigidity grid is low-pass filtered in the wavenumber domain using a Gaussian function to reduce the amplitudes of the transformed rigidity grid near the Nyquist wavenumber. The half-wavelength of this Gaussian filter is 10 pixels which is similar to the smoothing needed for the cracked plate benchmark.

While this paper is largely focussed on potential applications to modelling flexure outboard of trenches, the model formulation is quite general and could be applied to any thin-plate flexure problem where variable rigidity is needed. One case where this method (1-D) was already used is to model the flexural evolution of an oceanic fracture zone where a step contrast in age across the fracture zone results in a sharp contrast in flexural rigidity (Sandwell, 1984). The young side of the fracture zone subsides at a faster rate than the older side and this differential subsidence drives the flexure. Another potential example is the modelling of flexure beneath very large seamounts which have bent the plate beyond its elastic limits. Accordingly, a cracked plate model has been proposed for the Hawaiian Chain (Watts, 2001). A third potential application is the flexure of foreland basins where the amplitude of the flexure is sufficient to weaken the plate (Watts, 2001). Indeed this formulation could be used to model any type of thin plate flexure where the size of the plate is much greater than the flexural wavelength such that the boundary conditions given in equations (3.3) and (3.4) are appropriate.

3.5 Conclusions

We have developed a 2-D iterative spectral method to compute the flexural response of a thin elastic plate of variable rigidity floating on an inviscid fluid half space that is subjected to an arbitrary vertical load and in-plane force. The method will converge as long as the spatial variations in flexural rigidity are band-limited. In practice we note that the rigidity grid must be low-pass filtered over a distance of about 10 pixels to achieve convergence.

We have assembled 7 analytical benchmarks for testing the code. Five of these benchmarks have uniform rigidity plates so accurate solutions are achieved

in 1 iteration. The two non-uniform rigidity benchmarks correspond to a broken plate and a plate with a step in rigidity. The numerical result for the 1000-times step variation in rigidity shows excellent agreement with the analytic solution while there are up to 10% differences between the numerical broken plate result and its analytic solution. This broken plate case reveals the limitation of the approach in that the rigidity must be smooth relative the Nyquist wavelength, but can still vary over wavelengths shorter than the flexural wavelenth. For earth applications we expect smooth spatial variations in rigidity in this range so the accuracy of the solutions should be better than the 10%.

To illustrate the 2-D capabilities of the approach we considered three variable rigidity test cases to simulate subduction zones. The first case has a sinusoidal trench planform and dramatic weakening of the "subducted" plate. The results show a factor of 1.5 difference in outer rise height on the plate outboard of the concave trench planform relative to the plate outboard of the convex trench planform. This highlights the need to have a 2-D formulation for modelling actual trenches. The second case is a linear trench where the subducting plate has an along-trench ramp in elastic thickness from 5 km to 25 km. As expected the flexural profiles across the trench vary dramatically with the underlying plate thickness. In the third case, we have combined these two features to simulate a more realistic subduction geometry with a synthetic model of the Chile trench, offshore South America. This final model demonstrates the utility we expect this solution to bring to flexural modeling studies in the future.

Finally we note that the vertical loading grid and rigidity grids can be arbitrarily complex as long as they satisfy the smoothness needed for convergence. Therefore this approach could be applied to all types of geophysical flexure problems ranging from seamount loading to thermomechanical evolution of sedimentary basins.

3.6 Acknowledgements

We thank Rachel Marcuson and Matthew Siegfried for constructive comments on early drafts of the manuscript. We also thank Paul Wessel for helpful discussions on flexural modeling. This research was supported by the National Science Foundation (OCE-1128801) and the Office of Naval Research (N00014-12-1-0111).

Chapter 3, in full, is a reprint of the material as it appears in the Geophysical Journal International: Garcia, E.S., D.T. Sandwell, K.M. Luttrell, "An iterative spectral solution method for thin elastic plate flexure with variable rigidity", *Geophysical Journal International*, 200(2): 1010-1026, doi: 10.1093/gji/ggu449, 2015. The dissertation author was the primary investigator and author of the paper.

Appendices

3.A Expressing 2-D flexure as a Fredholm integral equation of the second kind

Recall that we specified the following decomposition for the plate rigidity $D(x, y)$ in (3.7) in the main text,

$$D(x, y) = D_0 + D'(x, y) \tag{3.24}$$

By its definition as a material parameter, the plate rigidity cannot have a negative value, so a restriction for $D'(x, y)$ is that $D'(x, y) > -D_0$ for all (x, y). If we substitute the above decomposition for D into the governing equation (3.2),

$$\begin{aligned} D_0\nabla^2\left(\nabla^2 w\right) + \nabla^2\left[D'\nabla^2 w\right] - (1-\nu)\left[\frac{\partial^2 D'}{\partial x^2}\frac{\partial^2 w}{\partial y^2} - 2\frac{\partial^2 D'}{\partial x \partial y}\frac{\partial^2 w}{\partial x \partial y} + \frac{\partial^2 D'}{\partial y^2}\frac{\partial^2 w}{\partial x^2}\right] \\ - N_x\frac{\partial^2 w}{\partial x^2} - 2N_{xy}\frac{\partial^2 w}{\partial x \partial y} - N_y\frac{\partial^2 w}{\partial y^2} + \Delta\rho g w = p \end{aligned} \tag{3.25}$$

Eventually, we will express this partial differential equation in the space domain as an integral equation in the wavenumber, or Fourier domain. Formally, the two-dimensional Fourier transform of a function f is defined as,

$$\mathcal{F}\left[f(\boldsymbol{r})\right] = \hat{f}(\boldsymbol{k}) = \int_X dS\, f(\boldsymbol{r}) e^{-i2\pi \boldsymbol{k}\cdot\boldsymbol{r}} \tag{3.26}$$

The surface integral is taken over the entire x-y plane denoted by X. The transformed function $\hat{f}$ is a function of the wave vector $\boldsymbol{k}$, which has components k_x and k_y. In this work, we evaluate (3.26) and the corresponding inverse Fourier transform using iterated integrals over x and y, as well as k_x and k_y,

$$\mathcal{F}\left[f(\boldsymbol{r})\right] = \hat{f}(\boldsymbol{k}) = \int_{-\infty}^{+\infty}\int_{-\infty}^{+\infty} dx\, dy\, f(x,y) e^{-i2\pi(k_x x + k_y y)} \tag{3.27}$$

$$\mathcal{F}^{-1}\left[\hat{f}(\boldsymbol{k})\right] = f(\boldsymbol{r}) = \int_{-\infty}^{+\infty}\int_{-\infty}^{+\infty} dk_x\, dk_y\, f(k_x,k_y) e^{i2\pi(k_x x + k_y y)} \tag{3.28}$$

We assume that D' and w are band-limited functions so that their Fourier transforms exist. These variables can therefore be written using inverse Fourier transforms over the dummy variables (ζ_x, ζ_y) and (s_x, s_y) respectively,

$$D'(x,y) = \int_{-\infty}^{+\infty}\int_{-\infty}^{+\infty} d\zeta_x\, d\zeta_y\, \hat{D}'(\zeta_x,\zeta_y) e^{i2\pi(\zeta_x x + \zeta_y y)} \tag{3.29}$$

$$w(x,y) = \int_{-\infty}^{+\infty}\int_{-\infty}^{+\infty} ds_x\, ds_y\, \hat{w}(s_x,s_y) e^{i2\pi(s_x x + s_y y)} \tag{3.30}$$

The expressions (3.29) and (3.30) are then substituted in the governing equation (3.2). After performing this substitution, we interchange the order of integration with respect to ζ_x and s_x and similarly for ζ_y and s_y. This manipulation is valid when the absolute value of the integrands are finite. Carrying out the successive differentiations over x and y leads to:

$$\int_{-\infty}^{+\infty}\int_{-\infty}^{+\infty} ds_x\, ds_y \left\{ \left[(2\pi)^4 D_0 \left(s_x^2 + s_y^2\right)^2 + (2\pi)^2 \left(N_x s_x^2 + 2N_{xy} s_x s_y + N_y s_y^2\right) + \Delta\rho g \right] \right.$$
$$\left. \times \hat{w}(s_x, s_y) e^{i2\pi(s_x x + s_y y)} \right\}$$
$$+(2\pi)^4 \int_{-\infty}^{+\infty}\int_{-\infty}^{+\infty}\int_{-\infty}^{+\infty}\int_{-\infty}^{+\infty} ds_x\, ds_y\, d\zeta_x\, d\zeta_y \left\{ \left[(s_x + \zeta_x)^2 + (s_y + \zeta_y)^2 \right] \left(s_x^2 + s_y^2\right) \right.$$
$$\left. \times \hat{D}'(\zeta_x, \zeta_y) \hat{w}(s_x, s_y) e^{i2\pi[(s_x+\zeta_x)x + (s_y+\zeta_y)y]} \right\}$$
$$-(2\pi)^4 (1-\nu) \int_{-\infty}^{+\infty}\int_{-\infty}^{+\infty}\int_{-\infty}^{+\infty}\int_{-\infty}^{+\infty} ds_x\, ds_y\, d\zeta_x\, d\zeta_y \left\{ \left[s_x^2 \zeta_y^2 - 2 s_x \zeta_x s_y \zeta_y + s_y^2 \zeta_x^2 \right] \right.$$
$$\left. \times \hat{D}'(\zeta_x, \zeta_y) \hat{w}(s_x, s_y) e^{i2\pi[(s_x+\zeta_x)x + (s_y+\zeta_y)y]} \right\} = p(x, y) \tag{3.31}$$

All the terms in the above equation are still functions of (x, y) since we are just using integral representations for the terms in the left hand side (LHS). We can then apply the forward transform (3.27) to both sides of the equation and get:

$$\int_{-\infty}^{+\infty}\int_{-\infty}^{+\infty} dx\,dy \int_{-\infty}^{+\infty}\int_{-\infty}^{+\infty} ds_x\,ds_y \left\{ \left\{ (2\pi)^4 D_0 \left(s_x^2+s_y^2\right)^2 \right.\right.$$

$$\left.\left. +(2\pi)^2 \left(N_x s_x^2 + 2N_{xy} s_x s_y + N_y s_y^2\right) + \Delta\rho g \right\} \hat{w}(s_x,s_y) e^{i2\pi[(s_x-k_x)x+(s_y-k_y)y]} \right\}$$

$$+(2\pi)^4 \int_{-\infty}^{+\infty}\int_{-\infty}^{+\infty} dx\,dy \int_{-\infty}^{+\infty}\int_{-\infty}^{+\infty}\int_{-\infty}^{+\infty}\int_{-\infty}^{+\infty} ds_x\,ds_y\,d\zeta_x\,d\zeta_y \left\{ \left[(s_x+\zeta_x)^2+(s_y+\zeta_y)^2\right] \left(s_x^2+s_y^2\right) \right.$$

$$\left. \times \hat{D}'(\zeta_x,\zeta_y)\hat{w}(s_x,s_y) e^{i2\pi[(s_x+\zeta_x-k_x)x+(s_y+\zeta_y-k_y)y]} \right\}$$

$$-(2\pi)^4(1-\nu) \int_{-\infty}^{+\infty}\int_{-\infty}^{+\infty} dx\,dy \int_{-\infty}^{+\infty}\int_{-\infty}^{+\infty}\int_{-\infty}^{+\infty}\int_{-\infty}^{+\infty} ds_x\,ds_y\,d\zeta_x\,d\zeta_y \left\{ \left[s_x^2\zeta_y^2 - 2s_x\zeta_x s_y\zeta_y + s_y^2\zeta_x^2\right] \right.$$

$$\left. \times \hat{D}'(\zeta_x,\zeta_y)\hat{w}(s_x,s_y) e^{i2\pi[(s_x+\zeta_x-k_x)x+(s_y+\zeta_y-k_y)y]} \right\} = \hat{p}(k_x,k_y) \tag{3.32}$$

From the properties of the Dirac delta distribution, we can write the following relations:

$$\int_{-\infty}^{+\infty} dx\ e^{i2\pi(s_x-k_x)x} = \delta(s_x-k_x) \quad , \qquad \int_{-\infty}^{+\infty} dx\ e^{i2\pi[\zeta_x-(k_x-s_x)]x} = \delta[\zeta_x-(k_x-s_x)] \tag{3.33}$$

$$\int_{-\infty}^{+\infty} dy\ e^{i2\pi(s_y-k_y)y} = \delta(s_y-k_y) \quad , \qquad \int_{-\infty}^{+\infty} dy\ e^{i2\pi[\zeta_y-(k_y-s_y)]y} = \delta[\zeta_y-(k_y-s_y)] \tag{3.34}$$

We substitute these relations (3.33)-(3.34) into (3.32), and then integrate over s_x and s_y for the first set of integrals, while we integrate over ζ_x, ζ_y for the remaining set of integrals. What remains after invoking the sifting property of the Dirac delta distribution is an equation in the wavenumber domain:

$$\Big[(2\pi)^4 D_0\left(k_x^2+k_y^2\right)^2+(2\pi)^2\left(N_x k_x^2+2N_{xy}k_xk_y+N_y k_y^2\right)+\Delta\rho g\Big]\,\hat{w}$$
$$+(2\pi)^4\int_{-\infty}^{+\infty}\int_{-\infty}^{+\infty} ds_x\,ds_y\,\left(k_x^2+k_y^2\right)^2\left(s_x^2+s_y^2\right)^2\hat{D}'(k_x-s_x,k_y-s_y)\hat{w}(s_x,s_y)$$
$$-(2\pi)^4(1-\nu)\int_{-\infty}^{+\infty}\int_{-\infty}^{+\infty} ds_x\,ds_y\left\{\Big[s_x^2(k_y-s_y)^2-2s_x(k_x-s_x)s_y(k_y-s_y)\right.$$
$$\left.+s_y^2(k_x-s_x)^2\Big]\hat{D}'(k_x-s_x,k_y-s_y)\hat{w}(s_x,s_y)\right\}=\hat{p} \quad (3.35)$$

Rearranging terms slightly and combining the integrals over s_x and s_y, we see that this can be cast in the form of an integral equation,

$$\Big[(2\pi)^4 D_0\left(k_x^2+k_y^2\right)^2+(2\pi)^2\left(N_x k_x^2+2N_{xy}k_xk_y+N_y k_y^2\right)+\Delta\rho g\Big]\,\hat{w}=$$
$$\hat{p}(k_x,k_y)-(2\pi)^4\int_{-\infty}^{+\infty}\int_{-\infty}^{+\infty} ds_x\,ds_y\left\{\left(k_x^2+k_y^2\right)^2\left(s_x^2+s_y^2\right)^2-(1-\nu)\Big\{s_x^2(k_y-s_y)^2\right.$$
$$\left.-2s_x(k_x-s_x)s_y(k_y-s_y)+s_y^2(k_x-s_x)^2\Big\}\hat{D}'(k_x-s_x,k_y-s_y)\hat{w}(s_x,s_y)\right\} \quad (3.36)$$

We can write (3.36) compactly by adopting a couple of definitions. First, we recall the form of the response function to uniform rigidity D_0, given in (3.6). Second, we define the kernel $K(k_x,s_x;k_y,s_y)$ as:

$$K(k_x,s_x;k_y,s_y)=-(2\pi)^4\hat{\Phi}\Big\{\left(k_x^2+k_y^2\right)^2\left(s_x^2+s_y^2\right)^2-$$
$$(1-\nu)s_x^2(k_y-s_y)^2-2s_x(k_x-s_x)s_y(k_y-s_y)$$
$$+s_y^2(k_x-s_x)^2\Big\}\hat{D}'(k_x-s_x,k_y-s_y) \quad (3.37)$$

Using the notations specified by (3.6) and (3.37) enables us to express (3.36) in the standard form of a two-dimensional Fredholm integral equation of the second kind,

$$\hat{w}(k_x, k_y) = \hat{p}(k_x, k_y)\hat{\Phi}(k_x, k_y) + \int_{-\infty}^{+\infty}\int_{-\infty}^{+\infty} ds_x\, ds_y\, K(k_x, s_x; k_y, s_y)\hat{w}(s_x, s_y) \quad (3.38)$$

where the nonhomogeneous term of the integral equation is $p(k_x, k_y)\hat{\Phi}(k_x, k_y)$, which is identical to the uniform plate solution $\hat{w}_0(k_x, k_y)$ stated in (3.5). Verifying that (3.36) is indeed a Fredholm integral equation of the second kind enables us to refer to the well-developed theory behind these types of equations in establishing the existence and uniqueness of a solution. If a solution $\hat{w}$ can be found in the Fourier domain, then by taking the inverse transform we obtain the desired solution $w(x, y)$ to the governing equation (3.2). One method of solving Fredholm integral equations is through successive approximation, and in the following section we describe our implementation of such an iterative algorithm.

3.B An iterative scheme to solve the equivalent integral equation

If we consider the Fredholm integral equation of the second kind as expressed in (3.38) with kernel (3.37), for many forms of D' (and hence $\hat{D}'$), the kernel turns out to be neither symmetric, degenerate, nor separable. This implies that some standard methods of solving integral equations are not feasible for our purposes. Ideally, we want to develop a computational framework for solving thin elastic plate flexure problems involving arbitrary variations in rigidity, valid under some criterion of smoothness. In pursuit of this generality, we resort to an iterative solution method.

A solution to the Fredholm integral equation (3.38) can be obtained by starting with a guess for $\hat{w}$, then evaluating the right hand side (RHS) of the equation. This result is then substituted again into the RHS, giving a new estimate for the solution. The process is repeated until the desired accuracy is reached. We will delve further into the conditions for the convergence of this scheme in the next section. In the meantime, we will be demonstrating the iteration process. Suppose

that our guess is $\hat{w} = 0$ for all wavenumbers, and so by substituting this into the RHS of (3.38), we get that the first solution is $\hat{w}^{(1)} = \hat{w}_0$. By induction, the n-th approximation to the solution of the integral equation is given by

$$\hat{w}^{(n)} = \hat{w}_0 + \int_{-\infty}^{+\infty}\int_{-\infty}^{+\infty} ds_x\, ds_y\, K(k_x, s_x; k_y, s_y)\hat{w}^{(n-1)}(s_x, s_y) \tag{3.39}$$

At each step of the algorithm, we substitute the kernel as given in (3.37), then calculate the integral. This may be done completely in the wavenumber domain. However, as some of the individual terms comprising $K(k_x, s_x; k_y, s_y)$ are in the form of a convolution, they may also be computed as multiplications in the space domain. To see this, we rewrite the integrand by separating it according to the constituent terms of the kernel:

$$\begin{aligned}
&\int_{-\infty}^{+\infty}\int_{-\infty}^{+\infty} ds_x\, ds_y\, K(k_x, s_x; k_y, s_y)\hat{w}^{(n-1)}(s_x, s_y) = \\
-(2\pi)^4\hat{\Phi}\Bigg\{ &\left(k_x^2 + k_y^2\right)^2 \int_{-\infty}^{+\infty}\int_{-\infty}^{+\infty} ds_x\, ds_y \left[\hat{D}'(k_x - s_x, k_y - s_y)\right] \\
&\qquad \times \left[\left(s_x^2 + s_y^2\right)^2 \hat{w}^{(n-1)}(s_x, s_y)\right] \\
-(1-\nu)\Big\{ &\int_{-\infty}^{+\infty}\int_{-\infty}^{+\infty} ds_x\, ds_y \left[(k_y - s_y)^2\hat{D}'(k_x - s_x, k_y - s_y)\right] \\
&\qquad \times \left[s_x^2\hat{w}^{(n-1)}(s_x, s_y)\right] \\
-2\int_{-\infty}^{+\infty}\int_{-\infty}^{+\infty} &ds_x\, ds_y \left[(k_x - s_x)(k_y - s_y)\hat{D}'(k_x - s_x, k_y - s_y)\right] \\
&\qquad \times \left[s_x s_y\hat{w}^{(n-1)}(s_x, s_y)\right] \\
+\int_{-\infty}^{+\infty}\int_{-\infty}^{+\infty} &ds_x\, ds_y \left[(k_x - s_x)^2\hat{D}'(k_x - s_x, k_y - s_y)\right] \\
&\qquad \times \left[s_y^2\hat{w}^{(n-1)}(s_x, s_y)\right]\Big\}\Bigg\}
\end{aligned} \tag{3.40}$$

The individual terms on the RHS may be identified as convolutions in the wavenumber domain. By the convolution theorem, these terms have equivalent representations in the space domain. The presence of terms proportional to powers of the wavenumber components suggests that we are dealing with the derivatives of D' and w. Thus, an alternate way of expressing (3.40) is

$$\int_{-\infty}^{+\infty}\int_{-\infty}^{+\infty} ds_x\, ds_y\, K(k_x, s_x; k_y, s_y)\hat{w}^{(n-1)}(s_x, s_y) = \\ -\hat{\Phi}(k_x, k_y)\mathcal{F}\Bigg\{\nabla^2\left[D'\nabla^2 w^{(n-1)}\right] \\ -(1-\nu)\left[\frac{\partial^2 D'}{\partial x^2}\frac{\partial^2 w}{\partial y^2}^{(n-1)} - 2\frac{\partial^2 D'}{\partial x \partial y}\frac{\partial^2 w}{\partial x \partial y}^{(n-1)} + \frac{\partial^2 D'}{\partial y^2}\frac{\partial^2 w}{\partial x^2}^{(n-1)}\right]\Bigg\} \tag{3.41}$$

Substitution of (3.41) in (3.39) leads to the expression (3.9) that was presented and discussed in the main body of the paper.

3.C Conditions for Convergence of the Iterative Solution

The Fredholm theory of integral equations provides a framework for discussing the existence and uniqueness of a solution obtained by an iterative technique. When written in a standard form such as in (3.38), the RHS of an integral equation is regarded as an operator $\mathcal{T}$ acting on the unknown function. In our case, the unknown function we are solving for is $\hat{w}$, and the operator $\mathcal{T}[\hat{w}]$ may be defined as,

$$\mathcal{T}[\hat{w}] = \hat{w}_0 + \int_{-\infty}^{+\infty}\int_{-\infty}^{+\infty} ds_x\, ds_y\, K(k_x, s_x; k_y, s_y)\hat{w}(s_x, s_y) \tag{3.42}$$

In the operator view of integral equations, the Banach fixed point theorem ensures that a unique solution will exist for $\hat{w} = \mathcal{T}[\hat{w}]$ for a contractive mapping

$\mathcal{T}$ on a complete metric space (Korevaar, 1968; Jerri, 1999). Now, the operator $\mathcal{T}$ can be considered to be a contractive mapping on the metric space $\mathcal{M}$ if for each $u_1, u_2 \in \mathcal{M}$ the following relation holds,

$$d(\mathcal{T}(u_1), \mathcal{T}(u_2)) \leq \Upsilon d(u_1, u_2) \tag{3.43}$$

In the above condition, $0 < \Upsilon < 1$, and the metric d between two continuous functions $u_1(\boldsymbol{k})$ and $u_2(\boldsymbol{k})$ in the set $\mathcal{C}[(\xi_a, \xi_b); (\eta_a, \eta_b)]$ is defined as

$$\begin{aligned} &d(u_1(k_x, k_y), u_2(k_x, k_y)) = \\ &\max_{(k_x,k_y)\in[(\xi_a,\xi_b);(\eta_a,\eta_b)]} \Big| u_1((k_x, k_y), u_2(k_x, k_y)) - u_2((k_x, k_y), u_2(k_x, k_y)) \Big| \end{aligned} \tag{3.44}$$

Before we evaluate the criterion (3.43) as it applies to consecutive estimates of $\hat{w}$ resulting from the iterations, we make a few more assumptions. First, $\hat{w}_0$ must be continuous over the region described by $(k_x, k_y) \in [(\xi_a, \xi_b); (\eta_a, \eta_b)]$. The kernel $K(k_x, s_x; k_y, s_y)$ must also be continuous in $\Big\{(k_x, s_x; k_y, s_y) : (k_x, k_y) \in [(\xi_a, \xi_b); (\eta_a, \eta_b)],\ (s_x, s_y) \in [(\xi_a, \xi_b); (\eta_a, \eta_b)]\Big\}$. Furthermore, the kernel must be bounded such that $|K(k_x, s_x; k_y, s_y)| < \vartheta$ where ϑ is some finite constant. Note that these assumptions are consistent with our previously set requirements that the Fourier transforms of the load distribution p and rigidity D must exist, and furthermore band-limited.

Considering the LHS of (3.43) as it applies to successive estimates for $\hat{w}$, we get

$$
\begin{aligned}
&d(\mathcal{T}(\hat{w}_{n+1}), \mathcal{T}(\hat{w}_n)) = \\
&\max_{(k_x,k_y)\in[(\xi_a,\xi_b);(\eta_a,\eta_b)]} \Bigg| \hat{w}_0 + \int_{\xi_a}^{\xi_b}\int_{\eta_a}^{\eta_b} ds_x\, ds_y\, K(k_x, s_x; k_y, s_y)\hat{w}^{(n+1)}(s_x, s_y) \\
&\qquad\qquad -\hat{w}_0 - \int_{\xi_a}^{\xi_b}\int_{\eta_a}^{\eta_b} ds_x\, ds_y\, K(k_x, s_x; k_y, s_y)\hat{w}^{(n)}(s_x, s_y) \Bigg| \\
&d(\mathcal{T}(\hat{w}_{n+1}), \mathcal{T}(\hat{w}_n)) = \\
&\max_{(k_x,k_y)\in[(\xi_a,\xi_b);(\eta_a,\eta_b)]} \left| \int_{\xi_a}^{\xi_b}\int_{\eta_a}^{\eta_b} ds_x\, ds_y\, K(k_x, s_x; k_y, s_y) \left[\hat{w}^{(n)}(s_x, s_y) - \hat{w}^{(n+1)}(s_x, s_y))\right] \right|
\end{aligned}
\tag{3.45}
$$

Meanwhile, it may be shown that the RHS fulfills the inequality

$$
\begin{aligned}
&\max_{(k_x,k_y)\in[(\xi_a,\xi_b);(\eta_a,\eta_b)]} \left| \int_{\xi_a}^{\xi_b}\int_{\eta_a}^{\eta_b} ds_x\, ds_y\, K(k_x, s_x; k_y, s_y) \left[\hat{w}^{(n)}(s_x, s_y) - \hat{w}^{(n+1)}(s_x, s_y))\right] \right| \\
&\qquad \leq \max_{(k_x,k_y)\in[(\xi_a,\xi_b);(\eta_a,\eta_b)]} \left| \hat{w}^{(n)}(s_x, s_y) - \hat{w}^{(n+1)}(s_x, s_y)) \right| \\
&\qquad \times \max_{(k_x,k_y)\in[(\xi_a,\xi_b);(\eta_a,\eta_b)]} \int_{\xi_a}^{\xi_b}\int_{\eta_a}^{\eta_b} ds_x\, ds_y \left| K(k_x, s_x; k_y, s_y) \right| \\
&\max_{(k_x,k_y)\in[(\xi_a,\xi_b);(\eta_a,\eta_b)]} \left| \int_{\xi_a}^{\xi_b}\int_{\eta_a}^{\eta_b} ds_x\, ds_y\, K(k_x, s_x; k_y, s_y) \left[\hat{w}^{(n)}(s_x, s_y) - \hat{w}^{(n+1)}(s_x, s_y))\right] \right| \\
&\qquad \leq d\left(\hat{w}^{(n+1)}, \hat{w}^{(n)}\right) \max_{(k_x,k_y)\in[(\xi_a,\xi_b);(\eta_a,\eta_b)]} \int_{\xi_a}^{\xi_b}\int_{\eta_a}^{\eta_b} ds_x\, ds_y \left| K(k_x, s_x; k_y, s_y) \right|
\end{aligned}
\tag{3.46}
$$

as in (Korevaar, 1968) and following the definition of the metric (3.44). If we compare the right hand side of (3.43) with the required convergence criteria for this case, which is

$$
d(\mathcal{T}(\hat{w}^{(n+1)}), \mathcal{T}(\hat{w}^{(n)})) \leq \Upsilon d\left(\hat{w}^{(n+1)}, \hat{w}^{(n)}\right) \tag{3.47}
$$

then $\Upsilon = \max_{(k_x,k_y)\in[(\xi_a,\xi_b);(\eta_a,\eta_b)]} \int_{\xi_a}^{\xi_b}\int_{\eta_a}^{\eta_b} ds_x\, ds_y \left| K(k_x, s_x; k_y, s_y) \right|$ and so the condition for convergence is just

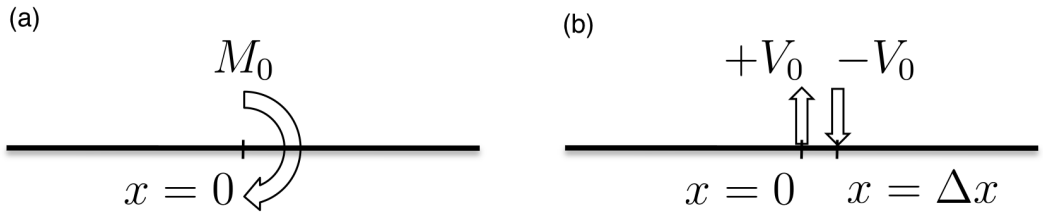

Figure 3.D.1: (a) A clockwise moment M_0 is applied at the origin. (b) The flexural deflection due to M_0 may be approximated as being due to the superposition of two opposing loads of equal magnitude V_0 placed a small distance Δx apart.

$$\max_{(k_x,k_y)\in[(\xi_a,\xi_b);(\eta_a,\eta_b)]} \int_{\xi_a}^{\xi_b} \int_{\eta_a}^{\eta_b} ds_x\, ds_y\, |K(k_x, s_x; k_y, s_y)| < 1 \tag{3.48}$$

Thus, for a fixed point to exist and for the iterative scheme to converge, the maximum of the integral of the absolute value of the kernel over the wavenumber bands of interest must be a sufficiently small value. The implication for the form of D and q in the space domain is that they must be smoothly varying functions over a narrow range of spatial scales.

3.D Approximating Applied Moments with Vertical Load Couples

Following an approximation that may be taken for infinite one-dimensional beams (Hetenyi, 1946; Watts, 2001), we also tested how well a moment along the x-direction M_0 applied to an interior point of the plate can be represented as a pair of opposing vertical loads V_0 separated by an infinitesimal distance Δx. This may be expressed formally as,

$$M_0 \approx \lim_{\Delta x \to 0} V_0 \Delta x \tag{3.49}$$

Since the system (3.2) is linear, the solution for the deflection w due to two opposing loads is simply the superposition of the individual solutions for each of the loads. Thus, in 1-D, if $+V$ is applied at $x = 0$ and $-V$ at $x = \Delta x$, and if we refer to the solution in the line load case (3.10) as w_V, then solution for this load couple w_c is given by the sum

$$w_M = w_V(x + \Delta x) - w_V(x) \tag{3.50}$$

Rewriting this expression slightly,

$$w_M = \Delta x \frac{w_V(x + \Delta x) - w_V(x)}{\Delta x} \tag{3.51}$$

Thus, as Δx becomes small,

$$w_M = \Delta x \lim_{\Delta x \to 0} \frac{w_V(x + \Delta x) - w_V(x)}{\Delta x} \approx \Delta x \frac{\partial w_V}{\partial x} \tag{3.52}$$

Recalling (3.10) and taking its derivative along x, we get

$$w_M(x) = -\frac{V \Delta x \alpha^2}{4D_0} \exp\left(-\frac{|x|}{\alpha}\right) \sin\left(\frac{x}{\alpha}\right) \approx -\frac{M_0 \alpha^2}{4D_0} \exp\left(-\frac{|x|}{\alpha}\right) \sin\left(\frac{x}{\alpha}\right) \tag{3.53}$$

following our assumption that $V\Delta x$ approaches M_0. Thus, the approximate solution for an applied moment M_0 is (Hetenyi, 1946)

$$w = -w_m \exp\left(-\frac{|x|}{\alpha}\right) \sin\left(\frac{x}{\alpha}\right) \tag{3.54}$$

where $w_m = M_0\alpha^2/4D_0$, which is included in the main text as equation (3.17).

We may apply the same set of assumptions to obtain an expression for the deflection due to a concentrated moment on a two-dimensional infinite plate. First, recall that the solution w for a point load with amplitude V_0 can be written in terms of the Kelvin-Bessel function Kei of order zero as (Brotchie, 1971; Lambeck & Nakiboglu, 1980)

$$w = w_p \mathrm{Kei}_0 \left[\frac{(x^2 + y^2)^{1/2}}{l}\right] \tag{3.55}$$

where $w_p = V_0 l^2/2\pi D_0$ and the flexural parameter l is

$$l = \left[\frac{D_0}{\Delta\rho g}\right]^{1/4} \tag{3.56}$$

By taking the partial derivative with respect to x of (3.55), the solution for a concentrated moment aligned with the x-axis is

$$w = w_r \left\{ \mathrm{Kei}_1 \left[\frac{(x^2+y^2)^{1/2}}{l}\right] - \mathrm{Ker}_1 \left[\frac{(x^2+y^2)^{1/2}}{l}\right] \right\} \tag{3.57}$$

where we are using Kelvin-Bessel functions Ker and Kei of order 1, and $w_r = w_q \left[x/2^{1/2} l\,(x^2+y^2)^{1/2}\right]$, with $w_q = M_0 l^2/2\pi D_0$. This is also included in the main text as equation (3.19).

3.E Expressions for the Solution of a Line Moment Applied to a Plate with Piecewise Rigidity

We derive the analytic solution for deflection produced by a line moment applied to a plate with a sharp step in flexural rigidity such that

$$D(x) = \begin{cases} D_1 & : x < 0 \\ D_2 & : x > 0 \end{cases} \tag{3.58}$$

following the approach of (Sandwell & Schubert, 1982). In the absence of in-plane forces, the governing equations may be written as a coupled system:

$$D_1 \frac{d^4 w_1}{dx^4} + \Delta\rho g w_1 = 0 \quad : x > 0 \tag{3.59}$$

$$D_2 \frac{d^4 w_2}{dx^4} + \Delta\rho g w_2 = 0 \quad : x < 0 \tag{3.60}$$

The boundary conditions are that the deflections w_1, w_2 and their slopes vanish as $|x| \to \infty$. The general solutions in each region of the plate have the form

$$w_1 = \exp\left(\frac{x}{\alpha_1}\right)\left[A_1\cos\left(\frac{x}{\alpha_1}\right) + B_1\sin\left(\frac{x}{\alpha_1}\right)\right] \quad : x < 0 \tag{3.61}$$

$$w_2 = \exp\left(-\frac{x}{\alpha_2}\right)\left[A_2\cos\left(\frac{x}{\alpha_2}\right) + B_1\sin\left(\frac{x}{\alpha_2}\right)\right] \quad : x > 0 \tag{3.62}$$

Note that the flexural parameters α_1 and α_2 are different for each region,

$$\alpha_{1,2} = \left[\frac{4D_{1,2}}{\Delta\rho g}\right]^{1/4} \tag{3.63}$$

The plate is subject to a line moment applied at $x = 0$. Apart from the boundary conditions at the edges of the model, the following matching conditions must also be fulfilled at the discontinuity in rigidity (also at $x = 0$):

$$w_1 - w_2 = 0 \tag{3.64}$$

$$\frac{dw_1}{dx} - \frac{dw_2}{dx} = 0 \tag{3.65}$$

$$-D_1\frac{d^2w_1}{dx^2} - D_2\frac{d^2w_2}{dx^2} = M_0 \tag{3.66}$$

$$-D_1\frac{d^3w_1}{dx^3} - D_2\frac{d^3w_2}{dx^3} = 0 \tag{3.67}$$

These matching conditions ensure the continuity of the deflections, slopes, and shear forces. The third condition accounts for the applied moment at the origin. Solving the linear system resulting from these matching conditions leads to explicit expressions for the unknown coefficients A_1, B_1, A_2 and B_2 in (3.61-3.62).

In our solution, we found that $A_1 = A_2 = A$, which may be expressed in terms of the flexural parameters $\alpha_{1,2}$ and the moment M_0 as

$$A = -\frac{\frac{1}{\alpha_1}\left(1 + \frac{\alpha_1}{D_1}\frac{D_2}{\alpha_2}\right) - \frac{\alpha_1}{D_1}\frac{D_2}{\alpha_2}\left(\frac{1}{\alpha_1} + \frac{1}{\alpha_2}\right)}{\left(\frac{D_1}{\alpha_1^3} + \frac{D_1}{\alpha_2^3}\right)\left(1 + \frac{\alpha_1}{D_1}\frac{D_2}{\alpha_2}\right) + \frac{D_2}{\alpha_2}\left(\frac{1}{\alpha_1} + \frac{1}{\alpha_2}\right)^2}\left(\frac{M_0}{2}\right) \tag{3.68}$$

The respective expressions for B_1 and B_2 are

$$B_1 = \frac{\alpha_1^2}{D_1}\left(\frac{M_0}{2} + \frac{D_2}{\alpha_2^2}B_2\right) \tag{3.69}$$

$$B_2 = \frac{\alpha_2\left[\frac{\alpha_1}{D_1}\frac{M_0}{2} + \left(\frac{1}{\alpha_1} + \frac{1}{\alpha_2}\right)A\right]}{\left(1 + \frac{\alpha_1}{D_1}\frac{D_2}{\alpha_2}\right)} \tag{3.70}$$

References

Banks, R. J., Parker, R. L., & Huestis, S. P., 1977. Isostatic compensation on a continental scale: local versus regional mechanisms, *Geophysical Journal International*, **51**(2), 431–452.

Barbot, S., Fialko, Y., & Sandwell, D., 2008. Effect of a compliant fault zone on the inferred earthquake slip distribution, *Journal of Geophysical Research*, **113**(B6).

Bodine, J. & Watts, A., 1979. On lithospheric flexure seaward of the bonin and mariana trenches, *Earth and Planetary Science Letters*, **43**(1), 132–148.

Braitenberg, C., Ebbing, J., & Gtze, H.-J., 2002. Inverse modelling of elastic thickness by convolution method the eastern alps as a case example, *Earth and Planetary Science Letters*, **202**(2), 387–404.

Brenner, N., 1967. Three fortran programs that perform the cooley-tukey fourier transform, Tech. rep., DTIC Document.

Brotchie, J. F., 1971. Flexure of a liquid-filled spherical shell in a radial gravity field, *Modern Geology*, **3**, 15–23.

Bry, M. & White, N., 2007. Reappraising elastic thickness variation at oceanic trenches, *Journal of Geophysical Research*, **112**(B8).

Caldwell, J. G., Haxby, W. F., Karig, D. E., & Turcotte, D. L., 1976. On the applicability of a universal elastic trench profile, *Earth and Planetary Science Letters*, **31**(2), 239–246.

Contreras-Reyes, E. & Osses, A., 2010. Lithospheric flexure modelling seaward of the chile trench: implications for oceanic plate weakening in the trench outer rise region, *Geophysical Journal International*, **182**(1), 97–112.

Craig, T., Copley, A., & Jackson, J., 2014. A reassessment of outer-rise seismicity and its implications for the mechanics of oceanic lithosphere, *Geophysical Journal International*, **197**(1), 63–89.

de Bremaecker, J.-C., 1977. Is the oceanic lithosphere elastic or viscous?, *Journal of Geophysical Research*, **82**(14), 2001–2004.

Erickson, S. G., 1993. Sedimentary loading, lithospheric flexure, and subduction initiation at passive margins, *Geology*, **21**(2), 125.

Garcia-Castellanos, D., 2002. Interplay between lithospheric flexure and river transport in foreland basins, *Basin Research*, **14**(2), 89–104.

Goetze, C. & Evans, B., 1979. Stress and temperature in the bending lithosphere as constrained by experimental rock mechanics, *Geophysical Journal International*, **59**(3), 463–478.

Hanks, T. C., 1971. The kuril trench - hokkaido rise system: Large shallow earthquakes and simple models of deformation, *Geophysical Journal International*, **23**(2), 173–189.

Hetenyi, M., 1946. *Beams on elastic foundation : theory with applications in the fields of civil and mechanical engineering*, The University of Michigan press, Ann Arbor.

Jerri, A. J., 1999. *Introduction to integral equations with applications*, Wiley, New York, 2nd edn.

Kim, S.-S. & Wessel, P., 2010. Flexure modelling at seamounts with dense cores: Flexure modelling with dense core loads, *Geophysical Journal International*, **182**(2), 583–598.

Kirby, J. & Swain, C., 2011. Improving the spatial resolution of effective elastic thickness estimation with the fan wavelet transform, *Computers & Geosciences*, **37**(9), 1345–1354.

Kirby, J. F., 2014. Estimation of the effective elastic thickness of the lithosphere using inverse spectral methods: The state of the art, *Tectonophysics*.

Korevaar, J., 1968. *Mathematical methods*, Academic Press, New York.

Lambeck, K. & Nakiboglu, S. M., 1980. Seamount loading and stress in the ocean lithosphere, *Journal of Geophysical Research*, **85**(B11), 6403.

Levitt, D. A. & Sandwell, D. T., 1995. Lithospheric bending at subduction zones based on depth soundings and satellite gravity, *Journal of Geophysical Research*, **100**(B1), 379.

Lobkovsky, L. I. & Sorokhtin, O. G., 1976. Plastic deformation of oceanic lithosphere in a subduction zone, *Tectonics of Lithospheric Plates*, pp. 22–52.

Luttrell, K. & Sandwell, D., 2012. Constraints on 3-d stress in the crust from support of mid-ocean ridge topography, *Journal of Geophysical Research*, **117**(B4).

Manriquez, P., Contreras-Reyes, E., & Osses, A., 2014. Lithospheric 3-d flexure modelling of the oceanic plate seaward of the trench using variable elastic thickness, *Geophysical Journal International*, **196**(2), 681–693.

Massell, C. G., 2002. *Large-scale structural variation of trench outer slopes and rises*, Ph.D. thesis, University of California, San Diego.

McNutt, M. K. & Menard, H. W., 1982. Constraints on yield strength in the oceanic lithosphere derived from observations of flexure, *Geophysical Journal International*, **71**(2), 363–394.

Melosh, H. J., 1978. Dynamic support of the outer rise, *Geophysical Research Letters*, **5**(5), 321–324.

Müller, R. D., Sdrolias, M., Gaina, C., & Roest, W. R., 2008. Age, spreading rates, and spreading asymmetry of the world's ocean crust, *Geochemistry, Geophysics, Geosystems*, **9**(4).

Parsons, B. & Molnar, P., 1976. The origin of outer topographic rises associated with trenches, *Geophysical Journal International*, **1**(4), 707–712.

Parsons, B. & Sclater, J. G., 1977. An analysis of the variation of ocean floor bathymetry and heat flow with age, *Journal of Geophysical Research*, **82**(5), 803–827.

Perez-Gussinye, M., Swain, C. J., Kirby, J. F., & Lowry, A. R., 2009. Spatial variations of the effective elastic thickness, te, using multitaper spectral estimation and wavelet methods: Examples from synthetic data and application to south america, *Geochemistry, Geophysics, Geosystems*, **10**(4), n/a–n/a.

Ranero, C. R., Phipps Morgan, J., McIntosh, K., & Reichert, C., 2003. Bending-related faulting and mantle serpentinization at the middle america trench, *Nature*, **425**(6956), 367–373.

Sandwell, D. & Schubert, G., 1982. Lithospheric flexure at fracture zones, *Journal of Geophysical Research*, **87**(B6), 4657.

Sandwell, D., Garcia, E., Soofi, K., Wessel, P., Chandler, M., & Smith, W. H. F., 2013. Toward 1-mGal accuracy in global marine gravity from CryoSat-2, envisat, and jason-1, *The Leading Edge*, **32**(8), 892–899.

Sandwell, D. T., 1984. Thermomechanical evolution of oceanic fracture zones, *Journal of Geophysical Research*, **89**(B13), 11401.

Smith, W. H. & Sandwell, D. T., 1997. Global sea floor topography from satellite altimetry and ship depth soundings, *Science*, **277**(5334), 1956–1962.

Tanimoto, T., 1998. State of stress within a bending spherical shell and its implications for subducting lithosphere, *Geophysical Journal International*, **134**(1), 199–206.

Trefethen, L. N., 2000. *Spectral methods in MATLAB*, Software, environments, tools, Society for Industrial and Applied Mathematics, Philadelphia, PA.

Turcotte, D., McAdoo, D., & Caldwell, J., 1978. An elastic-perfectly plastic analysis of the bending of the lithosphere at a trench, *Tectonophysics*, **47**(3-4), 193–205.

Turcotte, D. L. & Schubert, G., 2002. *Geodynamics*, Cambridge University Press, Cambridge ; New York, 2nd edn.

van Wees, J. D. & Cloetingh, S., 1994. A finite-difference technique to incorporate spatial variations in rigidity and planar faults into 3-d models for lithospheric flexure, *Geophysical Journal International*, **117**(1), 179–195.

Watts, A. B., 2001. *Isostasy and flexure of the lithosphere*, Cambridge University Press, Cambridge ; New York.

Watts, A. B. & Talwani, M., 1974. Gravity anomalies seaward of deep-sea trenches and their tectonic implications, *Geophysical Journal International*, **36**(1), 57–90.

Wessel, P., 1996. Analytical solutions for 3-d flexural deformation of semi-infinite elastic plates, *Geophysical Journal International*, **124**(3), 907–918.

Chapter 4

Outer Trench Slope Flexure and Faulting at Pacific Basin Subduction Zones

Abstract

We generate model bathymetry and free-air gravity grids for the seafloor seaward of subduction zones that capture the broad trends of deformation due to lithospheric flexure. By using a thin elastic plate formulation with rigidity variations along both horizontal dimensions and which accounts for the effects of plastic yielding, our models are able to reproduce the observed rapid change in curvature at the outer trench wall. Forward models for flexural deflection and plate rigidity are fitted to satellite altimetry-derived marine gravity anomalies jointly with shipboard sonar soundings and swath bathymetry data sets. The estimated parameters are the applied vertical shear and bending moment at the trench axis, and the data misfits are minimized with respect to the L1-norm subject to constraints on the variation of the load parameters along the strike of the trench. We perform pre-processing of the input data to enhance the recovery of the flexural signal. Short-wavelength features such as seamounts are isolated using a directional median filter and then excluded from the parameter estimation process.

Our preliminary results from several examples show that the plate rigidity progressively decreases with increasing proximity to the trench axis. These zones of plate weakening correspond to the occurrence of trench-parallel seafloor fractures at the outer trench wall as seen in high-resolution bathymetry data. We seek to determine whether a correlation exists between the distribution or morphology of these fractures and the amount or trend in the reduction of plate rigidity for outer rise regions across the Pacific.

4.1 Introduction

Subduction zones provide a natural laboratory for estimating the strength and thickness of the oceanic lithosphere. The bending moment from the negatively buoyant slab, combined with the downward force of the overriding plate, are balanced by trench and outer rise topography (Turcotte & Schubert, 2014). Simple thin elastic plate flexure models provide a remarkably good fit to bathymetry and gravity data outboard of the trench axis (Caldwell et al., 1976). In addition, simple models of the cooling of the lithospheric with age provide a remarkably accurate description of the increase in seafloor depth with age (Parsons & Sclater, 1977). Assuming the upper part of the lithosphere behaves elastically for temperatures less than $\sim$ 600 $^\circ$ C, the combination of the cooling and flexure models predicts that the elastic thickness, and thus flexural wavelength, of the lithosphere should depend on the age of the lithosphere. This elastic thickness versus age relationship has been adequately confirmed for moderate-sized seamounts (Watts, 2001) but fails for flexures at subduction zones (Wessel, 1992; Levitt & Sandwell, 1995; Bry & White, 2007). The breakdown of this relationship is due to the inelastic deformation in lithosphere that is bent well beyond its elastic limit (Wessel, 1992). The thin elastic plate flexure theory is accurate when the curvature of the flexed plate is small (˜10-8). However as the curvature is increased the upper part of the plate yields by sliding on optimally oriented faults while the lower part of the plate yields by plastic or ductile flow processes (Goetze & Evans, 1979; Mueller & Phillips, 1995). At low curvatures there is a linear relationship between applied

bending moment and curvature where the ratio is the flexural rigidity - related to the cube of the elastic thickness. However at high curvatures the non-linear processes dominate and eventually the moment saturates. As the bending approaches moment saturation, the ratio of moment to curvature drops far below the initial elastic value and the elastic plate appears thinner (i.e. effective elastic thickness). McNutt & Menard (1982) developed a method for correcting the effective elastic thickness back to the true mechanical thickness using the measurements of maximum plate curvature combined with a model for the yield strength versus depth. While this approach can be accurate for plates bent at moderate curvatures $\sim 10^{-7}$, it provides inaccurate results for plates bent at high curvatures (Mueller & Phillips, 1995). Moreover bathymetric fractures on the outer trench walls of subduction zones may result in inaccurate estimates of curvature depending on the filtering technique applied (Craig et al., 2014; Craig & Copley, 2014). The combined effect is that converting effective elastic thickness to mechanical thickness may be in error by a factor of 2 or more (Levitt & Sandwell, 1995). This may explain why elastic thickness estimates from flexure models of trenches show little or no increase with age.

Of course the lithosphere is bent well beyond its elastic limit at all subduction zones since the subducted part of the plate is permanently deflected away from the horizontal as it founders in the mantle. In this study we will focus on the end-member case where the lithosphere is approaching moment saturation at the trench axis. As shown in Mueller & Phillips (1995), the saturation bending moment increases almost linearly with increasing seafloor age for the half-space cooling model and shows some flattening at ages greater than about 70 Ma for the plate cooling model (Levitt & Sandwell, 1995). Therefore accurate estimates of bending moment at the deepest part of each trench can be used to calibrate the temperature-dependent yield strength envelope models.

Rather than measure the characteristic wavelength and curvature of the flexure, we propose that the moment of the flexure is the important parameter. Here we perform a circum-Pacific analysis of bathymetry and gravity outboard of trenches having a variety of cooling ages to estimate the saturation moment as

well as the depth and heave of the outer trench wall fractures. We use a thin-plate flexure that can simulate trenches having curved planform (Garcia et al., 2015). In addition the model has a full non-linear relationship between moment and curvature according to a prescribed yield strength envelope (YSE, e.g., Goetze & Evans, 1979). The new aspect of this analysis is that an iterative approach is employed to fit the non-uniform distribution of bathymetry and gravity data. The model has spatially variable applied bending moment and downward force along the curved trench axis (Figure 4.1). The starting model has an age-dependent flexural rigidity and a set of moment and load parameters is estimated. The curvature of the flexed plate is used to refine the spatially-variable rigidity and the least squares problem is re-solved until convergence is reached. The final model provides estimates of the moment at the trench axis, the depth of the fracturing of the upper part of the plate, and the overall strain in the uppermost part of the plate that can be related to the surface faulting. The main questions we will consider in this study are:

- Are any of the incoming plates at subduction zones moment saturated?

- Is an age-dependent YSE model consistent with the observations?

- What brittle, ductile, and thermal models are most consistent with the observations?

- What is the predicted magnitude and depth of outer trench wall fractures?

- Is this consistent with high-resolution seafloor depth observations?

- What are the implications in terms of the roughness and permeability of the downgoing plate?

Our analysis is similar to the global compilation by Levitt & Sandwell (1995) and more recently Bry & White (2007) with three significant differences. Those studies used constant-rigidity thin plate flexure to model gravity and topography profiles. The Levitt & Sandwell (1995) study limited the bathymetry to actual soundings while the Bry & White (2007) used actual soundings averaged over

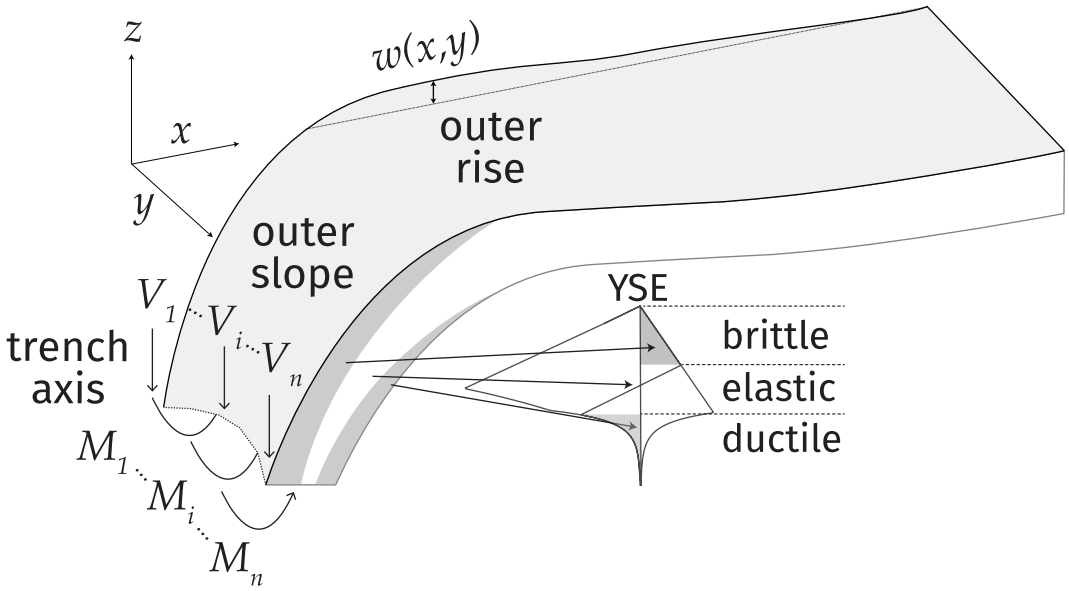

Figure 4.1: Thin elastic plate bent downward by moments and vertical loads acting along curved segments ($\sim$ 50 km long). The strength of each segment is adjusted so the model topography and gravity outboard of the trench match observations. The planform of the trench is digitized from (Bassett & Watts, 2015a,b). The plate has a non-linear moment curvature relation provided by a YSE model. The non-linear differential equation is solved using an iterative spectral method (Garcia et al., 2015)

segments outboard of the trench. Here we use a refined gravity model (Sandwell et al., 2014) and actual ship soundings that were recently updated (Olson et al., 2014). Moreover, rather than using only profiles that are nearly perpendicular to the trench, which greatly limit the areas to be modeled (Levitt & Sandwell, 1995), we developed a flexural surface model defined over two horizontal dimensions to account for the actual 2-D geometry of the trench in mapview. Therefore, soundings from ship tracks could be used whether the tracks are perpendicular or parallel to the trench axis planform, as long as the aggregate bathymetry samples a distribution of locations both adjacent and away from the trench. This can have an important effect where the planform of the trench is sharply curved (Manriquez et al., 2014). Most importantly, our model uses a full non-linear relationship between bending moment and curvature for a given YSE. Contreas-Reyas and Osses [2010] and Manriquez et al. (2014) performed similar regional analyses using a stair-step or full YSE rheology, respectively but they were primarily interested in visual fits for forward models and did not investigate trenches globally over a wide range of tectonic environments.

4.2 Flexure Modeling Approach

4.2.1 Physical Model

The physical model consists of a thin elastic plate of variable flexural rigidity $D(x, y)$ floating on a fluid substrate. The plate and substrate have the same density ρ_m. The plate is overlain by ocean having density of ρ_w. The differential equation describing the deflection of the plate $w(x, y)$ in response to a spatially variable vertical load $p(x, y)$ is given by

$$\nabla^2 \left[D \nabla^2 w \right] - (1 - \nu) \left[\frac{\partial^2 D}{\partial x^2} \frac{\partial^2 w}{\partial y^2} - 2 \frac{\partial^2 D}{\partial x \partial y} \frac{\partial^2 w}{\partial x \partial y} + \frac{\partial^2 D}{\partial y^2} \frac{\partial^2 w}{\partial x^2} \right] - N_x \frac{\partial^2 w}{\partial x^2} - 2 N_{xy} \frac{\partial^2 w}{\partial x \partial y} - N_y \frac{\partial^2 w}{\partial y^2} + (\rho_w - \rho_m) g w = p(x, y) \tag{4.1}$$

where g is the acceleration of gravity and N_x, N_{xy}, and N_y is the in-plane force. We solve the equation using an iterative spectral method where the model domain is much larger than the size of vertical load. The boundary conditions are such that the plate deflection and its derivatives vanish far from the load.

Bending moments and vertical loads are applied along finite-length curved segments as shown in Figure 4.1. The moment is approximated as a force couple of equal and opposing vertical loads following the numerical method described in Garcia et al. (2015). In addition to calculating the deflection of the plate, the gravity anomaly is calculated by upward continuation of the seafloor gravity to the ocean surface using the mean depth in the region. Each segment serves as a Green's function for the model inversion. The regional trench model consists of multiple segments placed end-to-end following the planform of the actual trench. Assume for the moment that we had correct values for the strength of the moments and vertical loads along the 12 segments. We begin the solution by constructing a spatially variable rigidity using the age (Müller et al., 2008) of the lithosphere outboard of the trench and a YSE model. A uniform age value of 1 Ma is used inboard of the trench to provide complete spatial definition of rigidity needed for the solver. Using the approach of Garcia et al. (2015) we solve for the plate deflection, gravity anomaly, and plate curvature for this initial guess at rigidity. We then use the curvature grid to re-estimate the spatial variations in rigidity again using the YSE formulation. We iterate until convergence of the solution for the deflection of the plate (Burov & Diament, 1995), which is normally reached after 5-10 iterations. This analysis provides linearized Green's functions for each of the segments. These Green's functions are used in the inversion to update the estimates of the moments and vertical loads along the segments. Curvature from the updated solution us used to re-estimate the spatial variations in rigidity and a second set of Green's functions is constructed. This outer loop generally converges after 3-5 iterations.

4.2.2 Data Preparation

The inversion for the moments, vertical loads and outer trench wall deformation is performed by minimizing the misfit between the model bathymetry/gravity. There are 4 types of data that go into this analysis. The coordinates of the trench planform are determined using the deepest points along the trench from Bassett & Watts (2015a,b), which are then divided into segments of a set length. The segments for two example areas are shown as alternating red and yellow lines in Figure 2. The age of the lithosphere for the region is based on the analysis of Müller et al. (2008) and, as described above, lithoshere inboard of the trench is set to a low age of 1 Ma. Seafloor depth is based on a recent global compilation at 500 m resolution (Olson et al., 2014) and gravity is based on a recent analysis by Sandwell et al. (2014).

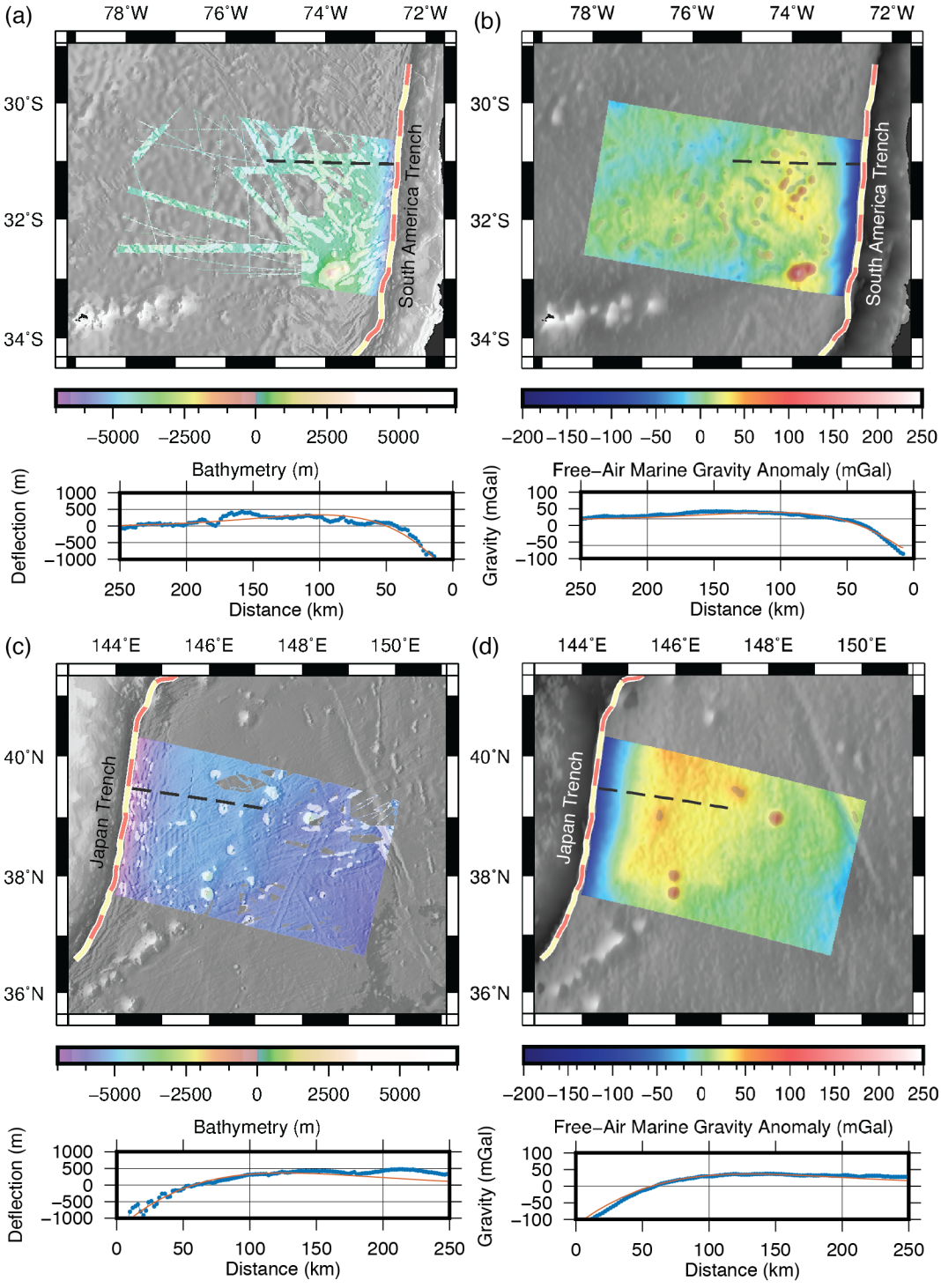
(a)
78˚W
76˚W
74˚W
72˚W
30˚S
32˚S
34˚S
South America Trench
−5000 −2500 0 2500 5000
Bathymetry (m)
Deflection (m)
1000
500
0
−500
−1000
250 200 150 100 50 0
Distance (km)
(b)
78˚W
76˚W
74˚W
72˚W
30˚S
32˚S
34˚S
South America Trench
−200 −150 −100 −50 0 50 100 150 200 250
Free−Air Marine Gravity Anomaly (mGal)
Gravity (mGal)
100
50
0
−50
−100
250 200 150 100 50 0
Distance (km)
(c)
144˚E
146˚E
148˚E
150˚E
40˚N
38˚N
36˚N
Japan Trench
−5000 −2500 0 2500 5000
Bathymetry (m)
Deflection (m)
1000
500
0
−500
−1000
0 50 100 150 200 250
Distance (km)
(d)
144˚E
146˚E
148˚E
150˚E
40˚N
38˚N
36˚N
Japan Trench
−200 −150 −100 −50 0 50 100 150 200 250
Free−Air Marine Gravity Anomaly (mGal)
Gravity (mGal)
100
50
0
−50
−100
0 50 100 150 200 250
Distance (km)

Figure 4.2 *(previous page)*: The colored regions in the maps are where data is compared with model quantities, while smaller shaded areas within show data that has been filtered out (see text). The segments along the trench with alternating color patterns represent the free parameters of bending moment and vertical load. Profiles of model fits for each case are also shown, with blue points for the data and an orange line for the model. The sampling tracks are displayed as a dashed line in each map. (a) Seafloor depth for a portion of the South America Trench offshore Chile. (b) Marine gravity offshore Chile (c) Bathymetry offshore Japan (d) Marine gravity offshore Japan.

The features of our model setup which are selected by the user include the individual length of the trench segments, the along-trench extent to be considered for load estimation, and the area of the observations to be included in the parameter estimation process [Figure 2]. For this work, we chose to divide the trench axis into 50-km long trench segments, and estimate the loads for 600-km long regions in the along-trench direction. From the center of this entire model region we measure a 300-km long subregion along the trench axis and only include data that are approximately 600 km seaward of this smaller subregion. This seaward and trench-perpendicular extent of the data is similar to the profile lengths used in previous studies (Levitt & Sandwell, 1995; Caldwell et al., 1976). Meanwhile, the inter-model spacing was chosen to be comparable to the 300-km length of the model region so there is sufficient overlap from adjacent models.

Outlier gravity and bathymetry data are edited prior to inverting for the flexural parameters. As a first step we make a long-wavelength slope correction to the bathymetry based on the expected seafloor subsidence due to lithosphere cooling with age (Hillier & Watts, 2005). Another correction that varies slowly across large spatial scales is that due to sediment loading, which we also apply to the sounding data (Divins, 2003; Whittaker et al., 2013). Short-wavelength features in both the bathymetry and gravity which we do not wish our models to fit include small seamounts, fracture zone scarps, and even bending-related faults.

While there are methods for isolating this non-flexural topography (Zhang et al., 2014) that take into account variations in crustal thickness, and these may also be extracted through expert interpretation (Crosby & McKenzie, 2009), we instead separate the regional and local signals using a directional median filter (Kim & Wessel, 2008) (Figure 4.2). Before being used as input in the parameter estimation procedure, the residual local signal is separated from the regional trends in both the bathymetry and gravity data and are then given lower weights to decrease their effect on the final model fits. The advantage of adopting anisotropic filtering over similar methods that separate local scale topography from regional swells is that it provides consistent performance in feature detection with minimal user supervision.

4.2.3 Estimating Model Parameters

We solve a parameter estimation problem for the values of bending moment and vertical shear at the trench axis (Figure 4.1) using a 1-norm minimization. For every i-th trench segment, we solve for a downward vertical load V_i and a bending moment M_i that is applied perpendicular to that segment. In addition we impose a smoothness constraint to minimize the difference in moment and downward force between adjacent segments. The 1-norm minimization is

$$\min \left\{ \|\mathbf{Am} - \mathbf{b}\|^1 + \alpha \|\mathbf{Sm}\|^1 \right\} \tag{4.2}$$

where $\mathbf{m}$ is a vector of model parameters, $\mathbf{A}$ is the design matrix, $\mathbf{b}$ is a vector of data constraints, $\mathbf{S}$ is the smoothing matrix and α is the relative weight given to the smoothing parameter. We set up a system of linear equations to jointly satisfy the relations $\mathbf{Am} = \mathbf{b}$ and $\mathbf{Sm} = \mathbf{0}$. These equations can be expressed in matrix form as,

$$\begin{bmatrix} \boldsymbol{\Gamma}_{\hat{w}}\mathbf{G}_w(M) & \boldsymbol{\Gamma}_{\hat{w}}\mathbf{G}_w(V) & \boldsymbol{\Gamma}_{\hat{w}} & \mathbf{0} \\ \lambda\boldsymbol{\Gamma}_{\Delta\hat{g}}\mathbf{G}_{\boldsymbol{\Delta}\mathbf{g},\mathbf{M}} & \lambda\boldsymbol{\Gamma}_{\Delta\hat{g}}\mathbf{G}_{\boldsymbol{\Delta}\mathbf{g},\mathbf{V}} & \mathbf{0} & \lambda\boldsymbol{\Gamma}_{\Delta\hat{g}} \\ \alpha_M\mathbf{D} & \mathbf{0} & \mathbf{0} & \mathbf{0} \\ \mathbf{0} & \alpha_V\mathbf{D} & \mathbf{0} & \mathbf{0} \end{bmatrix} \begin{bmatrix} \mathbf{m}_M \\ \mathbf{m}_V \\ w_0 \\ \Delta g_0 \end{bmatrix} = \begin{bmatrix} \boldsymbol{\Gamma}_{\hat{w}}\hat{\mathbf{w}} \\ \boldsymbol{\Gamma}_{\Delta\hat{g}}\boldsymbol{\Delta}\hat{\mathbf{g}} \\ \mathbf{0} \\ \mathbf{0} \end{bmatrix} \tag{4.3}$$

On the left-hand side of equation (4.3), the Greens's functions $\mathbf{G}$ are calculated for the plate deflection w and gravity anomaly Δg that correspond to the model plate's flexural response to a unit bending moments M and vertical load V at the i-th model trench segment. The data vector $\mathbf{b}$ consists of subvectors for the processed bathymetry $\hat{w}$ and marine gravity anomaly Δg. The components of the model vector represent the estimated values of the applied loads at the N trench segments:

$$\mathbf{m}_M = [M_1, M_2, \cdots M_n]^T \tag{4.4}$$

$$\mathbf{m}_V = [V_1, V_2, \cdots V_n]^T \tag{4.5}$$

Along with these main flexural loading parameters, we also estimate an unknown offset w_0 between the processed bathymetry data and the model deflection surface, which is calculated in reference to an undeformed depth. The offset Δg_0 saves the same purpose for gravity anomalies.

On the right-hand side of equation (4.3), the input data are comprised of independent sets of shipboard soundings and satellite altimetry-derived gravity anomalies. The observations to be compared with the model predictions are the processed bathymetry and marine gravity anomaly data, which are represented in the sub-vectors $\hat{\mathbf{w}}$ and $\boldsymbol{\Delta}\hat{\mathbf{g}}$, respectively. The elements of these sub-vectors are assigned individual weights based on distance from the trench (Levitt & Sandwell, 1995; Emry et al., 2014) and the results of the directional median filtering algorithm (Kim & Wessel, 2008) to remove small-scale anomalous topography. These weights are expressed as the following diagonal matrices:

$$\boldsymbol{\Gamma}_{\hat{w}} = [\Gamma_{\hat{w},1}, \Gamma_{\hat{w},2}, \cdots \Gamma_{\hat{w},q}]^T \tag{4.6}$$

$$\boldsymbol{\Gamma}_{\boldsymbol{\Delta}\hat{\mathbf{g}}} = [\Gamma_{\Delta\hat{g},1}, \Gamma_{\Delta\hat{g},2}, \cdots \Gamma_{\Delta\hat{g},r}]^T \tag{4.7}$$

The smoothness constraint imposed on $\mathbf{m}_M$ and $\mathbf{m}_M$ separately may be adjusted independently through the choice of (α_M) and (α_V) values. The first-difference $\mathbf{D}$ operator is just

$$\mathbf{D} = \begin{bmatrix} 1 & -1 & 0 & \cdots & \cdots & 0 \\ 0 & 1 & -1 & 0 & \cdots & \vdots \\ \vdots & \ddots & \ddots & \ddots & \vdots & \vdots \\ \vdots & \vdots & \ddots & \ddots & \ddots & 0 \\ \vdots & \vdots & \cdots & 0 & 1 & -1 \end{bmatrix} \tag{4.8}$$

As for the smoothing parameters, we prescribe a minimum value of *alpha* such that all vertical shear loading values estimated at the trench are applied in the downward sense, and all the bending moments have the same sign. Meanwhile, an upper bound on *alpha* would result in all segments having the same direction and magnitude of loading parameters – an over-smoothed model.

We can define a joint misfit function ψ for bathymetry and gravity as follows:

$$\psi = \frac{1}{1+\tilde{\lambda}} \left\{ \sum_{i=1}^{q} \left| \frac{\xi_{w_i}}{\zeta_w} \right| + \tilde{\lambda} \sum_{j=1}^{r} \left| \frac{\xi_{\Delta g_j}}{\zeta_{\Delta g}} \right| \right\} \tag{4.9}$$

which is similar to the misfit criterion used in Levitt & Sandwell (1995). The residuals ξ at each model and data grid point (x, y) are computed using

$$\begin{aligned} \xi_{w_i} &= \Gamma_{w_i}\{w(x_i, y_i) - \hat{w}_i\} \\ &= \frac{1}{\Gamma_{w_i}} \left\{ \left[\sum_{k=1}^{n} \left(M_k G_{w,i}(M_k) + V_k G_{w,i}(V_k) \right) + w_0 \right] - \hat{w}_i \right\} \end{aligned} \tag{4.10}$$

$$\begin{aligned} \xi_{\Delta g_j} &= \frac{1}{\Gamma_{\Delta g_j}}\{\Delta g(x_j, y_j) - \Delta \hat{g}_j\} \\ &= \Gamma_{\Delta g_j} \left\{ \left[\sum_{k=1}^{n} \left(M_k G_{\Delta g_j}(M_k) + V_k G_{\Delta g_j}(V_k) \right) + \Delta g_0 \right] - \Delta \hat{g}_j \right\} \end{aligned} \tag{4.11}$$

The residuals are divided by the total absolute deviations ζ of each set of observations from the estimated offsets,

$$\zeta_{\Delta h} = \sum_{i=1}^{q} \Gamma_{w_i} \left| \hat{w}_i - w_0 \right| \tag{4.12}$$

$$\zeta_{\Delta g} = \sum_{j=1}^{r} \Gamma_{\Delta g_j} \left| \Delta \hat{g}_j - \Delta g_0 \right| \tag{4.13}$$

and so the misfit measure is an indicator of how much of an improvement over a constant plane the model deflection surface provides in terms of fitting the data. A weighting parameter $\tilde{\lambda}$ controls the relative importance of the gravity to the bathymetry. Note that increasing $\tilde{\lambda}$ would tend to improve the model fits to gravity at the expense of the bathymetry residuals. For most cases the lowest misfit values occur when $\tilde{\lambda}$ is between 0.1 and 1. Following Levitt & Sandwell (1995) we set $\tilde{\lambda}$=0.4 for our suite of models.

The rigidity grid for each of our thin elastic plate models is estimated using a nonlinear moment-curvature relation that assumes a brittle-elastic-plastic rheology for the oceanic lithosphere (Figure 4.3). In this yield strength envelope formulation (Goetze & Evans, 1979; McNutt & Menard, 1982), the differential stress in the upper portion of our lithosphere is assumed to be limited by brittle yielding. At greater depths, brittle failure transitions into ductile yielding. Moreover, the ductile behavior is separated into regimes of low and high-temperature plasticity. In the middle of the plate where the stresses do not reach these brittle and ductile yielding values, the plate continues to behave elastically and the stresses increase linearly away from the nodal plane with a gradient equal to the plate curvature. Note that unlike the case for flexure profile modeling, the horizontal grid dimensions in our models may not necessarily be aligned to two of the principal stress axes, which is the implicit assumption when dealing with profiles which have only one horizontal dimension. Strictly speaking, a coordinate transformation should be applied so that the curvatures from the model grid can be put into the expressions for differential stress.

For the portion of the YSE describing brittle behavior, a frictional failure criterion based on rock deformation experiments (Byerlee, 1978) is imposed in the strong rheology case (f =0.85 in shallow regions, transitioning to $f = 0.6$ at depth),

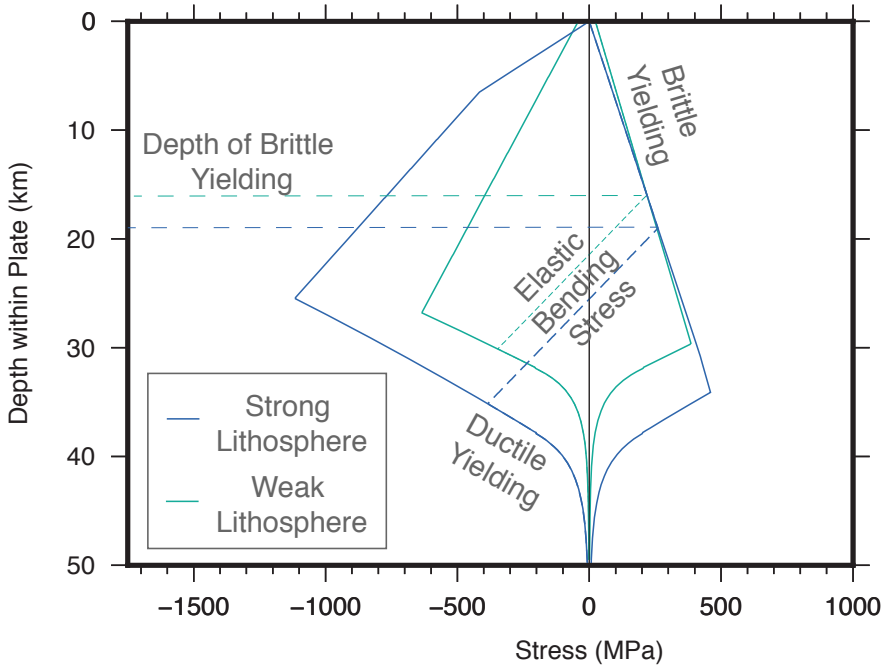

Figure 4.3: Yield strength versus depth for two thermal models representing cold (Parsons & Sclater, 1977) and hot (Hasterok, 2013) geotherms. The two models also have different static coefficient of friction (0.85 and 0.3, respectively) and levels of pore pressure (fully hydrostatic and no pore pressure) that affect the yield strength of the upper lithosphere. For the yield strength of the lower lithosphere, the strong and weak lithosphere models both correspond to a form of the high-temperature ductile flow (Goetze & Evans, 1979; Wessel, 1992) with a value for activation energy that is appropriate for wet dunite. This example shows yielding from a moderate curvature of 5×10^{-7} and age of 70 Ma. The depth of brittle yielding is at the intersection of the elastic stress and the brittle yielding curve.

while a low coefficient of friction (f =0.3)(f =0.3, Craig et al., 2014) is set in the weak lithosphere scenario. The high-temperature ductile flow law is in the standard form and uses a lower value for the activation energy that lies within the range of experimental values for wet olivine (Hirth & Kohlstedt, 2003). The magnitude of the ductile yielding stresses resulting from these flow laws is dependent on the geotherm, and for the strong and weak lithosphere models we compare the plate cooling model of Parsons & Sclater (1977) with that of Hasterok (2013), which is based on a more recent global compilation of heat flow measurements.

4.3 Results

The initial inversions using the strong lithosphere rheology (Figure 4.3) provided poor fits to the gravity and bathymetry data. In general the model underestimated the topography/gravity of the outer rise and also overestimated the depth and gravity on the of the trench and outer trench wall (Figure 4.4b, 4.5b). The plate was too strong to approach moment saturation and thus had a thick elastic core on the outer trench wall. Previous studies using constant rigidity elastic plates simply reduced the plate thickness until a good match was achieved (e.g., Levitt & Sandwell, 1995). In this formulation we achieved generally good fits by increasing the temperature of the lithosphere by replacing the Parsons & Sclater (1977) Parsons and Sclater cooling model with the Hasterok (2013) plate cooling model. This provided some weakening of the lower lithosphere but was still insufficient to achieve the large curvatures observed on the outer trench wall, which can be as high as around 1.0×10^{-6}/m based on analysis of bathymetry (Craig et al., 2014). Following Craig et al. (2014) we also adopted parameter values for a brittle rheology that was weaker than the Byerlee (1978) empirical relations.

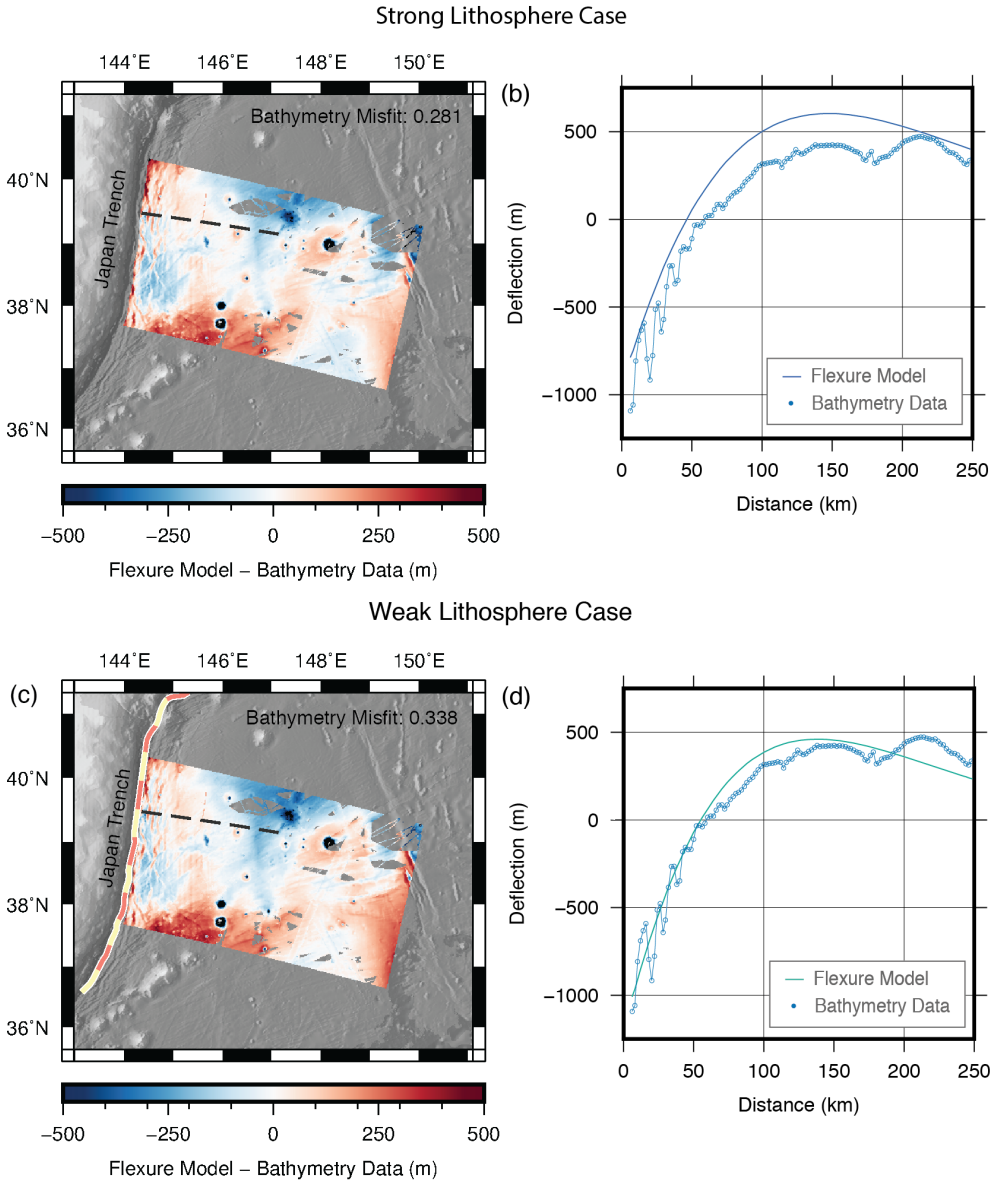
Strong Lithosphere Case
144˚E
146˚E
148˚E
150˚E
40˚N
38˚N
36˚N
Bathymetry Misfit: 0.281
Japan Trench
−500
−250
0
250
500
Flexure Model – Bathymetry Data (m)
(b)
Deflection (m)
500
0
−500
−1000
Flexure Model
Bathymetry Data
0
50
100
150
200
250
Distance (km)
Weak Lithosphere Case
(c)
Bathymetry Misfit: 0.338
(d)

Figure 4.4 *(previous page)*: The residuals between the model flexural deflection and the processed bathymetry data, and cases are shown for two different rheologies: a strong lithosphere and a weak lithosphere YSE (see text). Profiles of model fits for each case are also shown, with blue points for the data and an orange line for the model. The sampling tracks are displayed as a dashed line in each map. (a) Residuals for a portion of the Japan Trench offshore NE Honshu using a model with a strong lithosphere (map view). (b) Bathymetry profile and model deflection for a strong lithosphere (c) Residuals for a weak lithosphere model (d) Weak lithosphere model fit (profile view for a track).

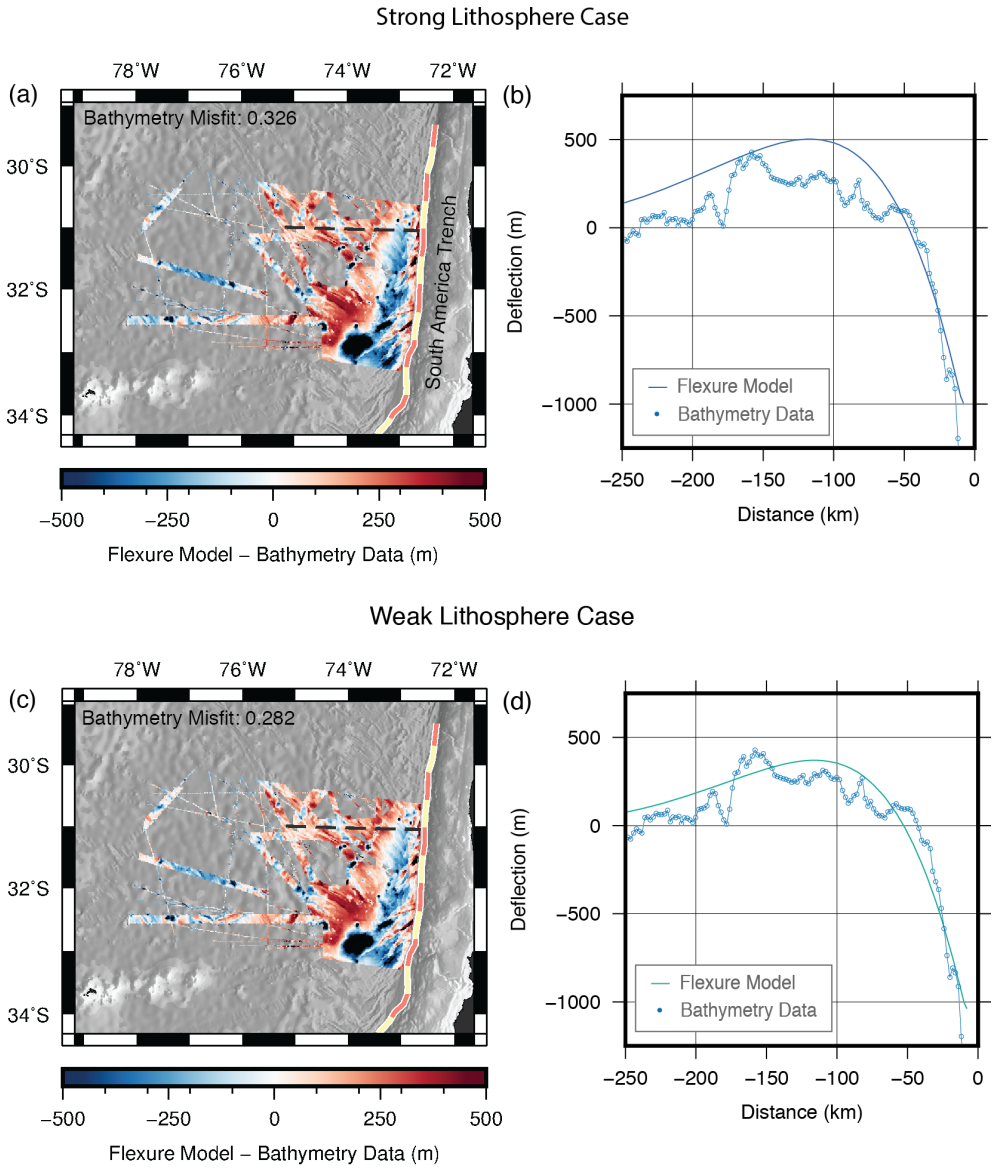
Strong Lithosphere Case
(a)
78˚W
76˚W
74˚W
72˚W
30˚S
32˚S
34˚S
Bathymetry Misfit: 0.326
South America Trench
−500
−250
0
250
500
Flexure Model – Bathymetry Data (m)
(b)
Deflection (m)
500
0
−500
−1000
Flexure Model
Bathymetry Data
−250
−200
−150
−100
−50
0
Distance (km)
Weak Lithosphere Case
(c)
78˚W
76˚W
74˚W
72˚W
30˚S
32˚S
34˚S
Bathymetry Misfit: 0.282
−500
−250
0
250
500
Flexure Model – Bathymetry Data (m)
(d)
Deflection (m)
500
0
−500
−1000
Flexure Model
Bathymetry Data
−250
−200
−150
−100
−50
0
Distance (km)

Figure 4.5 *(previous page)*: The residuals between the model flexural deflection and the processed bathymetry data, and cases are shown for two different rheologies: a strong lithosphere and a weak lithosphere YSE (see text). Profiles of model fits for each case are also shown, with blue points for the data and an orange line for the model. The sampling tracks are displayed as a dashed line in each map. (a) Residuals for a portion of the South America Trench offshore Chile using a model with a strong lithosphere (map view). (b) Bathymetry profile and model deflection for a strong lithosphere (c) Residuals for a weak lithosphere model (d) Weak lithosphere model fit (profile view for a track).

The results for all the model trench regions are summarized in Table 4.1. The first column contains the names for the model regions following the convention of Wu et al. (2008), and the second and third columns list the coordinates of the midpoint along the model trench segments in that region. These are followed by the average seafloor age (Müller et al., 2008) along the trench outer slope as sampled from the model grid locations. The misfit values for the bathymetry and gravity data are also included. In general these values are less than 0.5, indicating that the flexure models perform at least 50% better than a flat plane in fitting either the bathymetry or gravity observations. Examples of these residuals are shown in Figures 4.4 and 4.5.

We now proceed to compiling our model results to make inferences about the mechanical properties of incoming lithosphere at circum-Pacific subduction zones. Figure 4.7a plots the average bending moment calculated at the trench outer slope (just slightly seaward of the trench on the subducting plate) against age (note that these values are given in Table 4.1). We then compare it to the values of the saturation moment computed for every age, which we calculated by finding the limit of the nonlinear moment-curvature relation for the specified YSE at high curvature. Within the formulation of our model, this saturation moment serves as a strict upper bound for the values of moment that the plate can support. Our results show that young lithosphere (< 70 Ma) is nearly moment saturated

at the trench outer slope, while old lithosphere (< 70 Ma) is at least 2/3 moment saturated.

A plot of model seafloor depth at zero deflection in the center of each subregion versus age is shown in Figure 4.7. Also shown is the depth-age relation predicted by the Hasterok (2013) and Parsons & Sclater (1977) thermal models, as well as the empirically-derived relation by Hillier & Watts (2005). In the case of young lithosphere the Hasterok (2013) and Parsons & Sclater (1977) seem to bracket our model results, with the seafloor subsidence of Hillier & Watts (2005) giving the closest fit. Meanwhile, any such correspondence is less clear for older lithosphere, and some of the observed depths much are greater than the model depths. There are at least two possible explanations for this: the Hasterok (2013) model might be generating warmer lithosphere than required to match the observed subdsidence, or that the net downward V forces increase average depth close to the trench. Another possibility we have yet to explore further is how subtle tilts across both longitude and latitude are affecting our depth estimates. Unlike in Bry & White (2007) or Levitt & Sandwell (1995) we did not include an unknown slope in the bathymetry or gravity observations as a free parameter in our modeling approach, and there might be small some trade-off between a plane tilt and the average depth offset.

Table 4.1: Model Results Summary

Model Name	Midpoint along Trench		Seafloor Age	Misfit Measure		Bending Moment M	Deflection Curvature κ	Elastic Thickness T_e	Depth Offset w_0
	Lon	Lat	(Ma)	w	Δg	joint (ψ)	(10^{16} Nm)	(10^{-7}/m)	(km)
COS1	-94.08	14.12	24.81	0.25	0.38	1.28	7.94	13.48	4.45
COS2	-92.06	13.05	24.56	0.25	0.39	1.31	11.72	12.00	4.34
COS3	-90.04	12.19	24.93	0.33	0.34	1.36	13.09	11.58	4.31
COS4	-87.00	10.40	23.82	0.44	0.37	1.25	10.16	12.25	4.37
COS5	-88.06	11.29	24.93	0.35	0.43	1.35	13.08	11.63	4.33
PER3	-81.66	-7.01	29.48	0.17	0.31	1.43	3.48	18.42	4.77
PER4	-80.80	-9.06	32.12	0.22	0.23	1.24	1.68	23.61	4.78
PER5	-79.67	-11.09	41.44	0.20	0.30	2.17	2.83	22.59	4.99
PER6	-78.37	-13.05	42.96	0.29	0.44	2.31	3.09	22.44	5.00
NCH1	-74.19	-17.10	47.67	0.21	0.41	2.95	6.36	19.11	5.17
NCH2	-72.05	-19.05	53.28	0.30	0.43	3.46	8.34	18.40	5.06
NCH3	-71.32	-20.97	53.16	0.43	0.44	3.49	9.39	17.74	5.04
NCH4	-71.38	-22.99	50.54	0.17	0.39	3.31	9.99	17.07	5.19
NCH5	-71.56	-24.95	47.56	0.26	0.47	3.00	7.47	18.21	4.89
NCH6	-71.85	-26.98	46.21	0.37	0.46	2.79	5.46	19.73	4.96
JFR1	-72.33	-28.99	44.45	0.18	0.29	2.63	5.05	19.85	5.00
JFR2	-72.58	-30.51	41.48	0.21	0.32	2.47	6.22	18.24	4.93
JFR3	-72.74	-31.93	39.09	0.28	0.39	2.34	7.41	16.81	4.75

Model Name	Midpoint along Trench		Seafloor Age	Misfit Measure		Bending Moment M	Deflection Curvature κ	Elastic Thickness T_e	Depth Offset w_0
	Lon	Lat	(Ma)	w	Δg	joint (ψ)	(10^{16} Nm)	(10^{-7}/m)	(km)
CAL2	178.98	50.34	52.33	0.36	0.31	3.32	6.89	19.35	5.18
CAL3	-179.03	50.27	53.57	0.32	0.32	3.41	6.91	19.50	5.07
CAL4	-176.89	50.33	55.57	0.24	0.36	3.52	6.42	20.19	5.17
CAL5	-174.91	50.51	56.69	0.24	0.40	3.57	6.04	20.71	5.31
CAL6	-172.97	50.73	58.68	0.37	0.35	3.55	4.58	22.67	5.44
EAL1	-170.88	51.04	60.22	0.33	0.32	3.52	3.67	24.31	5.48
EAL2	-168.91	51.47	58.63	0.39	0.35	3.32	3.16	25.08	5.44
EAL3	-166.97	51.96	56.89	0.33	0.32	3.36	3.96	23.36	5.26
EAL4	-164.94	52.47	56.16	0.29	0.32	3.28	3.73	23.64	5.26
EAL5	-162.90	52.97	55.93	0.31	0.23	3.27	3.72	23.63	5.31
PHL4	126.84	10.02	96.27	0.35	0.32	5.31	6.00	23.68	5.56
PHL5	127.31	8.00	102.12	0.37	0.35	5.70	8.76	21.38	5.75
KER1	-178.41	-34.95	110.61	0.39	0.29	5.00	3.21	28.61	5.90
KER2	-177.63	-33.11	105.78	0.22	0.30	5.11	3.81	27.23	6.09
KER3	-176.77	-31.04	100.44	0.37	0.29	5.15	4.43	25.95	5.85
KER4	-176.01	-29.08	94.23	0.40	0.40	5.09	4.86	25.05	5.79
KER5	-175.47	-26.98	88.40	0.43	0.51	4.65	3.56	27.08	5.56

Model Name	Midpoint along Trench		Seafloor Age	Misfit Measure		Bending Moment M	Deflection Curvature κ	Elastic Thickness T_e	Depth Offset w_0
	Lon	Lat	(Ma)	w	Δg	joint (ψ)	(10^{16} Nm)	(10^{-7}/m)	(km)
TON1	-175.10	-25.04	87.50	0.47	0.48	4.59	3.60	27.20	5.71
TON2	-174.47	-23.04	91.49	0.28	0.35	4.95	4.46	25.54	5.90
TON3	-173.46	-21.02	97.79	0.26	0.29	4.97	3.85	26.88	6.06
TON4	-172.73	-19.08	101.46	0.43	0.38	4.94	3.50	27.72	5.73
TON5	-172.25	-16.97	105.22	0.30	0.31	5.48	5.79	24.22	5.90
TON6	-172.45	-15.58	108.14	0.51	0.46	5.59	6.28	23.73	5.36
NKU3	155.23	47.01	113.20	0.33	0.27	5.68	6.32	23.82	5.77
SKU1	152.99	45.31	115.60	0.31	0.28	5.62	5.65	24.64	5.74
SKU2	151.07	44.30	116.44	0.21	0.21	5.76	6.63	23.55	5.68
SKU4	147.08	42.12	126.24	0.35	0.31	5.27	3.51	28.26	5.89
SKU5	145.64	41.36	129.36	0.22	0.25	5.26	3.41	28.53	5.89
JAP1	144.71	40.42	130.27	0.21	0.20	5.18	3.16	29.10	5.91
JAP2	144.26	39.01	131.47	0.34	0.30	5.22	3.24	28.92	5.93
JAP3	143.50	36.96	133.09	0.33	0.31	5.07	2.84	29.94	5.92
JAP4	142.29	34.91	132.36	0.54	0.41	5.41	3.83	27.70	5.83
IZU1	142.13	33.00	135.00	0.31	0.28	5.99	6.97	23.46	5.80
IZU2	142.39	31.01	138.03	0.32	0.28	5.84	5.72	24.85	5.89
IZU3	143.00	29.05	141.06	0.31	0.29	5.83	5.54	25.11	5.89

Model Name	Midpoint along Trench		Seafloor Age	Misfit Measure		Bending Moment M	Deflection Curvature κ	Elastic Thickness T_e	Depth Offset w_0
	Lon	Lat	(Ma)	w	Δg	joint (ψ)	(10^{16} Nm)	(10^{-7}/m)	(km)
NMA1	145.14	23.05	140.64	0.51	0.42	5.11	2.87	30.00	5.40
NMA4	147.88	16.99	148.82	0.34	0.37	5.77	4.99	25.91	5.24
SMA1	147.54	14.97	151.29	0.55	0.41	5.68	4.50	26.66	5.51
SMA3	144.57	11.90	150.33	0.31	0.41	6.24	8.64	22.13	5.07
SMA4	142.59	11.24	148.12	0.37	0.44	6.14	7.69	22.91	5.28

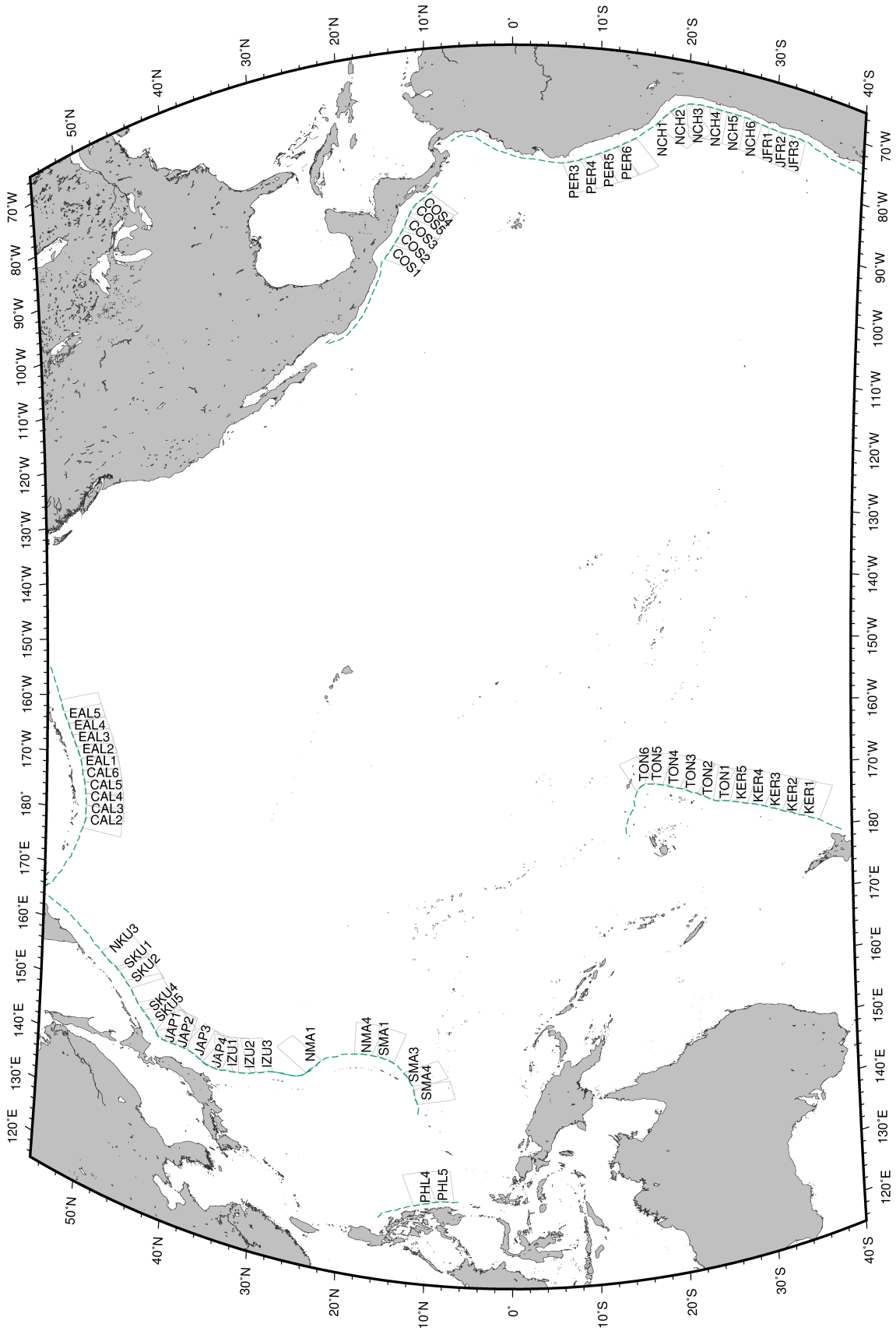
EAL5
EAL4
EAL3
EAL2
EAL1
CAL6
CAL5
CAL4
CAL3
CAL2
NKU3
SKU1
SKU2
SKU4
SKU5
JAP1
JAP2
JAP3
JAP4
IZU1
IZU2
IZU3
NMA1
NMA4
SMA1
SMA3
SMA4
PHL4
PHL5
COS4
COS5
COS3
COS2
COS1
PER3
PER4
PER5
PER6
NCH1
NCH2
NCH3
NCH4
NCH5
NCH6
JFR1
JFR2
JFR3
TON6
TON5
TON4
TON3
TON2
TON1
KER5
KER4
KER3
KER2
KER1

Figure 4.7 *(previous page)*: The dashed green lines indicate the planform of the trench axis (Bassett & Watts, 2015a,b), while the solid gray lines enclose the regions over which bathymetry and gravity observations were fit to the model flexural surface grids.

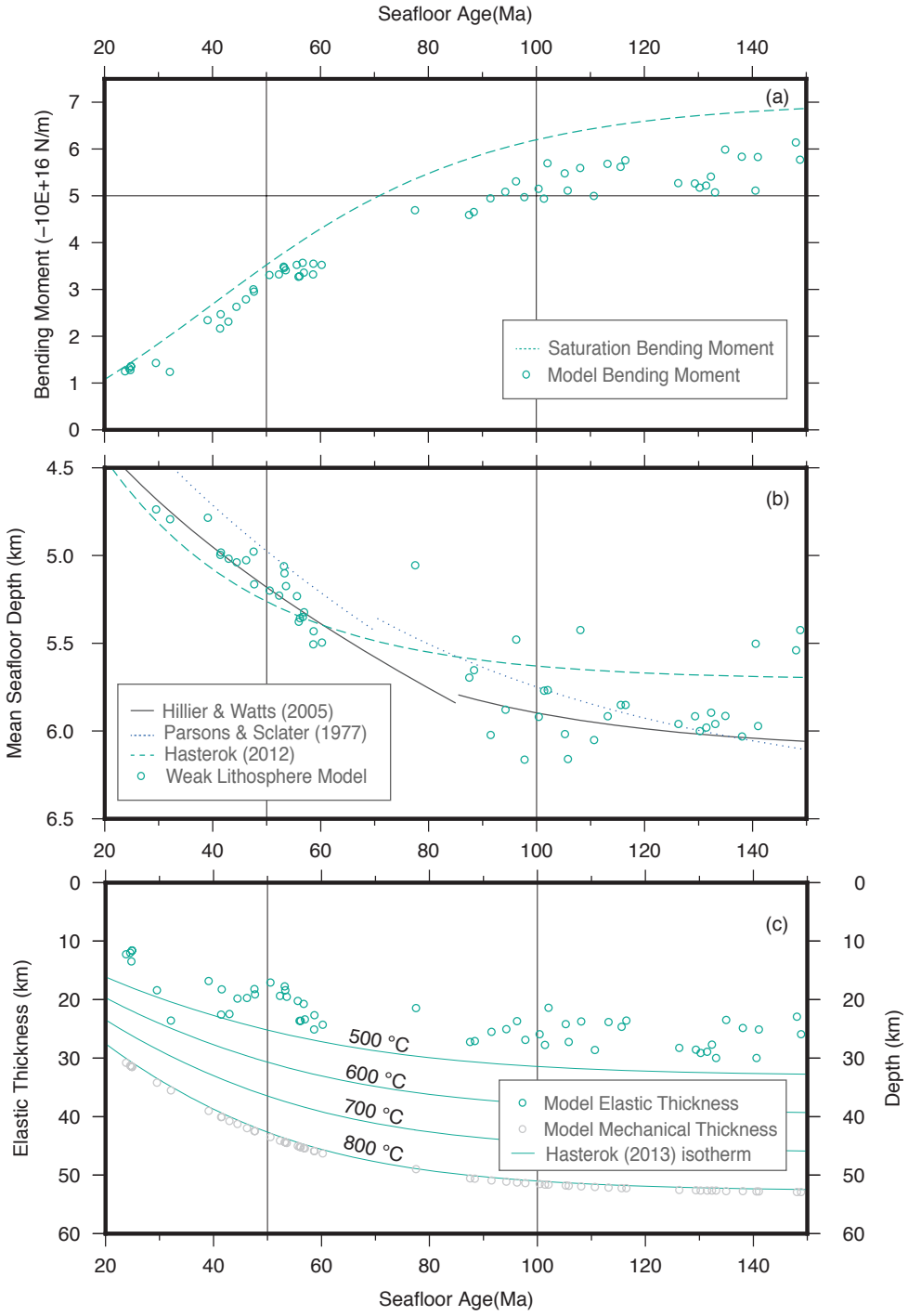
Seafloor Age(Ma)
20
40
60
80
100
120
140
(a)
Bending Moment (−10E+16 N/m)
0
1
2
3
4
5
6
7
Saturation Bending Moment
Model Bending Moment
(b)
Mean Seafloor Depth (km)
4.5
5.0
5.5
6.0
6.5
Hillier & Watts (2005)
Parsons & Sclater (1977)
Hasterok (2012)
Weak Lithosphere Model
(c)
Elastic Thickness (km)
Depth (km)
0
10
20
30
40
50
60
500 °C
600 °C
700 °C
800 °C
Model Elastic Thickness
Model Mechanical Thickness
Hasterok (2013) isotherm
Seafloor Age(Ma)

Figure 4.7 *(previous page)*: The model results (in diamond symbols) are plotted against seafloor age at the trench outer slope for the following quantities: a) bending moment, b) seafloor depth offset, and c) elastic thickness. There is a clear increase in the bending moment with age that is limited by the saturation moment given by the specified plate rheology.

4.4 Discussion

4.4.1 Lithospheric Strength Versus Age

The material comprising oceanic lithosphere has fairly uniform composition due to its formation at seafloor spreading ridges, and its thermal history is mainly governed by plate cooling as it moves away from these ridges towards subduction zones. Therefore, the mechanical behavior of oceanic lithosphere should depend mainly on its temperature (McKenzie et al., 2005). Compilations of surface heat flow measurements (Hasterok et al., 2011), and ocean depth related to thermal subsidence (Parsons & Sclater, 1977; Hillier & Watts, 2005) show a clear dependence on lithosphere age. These suggest that plate cooling models with age dependence can be used to infer mechanical strength via some choice of temperature-dependent rheology. However, global studies of effective elastic thickness values as estimated from flexure modeling at trenches (Levitt & Sandwell, 1995; Bry & White, 2007) do not seem to support the conclusion of the lithosphere thickening with age. Attempts at explaining this apparent conflict have emphasized the role of inelastic yielding in the weakening of the plate at the trench outer slope (Wessel, 1992; Bry & White, 2007; Craig & Copley, 2014). Evidence for stresses within the plate exceeding the elastic limit includes the prevalence of surface fractures in high-resolution bathymetry (Massell, 2002), dipping reflectors in seismic reflection profiles (Ranero et al., 2003; Boston et al., 2014), and the occurrence of earthquakes with normal fault mechanisms (Emry & Wiens, 2015; Craig et al., 2014).

In our modeling approach, we prescribe the initial elastic thickness by setting it to be equal to the mechanical thickness (solid line Figure 4.7c), which is

the depth at which the ductile yield stresses decrease to some arbitrary threshold. In our case this limit was set to be 10 MPa (Ranalli, 1995). Since the ductile yield stresses are related to temperature, the mechanical thickness should increase with age, and depending on the plate cooling model selected there is a correspondence with a certain temperature value. For the Hasterok (2013) model, these initial elastic thickness values track the 800° C isotherm closely. As mentioned in previous sections, by iteratively computing curvatures the flexure models we use can calculate an updated plate rigidity. The results from our models demonstrate that a plate with a mechanical thickness which is initially dependent on age can undergo sufficient reduction in effective elastic thickness to fit the high deflection curvature in the observed bathymetry and gravity.

Furthermore, the models show that all subduction zones considered for this study are approaching moment saturation. Moreover, the model estimated moment increases dramatically with age in parallel with the saturation moment. The most obvious signature of this is in the gravity data along the Chile subduction zone that has only around a -140 mGal trough over the young trench at a latitude of 30° S. This decreases going northward where older lithosphere is being subducted to a value of -250 mGal at a latitude of 20° S.

4.4.2 Outer Rise Fracturing

As discussed above, the plate is nearly moment saturated at the trench axis so the upper part of the plate, where strength is controlled by brittle fracturing, should have faults that extend from the surface to nearly 1/2 the plate thickness. With a few assumptions we can use the model to predict the vertical offset on the outer rise faults. The model is shown in Figure 4.8 where a plate of initial thickness H has a curvature of $\frac{\partial^2 w}{\partial x^2}$, where x is the direction of maximum curvature. The amount of strain is related to the curvature and the distance from the nodal plane by $\epsilon = -z\frac{\partial^2 w}{\partial x^2}$ (Turcotte & Schubert, 2014). The strain is purely elastic near the nodal plane, but there is inelastic yielding in both the upper and lower portions of the plate where there is sliding on optimally oriented faults and ductile flow, respectively. We assume that these regions are incompressible so that horizontal

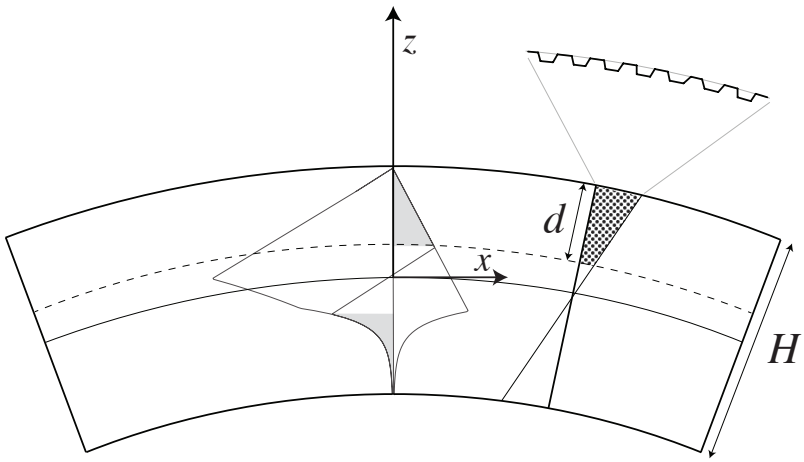

Figure 4.8: Schematic diagram showing a plate of thickness that is bent beyond its elastic limit. According to the YSE formulation fractures will extend to a depth d. We assume the upper zone of inelastic deformation is incompressible (stippled). The depth-averaged extension in that zone is accommodated by faulting and graben formation on the surface.

extension in the upper deformed layer of depth d is accommodated by vertical compaction. The compaction will appear on the surface as down-dropped blocks (Figure 4.8 inset). The average vertical compaction of the surface is equal to the horizontal strain integrated through the thickness of the upper deformed layer.

$$\Delta h = \frac{\partial^2 w}{\partial x^2} \int_{H/2-d}^{H/2} z dz \tag{4.14}$$

The result is

$$\Delta h = \frac{1}{2} \frac{\partial^2 w}{\partial x^2} d(H-d). \tag{4.15}$$

For a plate having an initial 50 km thickness and a faulting depth of 20 km and a typical curvature of $4{\times}10^{-7}/m$, the vertical compaction will be 120 m. If the ratio of uncompacted surface (horst) to down dropped blocks (graben) is 1/2, then the vertical relief will be 240 m. Note that in the numerical plate bending calculation,

the depth of the nodal plane is adjusted such that the integrated in-plane stress is zero so it will not be exactly in the position. Moreover, possible non-zero average in-plane stress will modify the depth and amplitude of the faulting. In the extreme case where the faults extend throughout the thickness of the plate, the compaction is

$$\Delta h = \frac{1}{4}\frac{\partial^2 w}{\partial x^2} H^2. \tag{4.16}$$

For a 50 km thick plate and curvature of 4×10^{-7}/m, the vertical compaction will be 250 m. If the ratio of horst to graben is 1/2, the vertical relief would be very large 500 m. Thus the relief of the horst and graben on the outer trench wall will depend on plate curvature, the initial plate thickness, and the strength of the in-plane force.

We can compare this model prediction with the amplitude of the horst and graben topography on the outer trench wall of the Japan and Chile trenches. We analyse the SRTM15_PLUS 15-minute digital bathymetry grid and apply the spectral averaging routines of Bassett & Watts (2015a,b) to remove the long-wavelength, trench-normal topography associated with the outer-rise and the seaward wall of the trench. Residual bathymetry along the Japan trench is shown in Figure 4.8b and the order of magnitude reduction in dynamic range of the topographic grid improves the identification of horsts and grabens. The residual bathymetric grid is sampled along 150 km long trench-normal profiles. We then interpret two surfaces along the top of horst blocks and the base of grabens respectively (gray dash in Figure 4.8a). The distance between these surfaces shows how the amplitude of the horst and graben topography varies with distance from the trench-axis. The proportion of grabens is estimated from the proportion of the residual bathymetric profile that is below the mid-point of the horst and graben surfaces.

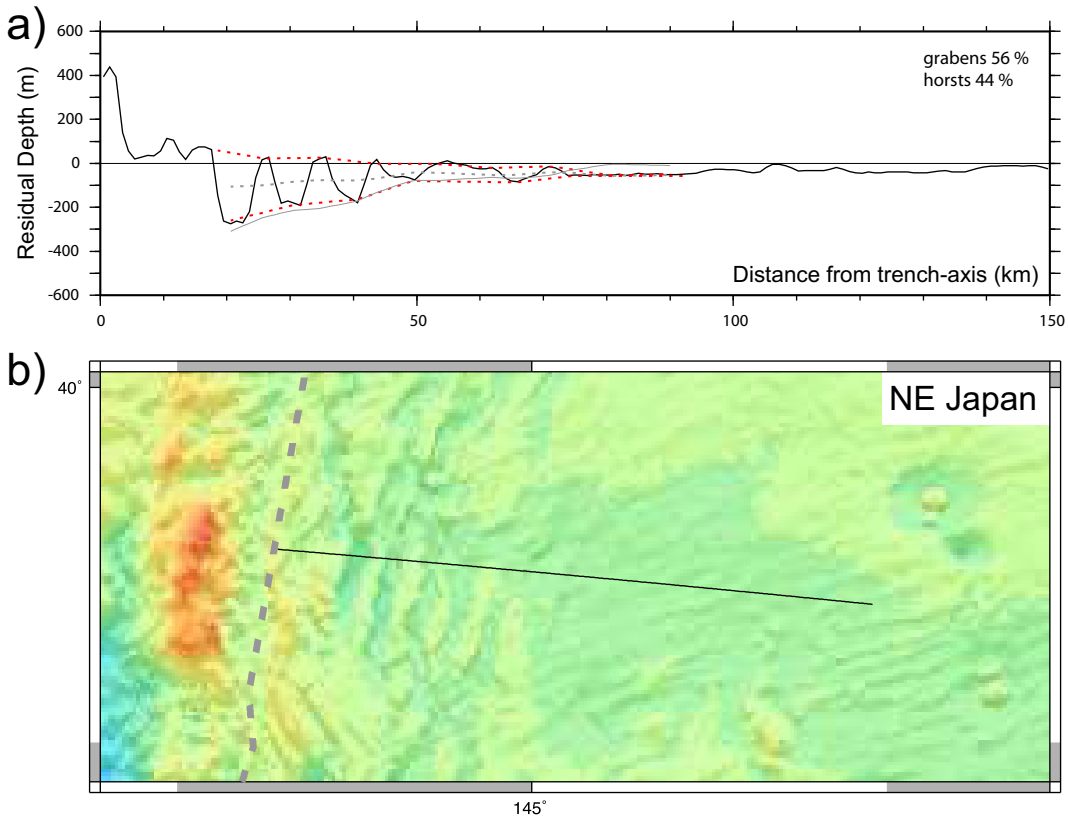

Figure 4.9: Outer-rise fractures in NE Japan a) Residual bathymetry across the seaward all of the trench and outer-rise. Dashed grey profiles traverse the top of horst blocks and the base of grabens. The distance between these surfaces (dotted red line) is used to estimate the depth of grabens. The dotted grey line is equidistant between the top (horst) and bottom (graben) surfaces and is used to estimate the proportion of horsts and grabens. b) Residual SRTM+ swath bathymetry. Dashed grey and solid black lines mark the trench-axis and the location of the profile shown in a) respectively.

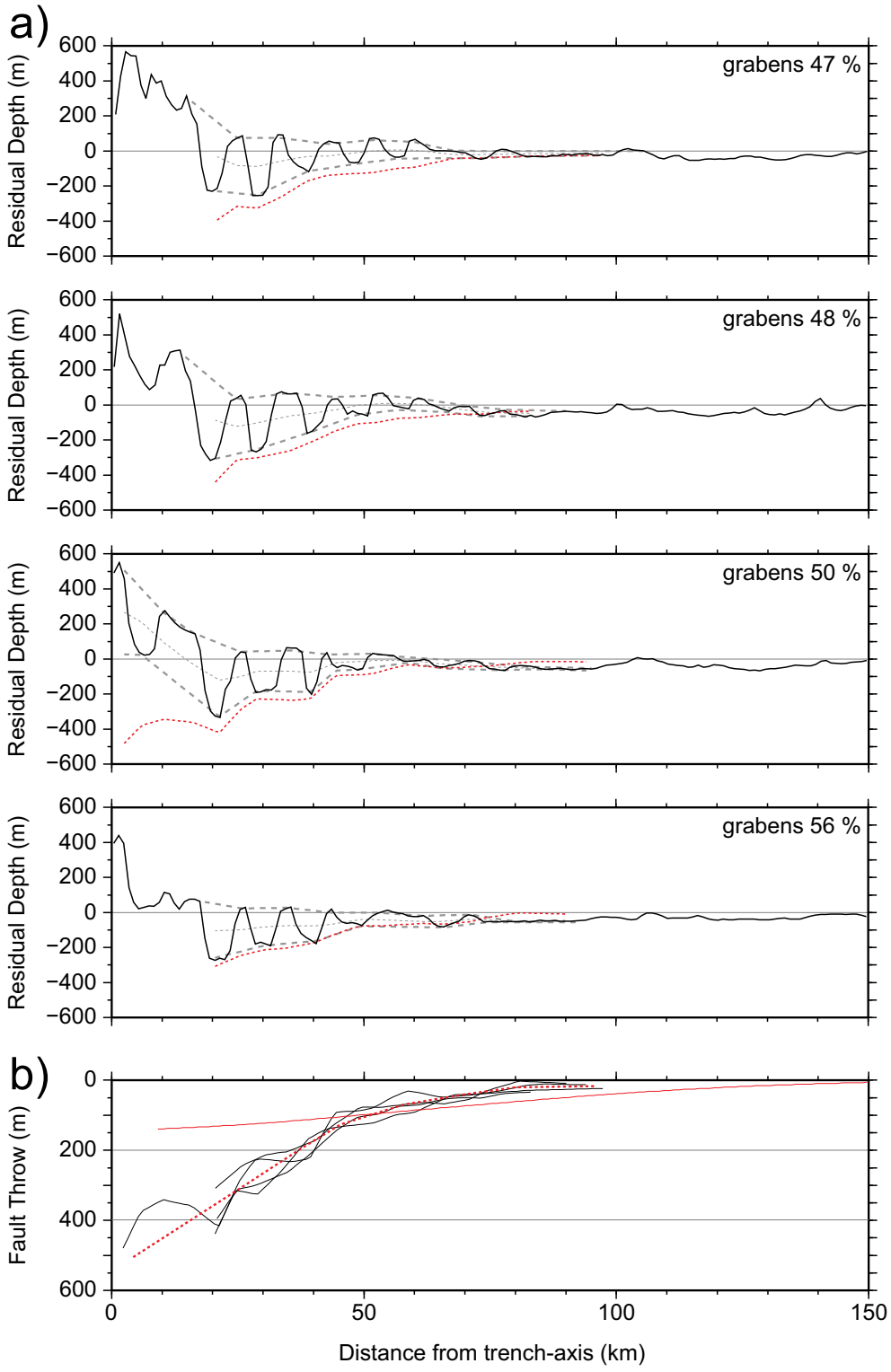
a)
Residual Depth (m)
600
400
200
0
−200
−400
−600
grabens 47 %
grabens 48 %
grabens 50 %
grabens 56 %
b)
Fault Throw (m)
0
200
400
600
0
50
100
150
Distance from trench-axis (km)

Figure 4.10 *(previous page)*: a) Profiles showing outer-rise fractures in NE Japan between 39.5° N and 40° N. Figure Nomenclature as in Figure 4.9a. b) Stack of graben depths along-strike showing how the throw on normal faults increases toward the trench-axis. Dashed red line shows the average of these profiles.

Figure 4.9a shows a sequence of residual bathymetric profiles taken over a 50 km wide region of the NE Japan trench centered on 39.5N. The dotted red profiles show the amplitude of horst and graben topography and the stack of these profiles is shown in Figure 8b. This stack shows that outer-rise faulting in this segment of the Japan trench begins at least 100 km from the trench-axis. The amplitude of horst and graben topography increases gradually to 100m, 45 km from the trench-axis. Landward of this point the fault throw increases significantly and 400-500 m deep are grabens observed within 20 km of the trench-axis. The solid red profile in Figure 4.9 shows the fault throw predicted from our model. This is close to the observed graben depth at distances >50 km from the trench, but is a factor >2 smaller than the deepest grabens near the trench-axis.

We have repeated this analysis for a segment of the South Chile subduction zone centered on 31S. As shown in Figure 4.9b, although the abyssal hill fabric in this region is pronounced, outer-rise faults are visible in the residual SRTM15_PLUS bathymetry (Figure 4.10). In contrast to NE Japan, horsts and grabens are only well expressed within 45 km of the trench-axis (Figure 10a). This may suggest that outer-rise fracturing does not extend further from the trench-axis, or that the smaller amplitude of faults in this region are being masked by pre-existing plate structure. In Figure 10b, fault throw profiles for Chile are plotted in black overlying those calculated in Japan (light grey). The proportion of grabens in both is approximately 50%.

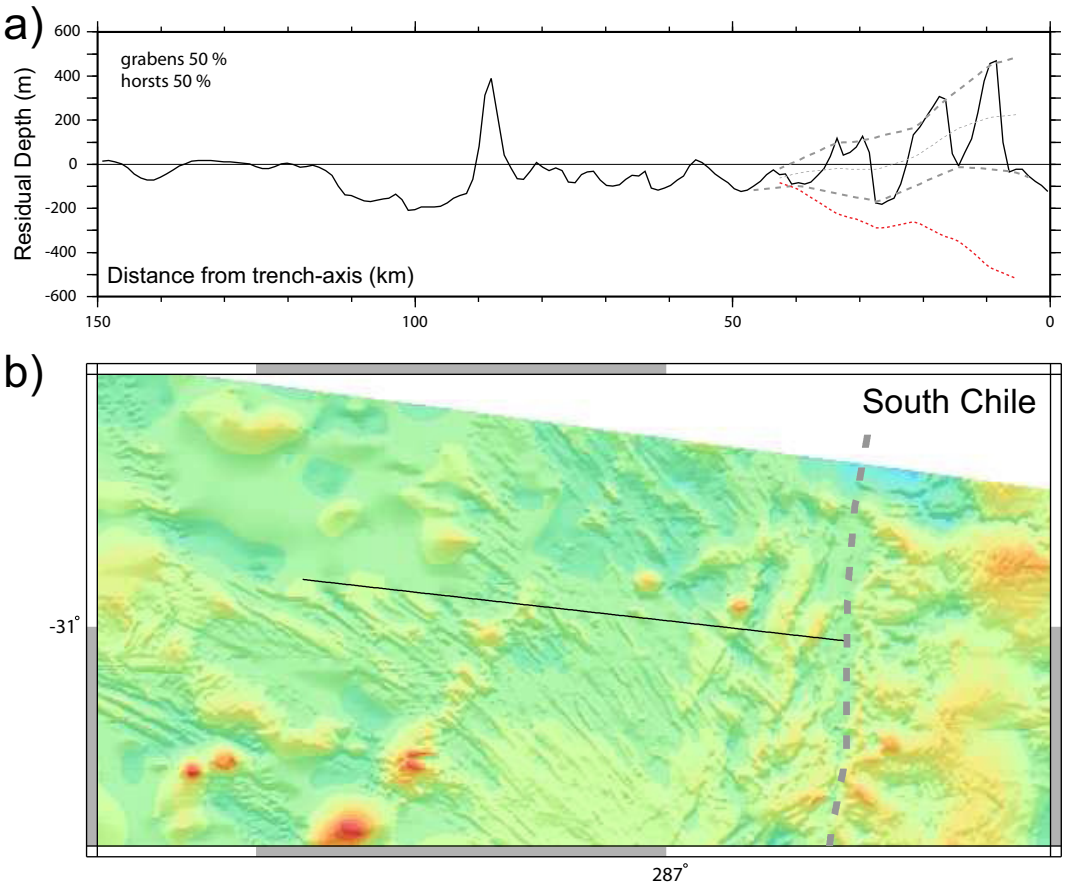

Figure 4.11: Outer-rise fractures in S Chile a) Residual bathymetry across the seaward all of the trench and outer-rise. Dashed grey profiles traverse the top of horst blocks and the base of grabens. The distance between these surfaces (dotted red line) is used to estimate the depth of grabens. The dotted grey line is equidistant between the top (horst) and bottom (graben) surfaces and is used to estimate the proportion of horsts and grabens. b) Residual SRTM+ swath bathymetry. Dashed grey and solid black lines mark the trench-axis and the location of the profile shown in a) respectively.

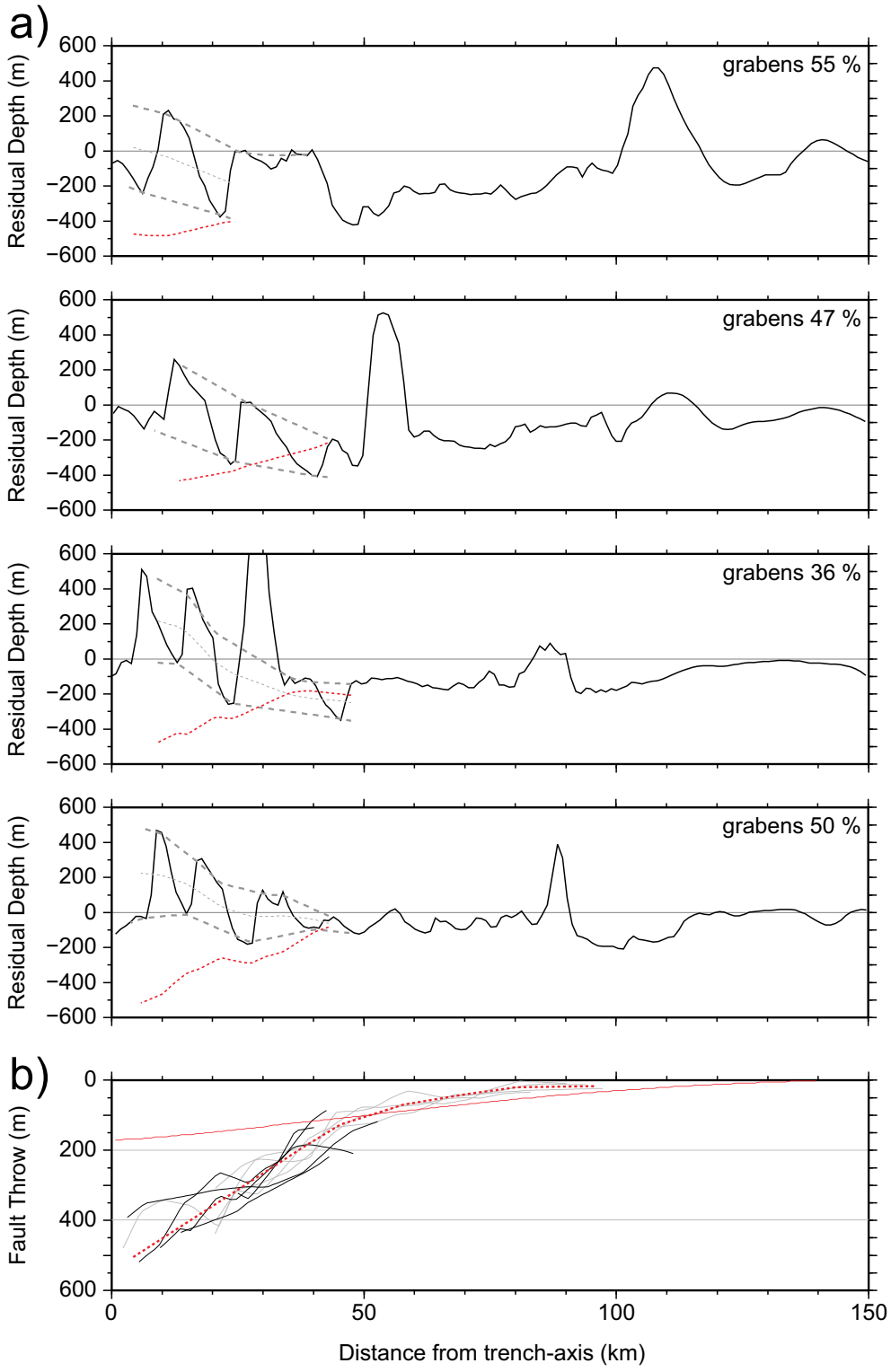
a)
Residual Depth (m)
600
400
200
0
−200
−400
−600
grabens 55 %
grabens 47 %
grabens 36 %
grabens 50 %
b)
Fault Throw (m)
0
200
400
600
0
50
100
150
Distance from trench-axis (km)

Figure 4.12 *(previous page)*: (a) Profiles showing outer-rise fractures in S Chile between 30° S and 31° S. Figure Nomenclature as in Figure 4.10a. b) Stack of graben depths along-strike showing how the throw on normal faults increases toward the trench-axis. Solid red line shows the graben depth predicted from the model. Black and light profiles are from S Chile and NE Japan respectively. Solid red line shows the graben depth predicted from the model.The dashed red line is also unchanged from Figure 8b. Despite significant differences in seafloor age, the throw on normal faults in S Chile is comparable to that observed in NE Japan.

The difference between our model for fault throw and the observed amplitude of the horst and graben topography close to the trench axis for the Japan and South America subduction zones potentially indicates that the observed normal faults could be accommodating more strain than inferred from our elastic-plastic formulation. An unknown mechanism that lowers the nodal plane might further increase the model fault throws.

We also note that despite the 90 Myr difference in the age of the subducting plate, the amplitude of horst and graben topography is comparable in both regions. The similarity in the amplitude of fault throws seems in contrast to the observed increase in seismogenic depth for earthquakes on the outer rise and slope (McKenzie et al., 2005; Craig et al., 2014), therefore implying that normal faults of shallower depth extent do not necessarily produce less prominent surface fractures. However, this is not necessarily in conflict with our model since a smaller value of the depth of yielding can be compensated for by a higher curvature to produce the same amount of predicted change in height Δh. Furthermore, within the brittle zone the yield stresses are largely independent of temperature, so a dependence on age would not be obvious.

In another study concerned with the interpretation and analysis of several seismic reflection lines across the outer slope of the Japan trench (Boston et al., 2014), the authors suggest that while steady slip on older faults can accumulate to produce large offsets, the presence of small offset scarps suggest that fracture can

continue forming on the plate surface as it approaches the trench. This may call the assumption of steady-state deformation on the trench outer slope into question.

4.4.3 Further Considerations

While the rheology parameters we selected to construct a suitable YSE for the flexure modeling produce satisfactory fits to seafloor depth and marine gravity, it may be possible to improve upon the results by conducting a systematic search of the parameters. We have used a combination of parameters in the YSE configuration that is unique to this work, but the individual values are still based on previously published numerical modeling or experimental work (Craig et al., 2014; Wessel, 1992; Zhong & Watts, 2013).

However, based on our preliminary tests, we concur with the conclusion of Zhong & Watts (2013) that altering parameters associated with the high-temperature ductile flow law (such as the activation energy or stress pre-factor) has a greater effect on the shape and curvature of the flexure surface than changing the coefficient of friction. Since the lower portion of the YSE determines the model mechanical thickness, this may imply that there is a range of initial elastic thickness values for undeformed lithosphere that eventually result in ideal fits after yielding occurs. A related concern in this regard is the choice of a thermal model, which would also increase or decrease the mechanical thickness. There are a few recent plate cooling models (McKenzie et al., 2005; Ritzwoller et al., 2004) which we did not examine in this work.

Also in Zhong & Watts (2013), the authors argue that a range of friction coefficient values from 0.25 to 0.7 while holding other parameters constant results in model misfits that are similar. From analysis of the strikes of new fractures and reactivated abyssal hills, Billen et al. (2007) propose that the friction coefficient is around 0.6, while from the study of focal mechanism dips, Craig et al. (2014) infers a value of about 0.3. In our modeling we use a single set of YSE parameters and so do not take into account whether incoming seafloor fabric is being reactivated (for example, at the Middle America trench (Ranero et al., 2003)), or new fractures are being formed (at the Tonga trench (Massell, 2002)). How-

ever, some regions appear more complicated because of a combination of these two styles of normal faulting, such as that observed offshore portions of the Japan and Izu-Bonin trenches (Kobayashi et al., 1998; Nakanishi, 2011). Apart from the coefficient of friction, we have not considered the effect of changing the cohesion parameter. Reducing the fault cohesion linearly as the elastic strain accumulates (Zhou et al., 2015; Naliboff et al., 2013) could induce progressive weakening with increased curvature that is more pronounced than our models are currently capable of, and might help improve our models of faulting.

A potential contribution of our fault modeling approach to geochemical and geodynamics studies of the Earth's interior is in predicting the hydration of subducting lithosphere at the trench outer slope Faccenda et al. (2009). Understanding the water input at subduction zones has implications for theories of the planetary hydrological cycle at geological time scales. Observations at the outer slope of the Middle America trench using seismic refraction (Van Avendonk et al., 2011) and marine electromagnetic imaging techniques (Naif et al., 2015) suggest the presence of water as pore fluid or hydrous minerals throughout the oceanic crust and perhaps the uppermost mantle. Output from numerical experiments illustrate that bending-related stresses allow seawater to penetrate downward along seafloor faults (Faccenda et al., 2009). Once within the lithosphere the water can be bound into mineral phases through chemical reactions such as serpentinization. If simple assumptions are made connecting the seismogenic depth to the extent of hydration, the amount of water input carried by the into the upper mantle could be estimated (Emry & Wiens, 2015). Once a method for validating our model predictions of faulting depth is tested, we can carry out a similar calculation and relate this to other constraints on the water content in the mantle.

4.5 Conclusions

We have extended previous efforts at modeling thin elastic plate flexure at subduction zones by incorporating inelastic effects and considering loads applied at the actual trench planform geometry. Our approach fitted depth soundings

and gravity jointly to variable rigidity flexural surface models at 59 sites around the Pacific basin. Traditional YSE models provide worse fits than our choice of modified parameters because they fail to capture the steep sudden descent of the plate at the trench outer slope simultaneously with the broad prominence of the outer rise. The preferred YSE has a lower mechanical thickness and weak friction, which results in the high curvatures at the trench outer slope that seem to be required by the observations. Most important, the estimated moment increases by a factor of 6 between the youngest and oldest lithosphere in excellent agreement with the strengthening versus age from the thermal models. All the plates are bent well beyond their elastic limit at the trench axis as required by subduction. As in previous studies the effective elastic thickness has no clear relationship with seafloor age, and lithosphere older than 40 Ma all approach a thickness of $\sim$ 25 km.

We used results from our model grids to calculate the vertical throw on the outer trench wall normal faults. A comparison with the actual vertical throw shows poor fits with the actual throw being $\sim$ 3 times greater than the model prediction. This misfit, as well as the inability of some of the models to achieve the observed outer trench wall curvature, suggests that the lithosphere undergoes a weakening well beyond the prediction of the YSE models. Perhaps future models incorporating a curvature-dependent strain-weakening mechanism could provide a better match to the outer trench wall fracturing. We intend to explore these types of models before submitting this work for publication. Once our models are able to generate more realistic depictions of faulting we plan on connecting our results to tweak global estimates of water input from subducting slabs.

4.6 Acknowledgements

Chapter 4, in full, is a preprint of material being prepared for submission to Geophysics Geochemistry Geosystems: Garcia, E. S., D. T. Sandwell, and D.G. Bassett, "Outer Trench Slope Flexure and Faulting at Pacific Basin Subduction Zones". The dissertation author was the primary investigator.

References

Bassett, D. & Watts, A. B., 2015a. Gravity anomalies, crustal structure, and seismicity at subduction zones: 1. seafloor roughness and subducting relief, *Geochemistry, Geophysics, Geosystems*, **16**(5), 1508–1540.

Bassett, D. & Watts, A. B., 2015b. Gravity anomalies, crustal structure, and seismicity at subduction zones: 2. interrelationships between fore-arc structure and seismogenic behavior, *Geochemistry, Geophysics, Geosystems*, **16**(5), 1541–1576.

Billen, M., Cowgill, E., & Buer, E., 2007. Determination of fault friction from reactivation of abyssal-hill faults in subduction zones, *Geology*, **35**(9), 819–822.

Boston, B., Moore, G. F., Nakamura, Y., & Kodaira, S., 2014. Outer-rise normal fault development and influence on near-trench dcollement propagation along the Japan Trench, off Tohoku, *Earth, Planets and Space*, **66**(1), 135.

Bry, M. & White, N., 2007. Reappraising elastic thickness variation at oceanic trenches, *Journal of Geophysical Research*, **112**(B8).

Burov, E. B. & Diament, M., 1995. The effective elastic thickness (t e) of continental lithosphere: What does it really mean?, *Journal of Geophysical Research: Solid Earth*, **100**(B3), 3905–3927.

Byerlee, J., 1978. Friction of rocks, *Pure and applied geophysics*, **116**(4-5), 615–626.

Caldwell, J. G., Haxby, W. F., Karig, D. E., & Turcotte, D. L., 1976. On the applicability of a universal elastic trench profile, *Earth and Planetary Science Letters*, **31**(2), 239–246.

Craig, T., Copley, A., & Jackson, J., 2014. A reassessment of outer-rise seismicity and its implications for the mechanics of oceanic lithosphere, *Geophysical Journal International*, **197**(1), 63–89.

Craig, T. J. & Copley, A., 2014. An explanation for the age independence of oceanic elastic thickness estimates from flexural profiles at subduction zones, and implications for continental rheology, *Earth and Planetary Science Letters*, **392**, 207–216.

Crosby, A. & McKenzie, D., 2009. An analysis of young ocean depth, gravity and global residual topography, *Geophysical Journal International*, **178**(3), 1198–1219.

Divins, D., 2003. Total sediment thickness of the world's oceans & marginal seas, noaa national geophysical data center, boulder, co.

Emry, E. L. & Wiens, D. A., 2015. Incoming plate faulting in the northern and western pacific and implications for subduction zone water budgets, *Earth and Planetary Science Letters*, **414**, 176–186.

Emry, E. L., Wiens, D. A., & Garcia-Castellanos, D., 2014. Faulting within the pacific plate at the mariana trench: Implications for plate interface coupling and subduction of hydrous minerals: Faulting at the mariana trench, *Journal of Geophysical Research: Solid Earth*, pp. n/a–n/a.

Faccenda, M., Gerya, T. V., & Burlini, L., 2009. Deep slab hydration induced by bending-related variations in tectonic pressure, *Nature Geoscience*, **2**(11), 790–793.

Garcia, E. S., Sandwell, D. T., & Luttrell, K. M., 2015. An iterative spectral solution method for thin elastic plate flexure with variable rigidity, *Geophysical Journal International*, **200**(2), 1010–1026.

Goetze, C. & Evans, B., 1979. Stress and temperature in the bending lithosphere as constrained by experimental rock mechanics, *Geophysical Journal International*, **59**(3), 463–478.

Hasterok, D., 2013. A heat flow based cooling model for tectonic plates, *Earth and Planetary Science Letters*, **361**, 34–43.

Hasterok, D., Chapman, D. S., & Davis, E., 2011. Oceanic heat flow: Implications for global heat loss, *Earth and Planetary Science Letters*, **311**(3), 386–395.

Hillier, J. K. & Watts, A., 2005. Relationship between depth and age in the north pacific ocean, *Journal of Geophysical Research: Solid Earth*, **110**(B2).

Hirth, G. & Kohlstedt, D., 2003. Rheology of the upper mantle and the mantle wedge: A view from the experimentalists, *Inside the subduction Factory*, pp. 83–105.

Kim, S.-S. & Wessel, P., 2008. Directional median filtering for regional-residual separation of bathymetry, *Geochemistry, Geophysics, Geosystems*, **9**(3).

Kobayashi, K., Nakanishi, M., Tamaki, K., & Ogawa, Y., 1998. Outer slope faulting associated with the western kuril and japan trenches, *Geophysical Journal International*, **134**(2), 356–372.

Levitt, D. A. & Sandwell, D. T., 1995. Lithospheric bending at subduction zones based on depth soundings and satellite gravity, *Journal of Geophysical Research*, **100**(B1), 379.

Manriquez, P., Contreras-Reyes, E., & Osses, A., 2014. Lithospheric 3-d flexure modelling of the oceanic plate seaward of the trench using variable elastic thickness, *Geophysical Journal International*, **196**(2), 681–693.

Massell, C. G., 2002. *Large-scale structural variation of trench outer slopes and rises*, Ph.D. thesis, University of California, San Diego.

McKenzie, D., Jackson, J., & Priestley, K., 2005. Thermal structure of oceanic and continental lithosphere, *Earth and Planetary Science Letters*, **233**(3), 337–349.

McNutt, M. K. & Menard, H. W., 1982. Constraints on yield strength in the oceanic lithosphere derived from observations of flexure, *Geophysical Journal International*, **71**(2), 363–394.

Mueller, S. & Phillips, R. J., 1995. On the reliability of lithospheric constraints derived from models of outer-rise flexure, *Geophysical Journal International*, **123**(3), 887–902.

Müller, R. D., Sdrolias, M., Gaina, C., & Roest, W. R., 2008. Age, spreading rates, and spreading asymmetry of the world's ocean crust, *Geochemistry, Geophysics, Geosystems*, **9**(4).

Naif, S., Key, K., Constable, S., & Evans, R. L., 2015. Water-rich bending faults at the middle america trench, *Geochemistry, Geophysics, Geosystems*, **16**(8), 2582–2597.

Nakanishi, M., 2011. Bending-related topographic structures of the subducting plate in the northwestern pacific ocean, in *Accretionary Prisms and Convergent Margin Tectonics in the Northwest Pacific Basin*, pp. 1–38, Springer.

Naliboff, J. B., Billen, M. I., Gerya, T., & Saunders, J., 2013. Dynamics of outer-rise faulting in oceanic-continental subduction systems, *Geochemistry, Geophysics, Geosystems*, **14**(7), 2310–2327.

Olson, C., Becker, J., & Sandwell, D., 2014. A new global bathymetry map at 15 arcsecond resolution for resolving seafloor fabric: Srtm15_plus, in *AGU Fall Meeting Abstracts*, vol. 1, p. 03.

Parsons, B. & Sclater, J. G., 1977. An analysis of the variation of ocean floor bathymetry and heat flow with age, *Journal of Geophysical Research*, **82**(5), 803–827.

Ranalli, G., 1995. *Rheology of the Earth*, Springer Science & Business Media.

Ranero, C. R., Phipps Morgan, J., McIntosh, K., & Reichert, C., 2003. Bending-related faulting and mantle serpentinization at the middle america trench, *Nature*, **425**(6956), 367–373.

Ritzwoller, M. H., Shapiro, N. M., & Zhong, S.-J., 2004. Cooling history of the pacific lithosphere, *Earth and Planetary Science Letters*, **226**(1), 69–84.

Sandwell, D. T., Müller, R. D., Smith, W. H., Garcia, E., & Francis, R., 2014. New global marine gravity model from cryosat-2 and jason-1 reveals buried tectonic structure, *Science*, **346**(6205), 65–67.

Turcotte, D. L. & Schubert, G., 2014. *Geodynamics*, Cambridge University Press, Cambridge, United Kingdom, 3rd edn.

Van Avendonk, H. J., Holbrook, W. S., Lizarralde, D., & Denyer, P., 2011. Structure and serpentinization of the subducting Cocos plate offshore Nicaragua and Costa Rica, *Geochemistry, Geophysics, Geosystems*, **12**(6).

Watts, A. B., 2001. *Isostasy and flexure of the lithosphere*, Cambridge University Press, Cambridge ; New York.

Wessel, P., 1992. Thermal stresses and the bimodal distribution of elastic thickness estimates of the oceanic lithosphere, *Journal of Geophysical Research: Solid Earth*, **97**(B10), 14177–14193.

Whittaker, J. M., Goncharov, A., Williams, S. E., Müller, R. D., & Leitchenkov, G., 2013. Global sediment thickness data set updated for the australian-antarctic southern ocean, *Geochemistry, Geophysics, Geosystems*, **14**(8), 3297–3305.

Wu, B., Conrad, C. P., Heuret, A., Lithgow-Bertelloni, C., & Lallemand, S., 2008. Reconciling strong slab pull and weak plate bending: The plate motion constraint on the strength of mantle slabs, *Earth and Planetary Science Letters*, **272**(1), 412–421.

Zhang, F., Lin, J., & Zhan, W., 2014. Variations in oceanic plate bending along the Mariana trench, *Earth and Planetary Science Letters*, **401**, 206–214.

Zhong, S. & Watts, A., 2013. Lithospheric deformation induced by loading of the hawaiian islands and its implications for mantle rheology, *Journal of Geophysical Research: Solid Earth*, **118**(11), 6025–6048.

Zhou, Z., Lin, J., Behn, M. D., & Olive, J.-A., 2015. Mechanism for normal faulting in the subducting plate at the mariana trench, *Geophysical Research Letters*, **42**(11), 4309–4317.